Polarization-Dependent Wavelength-Selective Structures for Multispectral Polarimetric Infrared Imaging

by

David R. Dunmeyer

Submitted to the

Department of Electrical Engineering and Computer Science

in partial fulfillment of the requirements for the degree of

Doctor of Philosophy

at the

MASSACHUSETTS INSTITUTE OF TECHNOLOGY

[February 2007]
January 2007

Author .....
Department of Electrical Engineering and Computer Science
Jan 17, 2007

Certified by .....
Cardinal Warde
Professor
Thesis Supervisor

Accepted by .....
Arthur C. Smith
Chairman, Department Committee on Graduate Students

Polarization-Dependent Wavelength-Selective Structures for Multispectral Polarimetric Infrared Imaging

by

David R. Dunmeyer

Submitted to the Department of Electrical Engineering and Computer Science
on Jan 17, 2007, in partial fulfillment of the
requirements for the degree of
Doctor of Philosophy

Abstract

The need for compact, rugged, low-cost multispectral-polarimetric filtering technology exists in both the civilian and defense communities. Such technology can be used for object detection, object recognition, and image contrast enhancement.

Mosaicked multispectral-polarimetric filter technology, using CMOS-type metallo-dielectric grating structures, is presented as a potential solution in which the spectral filtering and polarization filtering functions are performed in a single component.

In this work, single-layer and double-layer metallic-grating structures, embedded in uniform dielectric are investigated. Spectral tunability using only transverse grating properties in a two-layer metallic-grating structure is demonstrated. Additionally, one-layer and two-layer slotted-grid rectangular-aperture two-dimensional metallic gratings for infrared imaging are also studied.

To complement the simulations, thirty-nine separate infrared optical polarization and spectral filters were fabricated in silicon using the AMI 0.5μm / MOSIS foundry service, and they were characterized using polarized FTIR analysis. Polarized transmission spectra from these CMOS-based filters compare favorably with simulation results for four of the most promising filter types. An external-cavity-coupled single-layer metallic-grating structure, compatible with CMOS microbolometer detector technology is also offered as an application example.

Thesis Supervisor: Cardinal Warde
Title: Professor

Contents

List of Figures

Chapter 1

Introduction

1.1 Research Goals

The primary goals of this thesis are to develop new, highly-compact, multispectral, polarimetric filters using novel wavelength-selective and polarization-selective metallo-dielectric structures.

This thesis stems from a project in which we began investigating novel 3D architectures for designing multispectral polarization filters for mid-wave infrared (MWIR), λ =3-5μm, and long-wave infrared (LWIR), λ =7-14μm, imaging applications. To do this, we began looking at filtering structures that have been built and tested for use in microwave radar applications as well as structures used in contemporary visible optics. Our goal was to overcome limitations associated with multi-layered dielectric filters–limitations such as our inability to create stable, small-scale dielectric stacks for filtering of long-wavelength IR light.

We also studied stacked dielectric structures with the addition of imbedded wire-grid polarizers; by incorporating polarization filtering as part of the dielectric spectral filtering structure we can raise the overall transmission efficiency of in-band radiation as well as increase the TM vs. TE extinction ratio beyond that of spatially-separated polarization and spectral filters. Additionally, to overcome potential problems of optical cross-talk between polarization and spectral filters we incorporate side-lobe suppression techniques similar to those used in microwave radar structures.

This chapter begins by focusing upon the applications and motivations that drive this research. Specific wavebands of interest for object discrimination will be described in addition to specific polarizations and polarization extinction ratios required for useful sensor operation. Additionally, the current state of research in the infrared multispectral-polarimetric imaging field will be discussed.

1.1.1 Background

A sensor is a device used to sense or measure physical phenomena. Sensors detect electrical, mechanical, optical, chemical, tactile, and acoustic signatures and they extract and provide basic information about objects. Objects that may be difficult to discriminate using a single sensor are often differentiable with a multiple-sensor system that exploits several signature generation phenomena to gather data about a particular scene of interest. The application of multiple sensors, and the fusion of their data, offers numerous potential performance benefits over traditional single sensor approaches. Employing multiple sensors, which respond to different signatures, increases the probability that an object's signature will be found against a given set of other competing signatures such as weather, clutter, or background noise. Multiple sensor systems, in other words, diminish ambiguity and uncertainty in the measured information by reducing the set of hypotheses about the object or event. Multiple sensors may also be used to reduce the vulnerability to false conclusions drawn from single-sensor data. For instance, missiles seekers may carry multiple sensors and rely upon input from ground or air-based sensors to better guarantee a hit.

The research carried out for this paper focuses on the demonstrated need of an integrated sensor, with no moving parts, that can record the multispectral and polarization signatures of infrared scenes. This is done so that one can subsequently achieve improved image contrast and image fusion from the measured information.

For man-made objects embedded in natural scenes, multispectral signatures of the object could depend on the surface coating of the object and/or chemical composition of man-made materials. Moreover, multispectral data is significantly less sensitive to viewing geometry and surface smoothness than polarization data. On

the other hand, polarimetric measurement takes advantage of the fact that natural backgrounds show generally little or weak polarization signatures, while man-made objects tend to radiate with slightly more polarized radiation. A study for the 3-5μm waveband demonstrates that the polarized signatures of many natural objects were measured to have less than a 0.2% difference between TE and TM radiated components. However, man-made ground objects exhibited a 2-4% degree-of-linear-polarization (DoLP) [1, 2]. In addition, polarization data often contains information about the surface orientation and/or surface properties of objects, and a polarization signal can exist even when no intensity contrast is present [3, 4]. Consequently, it is believed that polarization and multispectral imaging data are complementary. By combining the two, better contrast can thus be achieved, since they depend on different optical characteristics of an object. However, as will be discussed further in this chapter, it is not yet clear which combinations of polarization and spectral measurements are optimal for object discrimination in any given scenario, as so little publicly-accessible data has been taken in natural and man-made scenes.

Our proposed filter designs integrate optical components that can determine spectral content, polarization state, and light intensity level in each pixel. One can use the integrated sensor in an infrared camera as shown in Figure 1-1 and then post-process the multiple outputs of each pixel with various image-fusion techniques to perform object discrimination. With a combination of the multispectral polarimetric mosaicked filter array (MPMFA) technology and various image fusion techniques, one should be able to perform selective discrimination among objects with nearly identical spatial and spectral features.

Additionally, in this chapter is discussed how we can utilize compactness, portability, ruggedness and signal processing strengths achieved through the use of semiconductor integrated circuit technology. Note that some desired features of the integrated sensor in Figure 1-1 are given in References [5] and [6] as well as in more detail in this chapter.

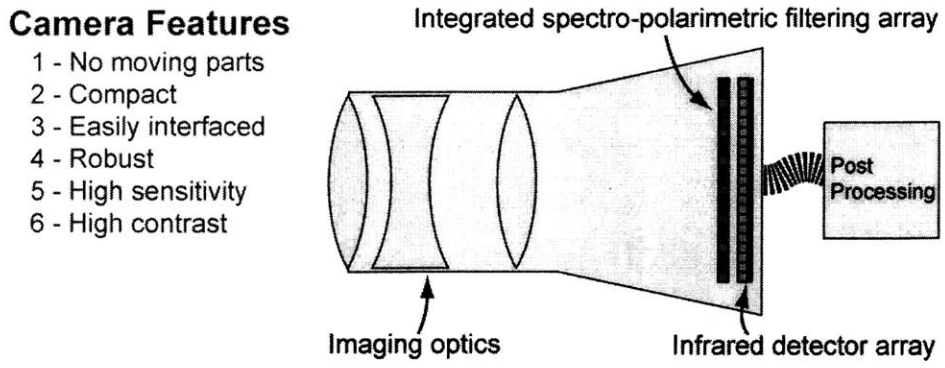

Figure 1-1: Integrated multispectral polarimetric sensor in an infrared camera and its desired features

1.2 Multispectral Polarimetric Mosaicked Filter Arrays

The original design for a multispectral polarimetric mosaicked filter array (MPMFA) proposed by Kim [5] uses a 3x3 array of pixels to act as a single macro-pixel, each of the pixels in that 3x3 array contains correlated but not identical information, as shown in Figure 1-2. Looking at all micro-pixels independently, one may obtain high-resolution information required for image fusion. Low resolution information is obtained from correlated image data from each macro-pixel. In total, this gives us effectively 10 images that need to be fused - one image for each of the 9 pixels in each macro-pixel and 1 image from the image formed by common spectral and polarimetric components of all the pixels. For example, if we had an 8x8 macro-pixel array, we would have 9 8x8 images each with separate polarization and spectral combinations. Additionally, by normalizing the energy contained in all the pixels, we can obtain a tenth image that is 64x64 pixels. Additional interpolation can be performed, utilizing the image offset between pixels within each macro-pixels, to increase this effective resolution even further. A diagram of the square-pixel MPMFA is shown in Figure 1-2.

Using modern methods in image interpolation and array fabrication, we can further reduce the signal-to-noise ratio when interpolating between pixels of similar color or polarization state. To do this, we can use a hexagonal grid pattern array that would sit atop a hexagonal grid detector array. The benefit of a hexagonal array filter is

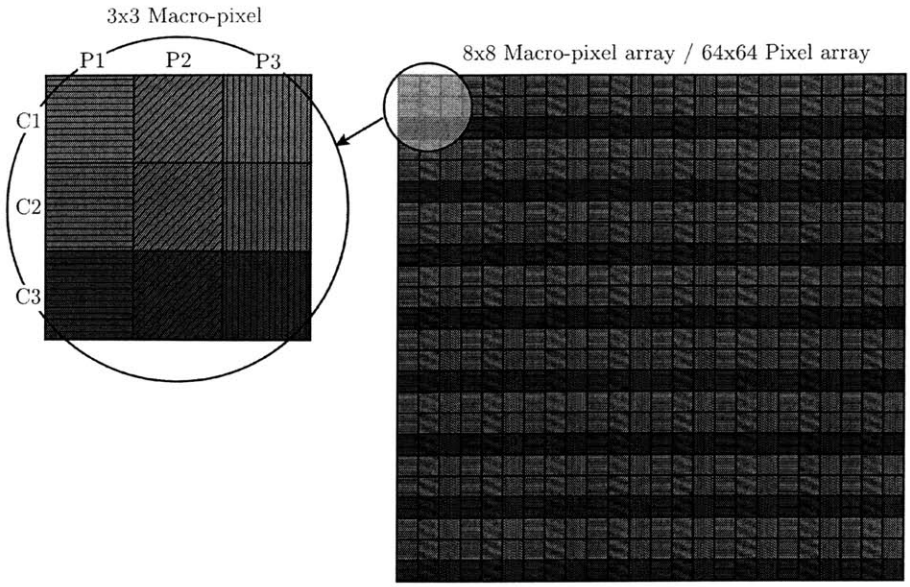

Figure 1-2: Left: A single three-color, three-polarization-state macro-pixel is shown. Each macro-pixel consists of 9 individual pixels, each of separate spatial location. **Right:** A 64x64 total micro-pixel array consists of an 8x8 array of macro-pixels.

that the centroid of each micro-pixel is equidistant to the center of each abutted micro-pixel. Therefore, one obtains data of equal spatial resolution in three directions instead of just two. Hexagonal structures have the drawback of requiring the use of hexagonal-grid IR detectors, which as of yet have not been manufactured in large scale. Additionally, more work must be done to minimize inter-pixel distances for tessellations involving more than three colors or three polarization states. In Figure 1-3(b) is an example of a hexagonal color filter array, similar to those used in some modern digital cameras. This tessellation consists of three colors, where each color has nearest neighbors of an equal number (in this case, three) of two distinct colors. In Figure 1-3(a), one sees a possible topology for just a hexagonal polarizing array. Notice there there is not even spacing between 45° (labeled as "3") and 135° (labeled as "4") polarizers. This is a necessary condition of a four-filter hexagonal grid.

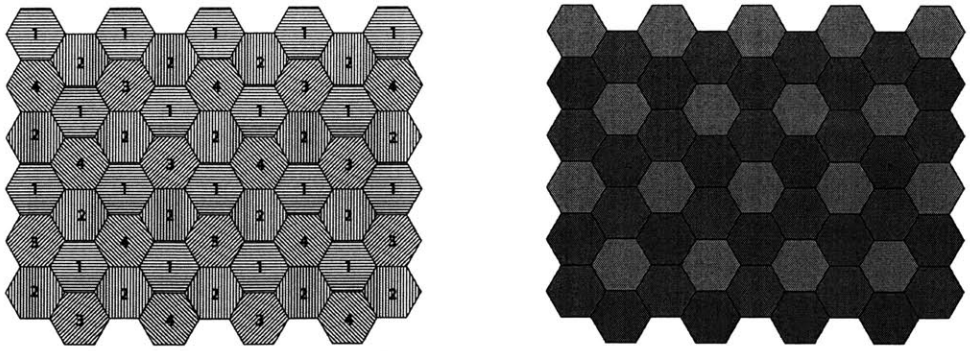

(a) (b)

Figure 1-3: (a) Hexagonal mosaicked array of linear polarizers; **(b)** Hexagonal mosaicked array of color filters

1.3 Applications and Motivation

The following several sections provide motivation and application for MPMFA technology. In general, the motivation driving the development of MPMFAs is to increase the effectiveness of current IR imaging system in object discrimination, detection, and recognition; to increase the number of applications for uncooled infrared sensors; and to ultimately save lives.

Possible applications come from military, security, law enforcement, first-responder, hazmat, fire fighting, search and rescue, automotive and aircraft safety, medicine, home monitoring, and environmental sensing.

1.3.1 Military, Paramilitary, Law Enforcement, and Security Applications

It is difficult to sort possible applications of MPMFAs into neat, distinct categories. Although what might be useful to military users could also be useful to fire fighting or medical users, in this thesis, possible applications have been grouped with users that have the greatest demonstrated need in that area.

Night Vision and Enhanced Vision

Currently, state-of-the-art systems for both night vision and enhanced vision involve the fusion of LWIR thermal images with NIR and visible-wavelength images. Such sensors are of great interest to the military, especially for use by dismounted soldiers in battlefield conditions.

LWIR and MWIR radiation transmits more readily and with less scattering through smoke, dust, and chemical obscurants than visible radiation. However, LWIR images have significantly lower contrast than visible color images. Therefore, by fusing the two together, once can achieve high-contrast images in normal conditions, and low contrast, but useful images in the presence of aerosol obscurants. Additionally, the use of such systems are ideal in environments with large amounts of pollutant laser radiation; while the human visual system may be overcome with coherent laser radiation, battlefield lasers (whether as target designators, dazzlers, or laser weapons) are outside the designed waveband range of head-mounted or weapon-mounted LWIR and MWIR sensors [7].

Battlefield conditions also dictate certain properties that a multispectral polarimetric imaging system must have:

1. **Real-Time Image Fusion of Sensor-Obtained Imagery**

   An imaging sensor must be able to provide fuseable data to an onboard computer. The system must operate at a frame rate that does not disorientate the soldier (for head-mounted displays and rifle sights). The sensor fusion must require minimal or no input from the soldier and must be easily useable and its settings user-adjustable. The use of polarization and wavelength as discriminants in such a sensor will enhance its ability to provide useable data to object discrimination and recognition systems. The sensor and display should provide false-color information to the user in a way that maximizes the information-processing capability inherent in the human visual system. The display should be adjustable to the preferences of the user and should adapt to changes in environment and situation. For instance, sometimes finding man-made objects

may be a primary goal, while at other times not a goal at all. Therefore, the user should be able to enhance polarization signatures when looking for man made objects and decrease such enhancement when not.

2. **Ability to Transmit Sensor-Gathered Data in Network-Centric Battlefield**

   The sensor must interface well with new technologies enabling soldiers to communicate battlefield conditions, targets, and movement with other units as well as command and control. Therefore the sensor should be easily integrable into existing and future systems. Additionally, the sensor should be able to provide information at a higher level than just pixel-level intensities. By analyzing polarization and spectral signatures, it should be able to mark objects or areas within a scene as man-made, naturally-occurring, or as possible human contacts along with each of their geospatial coordinates and transmit this data instead of just a raw image.

3. **Small and Unobtrusive**

   Soldiers must navigate obstacles, move quickly from target to target and from location to location with the greatest possible ease. The size of the sensor must facilitate soldier movement while standing, squatting, crawling, and rolling through brush and debris.

4. **Low Weight**

   Soldiers have limited carrying capacities, and the weight of helmet-mounted or weapon-mounted goggles/sights must be minimized. A single MPMFA within a weapon, instead of additional moving parts, or multiple bore-sighted imaging systems can help reduce weight.

5. **Low Power and Long Battery Life**

   The sensor should be useable for long periods of time, a great majority of which it will be in a persistent-on state. It should only use as little power as necessary to ensure that it is useable when needed on the battlefield. The sensor should

not contain power-hungry components such as motors or servos.

6. **High Resolution**

   High resolution imagery is important for object discrimination. The mosaicked-filter concept can provide much higher resolution images for battlefield situational awareness as it relates to multispectral data than can systems that use multiple sensors. Resources can be spent on developing larger microbolometer arrays instead of allocating resources to bore-sighted optical systems or on complex optical systems with multiple sensors, one for each waveband of interest.

7. **Low Maintenance and High Reliability**

   By eliminating moving parts in a MPMFA-centric sensor, one increases the reliability and decreases the amount of maintenance necessary for such an imaging system. The MPMFA eliminates moving parts in the optical filtering stage of a multispectral imaging sensor and therefore is much more rugged, durable, and reduces maintenance.

8. **Wide Field of View**

   A common need for soldiers is to have a wide filed-of-view. By using easily-manufacturable filtering technology with high-density imaging sensor arrays, once can increase the number of useable pixels available for imaging a scene. With more pixels comes the ability to increase field-of-view while maintaining reasonable image fidelity. MPMFA technology is scalable to arrays of any practical size, and therefore complements the production of larger detector arrays.

9. **Long Range**

   The sensor should be able to see objects-of-interest at great distance. In addition, it should be unobtrusive enough not to be seen or distinguishable by an enemy at much shorter distances. By optimizing the MPMFA as to transmit as much light as possible in the desired wavebands, we extend the range of such multispectral sensors.

10. **Uncooled**

    Cooling a sensor array requires additional electrical or chemical power. A sensor's increased complexity when integrated with a cooler decreases its reliability and increases the sensor's size and weight. Therefore, the MPMFA should be coupled with currently manufacturable technology that allows for uncooled operation in the MWIR and LWIR. Currently, microbolometers can operate in both the MWIR and LWIR, uncooled [8, 9]. More about the mating between our proposed MPMFA sensors and microbolometers is discussed in this thesis.

11. **Cost**

    Multispectral polarimetric imaging sensors need to be inexpensive enough to appropriate and field in large numbers. In the military, this is often referred to as 'cost containment.' While the sensors do not have to be inexpensive *per se*, it is ideal that we enable different companies and organizations to manufacture these sensors with minimal change to how they currently build filters or silicon devices. By enabling competition and rapid increases in production ability, the cost of such sensors is more stable, and changing military or civilian demands can be met.

Target Acquisition

Both the military and law enforcement have shown recent interest in sniper-location systems. Studies have demonstrated that muzzle flash lasts between 1 and 3.5 milliseconds and usually produces between 0.5W/ster to 10W/ster in the LWIR and between 5w/ster and 10w/ster in the MWIR. Currently, most sniper location systems use LWIR-sensing despite the lower intensities than MWIR-sensing would produce. This is due to solar-induced background noise as well as specular reflectance in the MWIR [10].

For Intelligence, Surveillance, Target Acquisition, and Recognisance (ISTAR), multispectral polarimetric sensors hold great promise. This includes search and rescue, but deals more with targeting for military or intelligence purposes. Such sensors

may be part of a dismounted soldier's helmet, may be attached to a UAV or a micro-UAV or attached to any form of land or sea vehicle [11]. Multispectral polarimetric sensors have the ability to distinguish between camouflage and natural backgrounds, or even to see through camouflage to what lies beneath.

Currently, multispectral image fusion systems (visible and LWIR, mostly) use image intensifiers for visible and near-infrared radiation during night-vision operation. Image intensifiers experience halo effects in the presence of bright sources, and are also bulky, relatively low resolution, and usually have a narrow field of view. For true multispectral night vision, coupling a multispectral polarimetric mosaicked imaging sensor with a low-light CCD, as produced by Lincoln Laboratory, could create a vastly improved solution [12, 13].

Law Enforcement Specifics

Law enforcement applications are quite similar to military needs, especially for paramilitary applications like SWAT. However, law enforcement officers are much less likely to need the same long battery life and durability necessary for battlefield conditions. Since law enforcement do not always carry weapons, and are not likely to use head-mounted displays during searches, sensors for law enforcement application are more likely to take the form of hand-held imagers or binoculars. Still, many of the requirements stated before remain.

The most common use by law enforcement will most likely be for search and apprehension operations. This might include search for suspects hidden in brush or foliage or in shadows.

Additionally, inexpensive multispectral sensors could be used in homeland defense by law enforcement or security officials. Multispectral sensors can be used to image public areas, looking for the spectral traces of chemical weapons. Multispectral sensors can be used in daytime or nighttime scene size-up, and help indicate not only the location of people, but possible chemical toxins and other dangers (running cars, fires, etc.) [14, 15].

Currently, law enforcement use smoke and other obscurants to disperse and control

crowds. Inexpensive multispectral sensors could be used to see through the smoke and distinguish between officers and mob participants.

Search and Rescue

In the case of terrorist attack, or catastrophic failure of buildings, when there are significant smoke and other aerosol obscurants, multispectral imagers could be used to see through such smoke for more rapid search and rescue operations.

Additionally, for the more common situation of hikers becoming lost in fog, near forest fires, in snowy or white-out conditions, or in dust storms, multispectral polarimetric sensors can aide in rescue operations. With the ability to see through such obscurants in addition to identifying man-made objects, a single search and rescue unit can search a much larger area in less time. An example might be a plane equipped with a multispectral polarimetric sensor. If a car falls off a road into a ravine during foggy conditions, it is often difficult to locate the vehicle from either airborne or land-based vehicles. With a multispectral polarimetric sensor, a search team can see through fog and identify the car (a man-made object) even if obscured by light dust or light foliage: the car can be identified by its polarization signature, temperature differences between car and the background, and through specular solar reflectance.

Along the shoreline, multispectral polarimetric sensors can be used to identify possible intruders into sensitive facilities or for lifeguarding. The high polarization water and the low polarization of a swimmer in daylight in addition to the thermal difference between the water and the swimmer during the daytime or nighttime can lead to faster identification of swimmers in trouble and increase the probability of rescue.

Put simply, if we can field enough multispectral polarimetric sensors at a low cost, with high reliability, and ease of manufacture, lives can be saved. Cost, unfortunately, is one of the largest factors in whether or not a technology is accepted and used. By using COTS (commercial-of-the-shelf) parts, inexpensive filtering technology and smart design, we can increase the probability that systems will be designed, fabricated, and used.

XM29 Rifle

The XM29 is the Army's newest state-of-the-art infantry rifle. This weapon is being designed to replace the M4 and M16A2 rifles currently in use. This riffle integrates dual barrels; target acquisition, fire, and control systems; direct view optics and a thermal imager; and is capable of both day and night operation. As part of the Future Force Warrior program, this riffle offers data communication, uplink to head-mounted displays, laser range finding and timed air-burst munitions capable of incapacitating enemies behind walls and other fortified targets [16].

The weapon, as currently designed uses a Vanadium Oxide microbolometer for thermal imaging and an optics train that allows for 90% probability of personnel and vehicle detection at 500meters under low clutter conditions.

A multispectral and polarimetric capability could be easily integrated into such a system, to add the many object recognition and detection benefits as discussed in this document. Since microbolometers have a wide spectral range, it would primarily a filter integration problem instead of an electrical readout or detector design problem. The multispectral polarimetric mosaicked filter array technology thus far discussed can be abutted to the sensor with minimal redesign of the optics train to give additional capabilities above and beyond a wideband LWIR sensor. Or, as discussed in a later chapter, a single-layer metallic-grid spectro-polarimetric filter can be integrated into the fabrication of the microbolometer. The XM29 is good an example of low costs IR sensors being equipped on mobile infantry units and a niche in which the MPMFA technology can add benefit.

Mine and Unexploded Ordinance Detection

Unexploded ordinance (UXO) detection has become a major area of research as-of-late due to several humanitarian and geopolitical factors. These include de-mining efforts around the globe in addition to military action in Iraq.

Currently, significant research is going into mine detection in the IR using LWIR multispectral and polarimetric signatures. The MPMFA fits a need for an integrated

filtering technology that can accelerate the development and deployment of mine detection senors.

Polarization studies of land mine materials and environments in which such mines might be found have shown that: 1. soil is effectively unpolarized and 2. the degree of linear polarization for CARC (Chemical Agent Resistance Coating), Silicon Rubber, and various plastics is between 0 and 0.03 depending on IR wavelength. The degree of linear polarization is defined as

$$\text{DoLP} = \frac{I_p}{I_u + I_p} \tag{1.1}$$

where DoLP is the degree of linear polarization, I_p is the intensity of polarized light from the object, and I_u is the intensity of unpolarized light from the object [17].

Additionally, these studies have shown similar partial polarization from cut wood and asphalt similar to that of materials used in mine making. This presents a difficulty in using just polarization to detect UXOs [17]. Thankfully, one can also use multispectral data to eliminate ambiguity.

From recent studies, various spectral predominances particularly suited for object discrimination of environmental and man-made objects have been determined. A few are listed here:

Chemical/Material	Spectral Peaks
Water Vapor	2.7μm, 6.3μm
CO_2	4.3μm, 15μm
CARC	8.73μm, 9.23μm

In general, broad waveband bandpass filters and sensors do a poor job of eliminating clutter, so specifying specific wavebands within the MWIR and LWIR for a multispectral mosaicked sensor is desired.

Additional recent studies have shown that digging can be detected by looking for moisture differences between disturbed and undisturbed soil. This can be advantageous in detecting recently planted UXOs, for search and rescue, or for criminology and forensics [18, 19, 20].

However, for object detection to work, multispectral images must be perfectly registered as well as acquired with near simultaneity. Small polarization differences between objects and their surroundings can easily be washed out with small temperature shifts between image acquisitions or by small changes in solar irradiance. The MPMFA technology eliminates these problems because of its ability to simultaneously distinguish polarization and spectral signatures. However, because the MPMFA uses interpolation to determine relative intensities of neighboring micro-pixels, objects that image to an area smaller than a macro-pixel on the MPMFA may not be detected. It is possible to adapt an MPMFA-based sensor to take multiple frames in rapid succession and stitch them together to create a higher resolution image. Such a technique works by using the normal swaying motion of a camera held by a human operator and is similar to digital motion stabilization techniques.

Ground Sensors for Facility and Home Monitoring

Possible applications for inexpensive multispectral imaging arrays exist in the field of facility and home monitoring. With inexpensive, low resolution microbolometer arrays, one can pattern mosaicked multispectral polarimetric imaging arrays that can provide much more useful information than motion detectors or visible cameras. Because of temperature differences between people wearing clothes and an animal, in addition to polarization shifts in a scene when man-made objects enter a frame (such as a car or a wrench), inexpensive multispectral IR sensors can be used to determine if a possible intruder is a person, and animal, on a vehicle, or carrying tools [21]. These filters can also be used to help detect fires and provide monitoring for areas around pools (using the large temperature and polarization differential between people and water) for improved home safety.

1.3.2 Chemical and Environmental Monitoring and Hazmat Applications

Hazmat (hazardous material) teams can use multispectral imagers to determine the location of gas clouds or ground-level pollutants. Such sensors could help in cleanup and evacuation efforts. On the battlefield, such systems, coupled with other distributed chemical sensor technologies, can search for and warn of possible uses of chemical weapons.

Multispectral sensors, using dual-wavebands have been shown to accurately detect chemicals such as Methanol, DMMP, and DIMP within the $\lambda = 8 - 12\mu$m waveband [22]. Such sensors may be capable of detecting industrial chemical contamination and leakage in addition to chemical weapons. Inexpensive multispectral imaging systems that can be distributed to first responders, security, and hazmat crews could aid in timely evacuation and response. Indeed, such sensors do not need to identify specific chemicals, they only need to identify the presence of unexpected chemical agents so that first-responders may issue a warning. Problems associated with such sensors include wide variations in background temperatures (which greatly complicates spectral comparison and detection routines), and so expanding the waveband of current LWIR detectors to the MWIR may be helpful. By moving to the MWIR, one may detect chemicals with signatures whose spectral peak intensity lies outside of the background blackbody radiation range of the LWIR.

Multispectral chemical sensors can also be placed in high-risk areas for volcanic eruption, where multispectral sensors can detect or see through chemicals present in volcanic clouds. Possibilities in multispectral imaging may also lead to better water management on farms from monitoring evapotranspiration, and therefore determining when and how much water plants need [22].

1.3.3 Fire Fighting and Forestry Applications

Fire fighting applications are broken down into two primary application areas. Forestry fire fighting deals with fires on large scales, often in forested or chaparral-dense areas.

These fires endanger firefighters' lives due to high winds, rapid changes in fire direction and intensity, and because of the vast landscape over which such fires may burn. Urban and suburban fire fighting, covers the extinguishing or controlling of fires in man-made structures or population-dense areas. Such fire fighting entails working in the confined, dangerous spaces in both residences and commercial buildings.

Forestry Fire Fighting

Current fire-line detection techniques fail to adequately address the needs of modern firefighters. Current imaging systems used by firefighters rely on LWIR thermal imaging. With LWIR imaging, it is difficult to distinguish between hot ash and active fire due to the high temperatures involved with active flames. Forest fire flames may reach up to 1200°C [23]. This corresponds with a blackbody source whose peak radiant intensity is at $\lambda = 1.97\mu$m (for the reader's benefit, the core temperature of an average human is about 37°C and the minimum external temperature (at the distal end of the legs) may be as low as 22°C in a cold room (freezer temperatures), this corresponds to a black body source whose peak radiant intensity is $\lambda_{37^\circ} = 9.34\mu$m or $\lambda_{22^\circ} = 9.81\mu$m–perfect for LWIR imaging) [24]. In other words, the peak intensity for flames is at the border of the NIR and MWIR. A multispectral imager that can discern between ash and flames, as well as discern man-made objects would be of great use to firefighters and the forestry service. Additionally, small spectral bands tend to be good for fire mapping due to the high contrast between two narrow spectral bands [23]. However, true multispectral imaging brings out terrain features better. So a mosaicked multispectral sensor would enable both functions at the same time and in the process improve reaction times, safety, and coordination between firefighters.

Urban/Suburban Fire Fighting

Another benefit of having a mosaicked multispectral sensor, is that is it more difficult to blind due to sudden flashes centered about a specific wavelength. Firefighters often face ambient temperatures of 150°C to 350°C and backdrafts or flashovers of over 500°C (this corresponds with peak blackbody radiation at $\lambda_{150^\circ} = 6.85\mu$m, $\lambda_{350^\circ} =$

4.65μm, and $\lambda_{500^\circ} = 3.75\mu$m respectively) [25]. If a sensor is wideband, then the high ambient temperature or acute temperature of a backdraft or flashover can oversaturate a wideband imaging sensor. By using a mosaicked filter array, only a few micro-pixels in each macro-pixel will oversaturate, allowing the firefighter to still see escape paths or victims using the unaffected pixels.

1.3.4 Automotive and Aeronautics Applications

Recently, several companies have begun developing and fielding sight enhancement technologies to make automobiles safer. This includes thermal IR imaging sensors used to see through fog for the purpose of crash avoidance [26]. Currently, the LWIR band from $\lambda = 7.5\mu$m to $\lambda = 13.5\mu$m has been preferred in such systems because of less atmospheric and aerosol clutter than in the MWIR as well as increased spectral energy in those wavelengths at normal daytime and nighttime temperatures [27]. In California, the author's home state, it is not uncommon to have heavy fog along the coast, dust storms inland, and large fires raging in regions of chaparral. All these conditions lead to many deaths and many more injuries every year in pileups and single and multiple car accidents. By integrating multispectral sensors that can see through obscurants with IR polarization sensors that can distinguish road from berm, it is is hoped that many such accidents can be avoided.

The MPMFA technology presented here also has the benefit of being reliable in harsh environments. Since there are no moving parts, and we are relying on uncooled imaging array technology, such sensors can go from snow to warm desert, from low humidity to high humidity without undue risk of mechanical failure or breakdown. Additionally, constant road shock can damage sensitive moving parts, and as MPMFA technology is solid-state, it is inherently tolerant to large vibration and shock loads.

In the realm of Aeronautics, multispectral polarimetric sensors could help small planes with a cost-effective way to see through fog and runway obscurants, and better allow air traffic control to monitor ground traffic on runways and taxiways in the presence of fog. The use of polarization could also allow planes to better distinguish runway from unpaved surfaces and help distinguish planes from runway in the case

when both are thermally similar.

1.3.5 Medical Applications

While polarization sensitive applications in the medical field are as of yet unknown, multispectral imagery does have potential applications in the burgeoning field of infrared medical imagery. One possible applications of multispectral imaging in medicine includes endoscopic heart surgery, using thermography [24] to look for adequate perfusion after treatment for coronary artery stenosis or myocardial infarction.

At this point, medical science does not have a strong grasp on all the metabolic processes involved with good health, as there has not been thorough thermographic medical studies of the human body. To the level that such thermography will enable physicians to better diagnose certain health problems is at this time uncertain [28].

Thermographic studies of dialysis grafts, aneurisms, and stenosis have been performed, but not in great detail. Studies have also been performed on extravasation (IV burns, where chemicals leak out from an IV into tissue surrounding a vein) with initial determination that such imaging methods deserve broader study [29].

1.3.6 Astronomical Applications

In large telescopes, both orbital and terrestrial, the 1-5um waveband is very important [30]. Many telescopes use multiple sensors within a beam path to image different wavebands from the ultraviolet to the visible to the IR. Whether these telescopes use pick-off mirrors, wavelength-dependent dichroic beam splitters, filter wheels, or multiple independent boresighted telescopes, these imaging systems tend be very complex. Because of this complexity, these telescopes also tend to be very expensive to build, operate, and maintain.

The MPMFA technology discussed in this document represents not a replacement, but an addition to the abilities found in astronomical telescopes around the world. In no way can or should a mosaicked sensor replace the high-resolution sensors found in space telescopes such as Hubble or in ground telescopes such as the Keck Observatory,

but such sensors may be useful in markets where cost is a major factor. A combination of microbolometer technology and MPMFA technology could potentially give the hobbyist astronomer tools unlike those available anytime in modern history. For multispectral infrared imaging of the cosmos, a mosaicked sensor would be much cheaper than several interchangeable sensors, or even filter wheel technology that has been present in many multispectral imaging applications.

The benefit to mosaicked technology over filter wheel technology (the current least expensive option for multispectral imaging) as it relates to both astronomy and other fields thus far discussed is the ability to image multispectral events on vastly different timescales. The tradeoff is that for increased multispectral resolution in terms of wavelength for fast events, we must give up some multispectral resolution in terms of transverse pixel resolution for slow events. A meteor hurtling through the atmosphere is a fast event that can not be viewed well with filter-wheel technology, since only one wavelength can be seen by the sensor at a time. On the other hand, the moon moves very slowly across the night sky, lending itself to filter wheel technology where one image is taken with one filter, then another image or sequence of images is taken at additional wavebands. In both cases, the images are either interpolated or superimposed to create a false-color image of the object. Mosaicked filter technology retains the benefit of being both high resolution in the transverse pixel domain, through modern interpolation techniques, as well as high resolution in the wavelength domain (multispectral) for both fast and slow events.

In space-exploration, MPMFA technology also finds a potential application. Rovers, such as those sent to Mars, incorporate advanced imaging sensor technologies for navigation, chemical analysis, and geological analysis [31]. Currently, the cameras used for such exploration are one-of-a-kind or made in small production runs and are predominately proprietary technology that use some space-qualified COTS parts. This is costly, but with just a few rovers, not necessarily a problem for well-funded space exploration programs. In the near future, NASA will begin sending multiple rovers to Mars and perhaps other planetary bodies. Indeed, when we start sending hundreds or even thousands of rovers–each very small, light weight, and expendable–we will need

less expensive imaging technology that is compact, rugged, and able to gather the scientific and explorative knowledge necessary for rover operation. MPMFA fits into the scheme nicely. In the infrared, MPMFA provides ruggedness (no moving parts), it provides compactness (vital for minimizing size and weight of a rover), it provides multispectral infrared data (that is useful in chemical analysis, thermal analysis, and navigation), it allows for polarization analysis, and it is potentially very inexpensive compared with multiple sensors.

MPMFA technology can also be used in micro-satellites (microsat) or even nano-satellite (nanosat). Such satellite technology requires extremely low-weight and compact components [32]. For gathering as much imaging information as possible, while still having low weight, compactness, ruggedness and low cost, MPMFA may be an option for earth-viewing microsats. Such micro-satellites could be used in man-made object detection and recognition, forest fire imaging, and a gamut of other imaging application where multispectral IR imagery and polarimetry may be useful. Specifically, MWIR is useful in viewing hot thermal events on earth, and can be useful not just in detecting rocket launches as with Space-Based Infrared (SBIR) [33] but also measuring and monitoring volcanic activity and forest fires.

1.4 State of the Industry

Infrared filters have found applications in military, civilian and law-enforcement applications. Recently, advances in microbolometer and MEMs-based infrared filters have begun to revolutionize the field of infrared imagery. Modern detector arrays far surpass those of just a decade ago in number of detector elements, in speed, and in sensitivity. Additionally, recent advances in infrared detectors have expanded greatly the number of potential applications for those detectors. Currently, uncooled (or TE-cooled) infrared detectors are becoming mainstream. These detectors, bolstered by advances in MEMs processing, stand to revolutionize the infrared imaging industry.

With new advances in infrared detector technology must come advances in infrared filtering technology. Smaller, more sensitive detectors require new technology for

front-end spectral and polarimetric filtering. Additionally, new applications demand increased performance and decreased cost of both filters and detectors.

1.4.1 Low-Cost Distributed Sensor Platforms

Currently, there is a push in both the civilian and military communities to increase usage of low-cost options for imaging systems. Primarily, this push stems from the relatively costly practice of designing and developing special-use imaging equipment in order to meet the specialized needs and specifications for a particular imaging system. The clients for such imaging systems expect both reliability and low-cost. Shrinking military budgets for high-cost single-use items has pushed imaging system manufacturers to turn to commercial off-the-shelf (COTS) components for their imaging systems. Additionally, the end-users of such systems have adapted their design specification to equipment that is currently available or easily adaptable to their needs.

There has also been much current work done in distributed sensors. Whether these distributed networks of sensors are used to monitor seismic activity in the civilian world or maintain battlefield awareness in the military sector, such distributed sensor systems must be inexpensive, massively reproducible, small, robust packages.

Many civilian and military surveillance applications, call for tens, hundreds, or even thousands of sensors located throughout an area of interest. Such sensors need to be able to handle unknown (or not well-known) environments. They must be inexpensive enough so that loosing a large number of the sensors does not create difficulties in replacement. The sensors must be massively reproducible with short turn-around times in production to ensure that supply can always meet demand. The sensors must be small enough and unobtrusive enough so that they may perform their surveillance without being an obstruction or being detected as the case may require. Additionally, they must be small or compact so that they may be easily deployed. And finally, the sensors must be robust; they must stand up to the harshest of environments. This may mean deployment in caustic environments, environments with high-vibration, very cold or very hot environments, humid or dry environments,

and environments of differing atmospheric pressure.

1.4.2 Adapting to COTS Needs in Modern Military and Civilian Applications

Due to the increased demand to incorporate COTS options with new imaging systems, we must look to every option of reducing the cost of our sensor/filters by using technology that currently exists and is easily adaptable to our needs. In doing this, this thesis focusses attention on looking specifically at currently realizable methods of manufacture and design.

The multispectral polarimetric filters briefly described in the previous sections of this thesis assume the use of COTS IR focal plane arrays. Additionally, the availability of inexpensive foundry and deposition services to create these filters is also assumed. Additionally, proof-of-concept engineering has been performed using MOSIS foundry services to produce multi-layer metallic grating filters using a standard CMOS 0.5μm process. This work is presented in Chapter 5.

1.5 Background and Previous Work

In Don Kim's doctoral thesis performed here at the Photonic Systems Group at MIT [34], he describes many related projects involving multispectral polarimetric imaging platforms. Included here are the names of these devices as well as appropriate references for each; however, a more comprehensive summary of these devices can be found in Kim's thesis: Earth Observing Scanning Polarimeter (EOSP) [35, 36, 37, 38], Polarization and Directionality of Earth Reflectances (POLDER) [39], Acousto-Optic Imaging Spectropolarimeter (POLARIS II) [40], Fourier Transform IR Spectropolarimeter (FTIRSP) [41, 42, 43], Remote Minefield Detection System (REMIDS) [44], Imaging Multispectral Polarimeter [45], Channeled Spectrum Spectropolarimetry [46], Prism spectrophotoprofilimeter [47], Computer-Tomography Imaging Spectrometer (CTISP) [48]. Single-band multiple-polarization systems include: MWIR

Polarization Sensitive Thermal Imager [49], Diffraction-Grating Photopolarimeter [50, 51], Airborne MWIR Polarimetric Imager [52], Prism-based Imaging Polarimeter [53], Single Shot Polarimetry Using Wedged Double Wollaston [54], Wire-grid Polarizer Arrays Patterned with Microlithography [55].

Additionally, other previous technologies include:

1. **Multispectral Infrared Stokes Imaging Polarimeter**, which measures all Stokes parameters in both MWIR and LWIR [56, 57]. This device uses quarter wave linear retarders for achromatic quarter-wave linear retardation in conjunction with linear polarizers. This device is a 512x512 imager, and although it covers the MWIR and LWIR, it does not cover multiple wavebands in either. It also requires rotation of the filtering element.

2. **Multi-band Infrared Imaging Radiometer**, which utilizes four abutted pyramidal prisms to create four separate images, each from a separate part of the 3-5μm MWIR waveband [58]. The benefit of this design is it is simplified from similar lenslet-array-type designs. This system does not accomplish polarimetric imaging.

3. **Field-Portable Imaging System for Field-Classification**, which is a complete target / background discrimination system [59]. This device combines 12 wavebands from UV to LWIR with 5 CCD cameras and 2 IR imagers, all boresighted to the same telescope. This system does not accomplish polarimetric imaging.

4. **Field-Portable Imaging Radiometric Spectrometer**, which uses an LWIR (8-11.5μm) FPA as part of a Fourier-transform spectrometer, and is primarily intended as a chemical sensor, but can be used for other hyperspectral applications [60]. This system does not accomplish polarimetric imaging.

5. **Multispectral Thermal Imager (MTI)**, which is aboard a research satellite sponsored by the US Department of Energy [61]. This multispectral imager

is designed for passive characterization of industrial facilities and environmental impact. The imager can view 16 separate wavebands from visible through LWIR. It has two bands in the MWIR and three bands in the LWIR, the choice of these bands will be discussed more in a the next chapter. This system does not accomplish polarimetric imaging.

6. **Landsat**. The Landsat series of satellites have provided multispectral images of earth's surface since the first Landsat mission was launched in 1972. Since then, there have been 7 total Landsat missions, with one launch failure of Landsat 6. Currently, both Landsat 5 and Landsat 7 are still operational [62]. Landsat 7, the most recent Landsat mission, has an Advanced Thematic Mapper + (ATM+), which can image eight spectral bands and download information via X-band at 150Mbps. Of those eight bands, two are in the MWIR and one is in the LWIR [63]. This system does not accomplish polarimetric imaging.

7. **Mars Global Surveyor**, launched in 1996 and arriving in orbit of Mars in late 1997, images the surface of Mars in one-hundred forty-two spectral bands from 6.25-50μm using the MGS Thermal Emission Spectrometer. Additional sensors measure light throughout the MWIR and LWIR [63]. This system does not accomplish polarimetric imaging.

8. **Airborne Imaging Radiometer (AIR)**, developed by Ball Aerospace, is designed for cloud imaging and sea-ice surface measurements. The device covers 10 spectral wavebands between 7μm and 14.5μm [64]. More on the specific waveband choices will be discussed in the next chapter. This system does not accomplish polarimetric imaging.

9. **Advanced Very-High Resolution Radiometer (AVHRR)** is a tool for testing the emissivity of terrestrial materials. Specifically, Salisbury, et. al., use it to determine reflectances from numerous natural materials in both the 3-5μm atmospheric window [65] and in the 8-14μm atmospheric window [18]. Both papers present comprehensive tables of reflectances for many forms of vegetation,

minerals, water, and ice. No data is provided with respect to polarization.

1.5.1 Continuation of Work Performed

The previous work, performed by Dong-Hyun Kim, for his Doctoral thesis [34], focused on creating "high and flat transmittance" polarizers using large-duty cycle 2.0μm pitch Al/Nb/Ti gratings on a silicon substrate. Kim also designed three-layer dielectric stacks for spectral filtering in the MWIR. Kim also proposed a solution of using multipitched polarizers or multiple polarizers in series [66]. Kim designed his spectral filters by means of a genetically-optimized search algorithm. Guided mode resonant effects were also discussed [67, 68]. Kim's ultimate recommendation was to put filters on one side of a substrate and polarizers on the other side of the substrate. With this configuration, since there is a large distance between polarizers and filters, there is a problem with high-order diffraction effects and signal contamination between pixels, which is addressed in this thesis through the use of sub-wavelength filters as well as coupled filters that do not rely on a flat polarizing-element transition curve.

In this thesis, alignment difficulties in the manufacture process of a combined spectral and polarimetric filter that were encountered in Kim's thesis are resolved and a solution to diffraction and cross-talk problems is presented.

Chapter 2

Waveband and Polarization Signatures of Interest

In the IR, we care about two spectral properties: emissivity (primarily in the form of black-body radiation) and spectral reflection (originating from direct reflection of sun light, from atmospheric scattering, or from light reflected within an emissive environment). The blackbody spectral radiance curve is described by the equation:

$$L(\lambda) = \frac{2hc^2}{\lambda^5(e^{hc/\lambda kT} - 1)} \left[\frac{W}{m^3 sr}\right] \tag{2.1}$$

where h is Plank's constant 6.626×10^{-24}J, c is the mks speed of light (2.9979×10^8m/s), λ is the wavelength of emitted light, k is Boltzmann's constant (1.3806×10^{-23} J/K), and T is the blackbody temperature of the emitting body measured in degrees Kelvin.

For most infrared imaging applications, when we are looking for the signatures of specific emissive sources, our primary concern is detecting temperature differences within an environment. However, we may also be looking for spectral features that come from molecular absorbance, or we may be looking for polarization signatures of emissive or reflected sources of IR radiation.

2.1 Atmospheric Window

Atmospheric scattering and absorption provides the main design criteria for most infrared imaging systems with significant stand-off range. Specifically, atmospheric absorption is of great concern in systems that incorporate telescope optics, or airborne and spaceborne systems that must "see" through a significant atmospheric layer. Atmospheric attenuation is caused by both scattering and absorption. Rayleigh scattering is caused by particles significantly smaller than the wavelength of incident light, λ. Rayleigh scattering is highly wavelength-dependent. Mie scattering occurs with particles on the order of or larger than the wavelength of incident light. Mie scattering is wavelength-independent and dominates in the IR.

Attenuation in the atmosphere, $\tau_0 = e^{-\beta x}$, where x is the length of atmospheric column, and β is primarily a function of wavelength, particle density, particle refractive index, particle conductivity, and particle size [69].

In the atmosphere, major absorbers are: ozone, water vapor, and other absorbing gases. At sea level, peak transmission in the IR occurs between 3-4.25μm and 8-10μm. In general, the IR atmospheric windows are considered to be 3-5μm (MWIR) and 8-12μm (LWIR).

2.2 Overview: Spectral Bandpasses of Significance

In the first chapter, several signatures of interest were already mentioned. Here, additional criteria for choosing a specific filter's characteristics based upon application in a multispectral, polarimetric imaging system are presented.

2.2.1 Emissivity Shift with Respect of Viewing Angle

In studies performed in the LWIR of surface emissivity vs. angle, important variation from Lamebertian emission were observed [70]. Jose Sobrino, et. al., have shown in their paper [70] that from 0-65° angle there was up to 7% change in emissivity from water and 1-3% change in emissivity for clay, sand, slime, and gravel. Interestingly,

homogeneous grass cover showed no emissivity dependence.

2.2.2 Spectral Wavebands Used in Current Imaging Systems

Current research has demonstrated operational feasibility for sniper location systems based on MWIR and LWIR imaging. Muzzle flash is an order of magnitude brighter in the MWIR (3-5μm) as the LWIR (8-12μm). However, in the presence of solar-induced glint and background clutter, LWIR proves more efficient [10].

For the field-portable imaging system developed by Evan Preston, et al. [59], they used three MWIR wavebands and four LWIR wavebands for object detection and discrimination (in this case, military vehicles) in the presence of aerosol and other obscurants. They chose the wavebands of 3-5.3μm (wideband filter) 3.5-4.1μm and 4.5-5.0μm (narrow band filters) in the MWIR and 8-13μm (wideband filter) 7.81-9.80μm, 9.98-11.41μm, and 10.497-10.857μm (narrowband filters) in the LWIR. Additionally, they used 5 other wavebands in the visible and UV [59].

The Multispectral Thermal Imager R&D satellite sponsored by the DOE for passive characterization of industrial facilities and environmental impact images in eleven spectral bands. However, only five of those bands, bands J through N, are used in infrared imaging [61]. In the MWIR band, two spectral bandpasses are used. The J band is from 3.50-4.10μm and the K band from 4.87-5.07μm. The MWIR bands are primarily used for daytime characterization. For nighttime and daytime water vapor characterization as well as Si_2O (quartz) concentrations, the L band, 8.00-8.40μm, and M band, 8.40-8.85μm, are used. One additional LWIR band, labeled N, is used. This one passes from 10.2-10.7μm.

The current LANDSAT 7 satellite uses three infrared spectral bands. These bands have been chosen through simulation as well as previous LANDSAT imaging satellite data. In the SWIR/MWIR, LANDSAT images in the 1.55-1.75μm spectral band for determining moisture content of soil and plants as well as for thin cloud penetration. In the high-frequency MWIR, the satellite images from 2.08-2.35μm for mapping hydrothermally altered rocks and mineral deposits. Additionally, a 10.4-12.5μm LWIR filter is used for thermal mapping and soil moisture mapping [63]. On the other hand,

the Mars Global Surveyor images in one-hundred and forty-three spectral bands from the low-frequency edge of the MWIR (6.25μm) all the way up to the FIR at 50μm.

The Advanced Very High Resolution Radiometer images with a 3.55-3.93μm filter for distinguishing green vegetation and water, a 10.3-11.3μm filter for temperature sensing of rough ice, and a 11.5-12.5μm filter for temperature sensing of rock, soil, and senescent vegetation [65]. The 10.3-11.3μm filter is chosen due to the reststrahlen bands (fundamental molecular vibrations) of ice.

In desert studies, the 3.55-3.93μm band has a much higher degree of reflectance than the other two bands [65]. Desert varnish, the coating of manganese, ferric oxide, and montmorillonitic clay on dessert rocks is masked by the strong Si-O reststrahlen band in the 8-14μm band.

Incidently, emissivity error (derived from Plank's law) is a factor of two less in the MWIR than in the LWIR. An emissivity error of 0.01 is 0.25°C at 4μm and 0.6°C at 10μm [65].

More information on senescent foliage reflection, various rocks and minerals, as well as ice and water may be found in Salisbury's 1992 and 1994 papers on emissivity of terrestrial materials both in the MWIR [65] and the LWIR [18].

2.2.3 Man-Made Objects

In mine-detection, several wavebands have proven useful as potential discriminants. Due to changes in soil water-content from recent soil disturbance, water vapor signatures can assist in mine detection. In the MWIR, specifically, a spectral peak at 2.7μm and another at 6.3μm can aid in soil disturbance detection [17].

Green CARC, a common plastic used in the military, has spectral predominances at 8.73μm and 9.23μm, enabling a two-band detection system with a narrow bandpass in each [17]. Green CARC also has spectral dips near 4.4μm that is about 0.2μm wide. There is another spectral dip at 3.4μm. MWIR peaks at 3.25μm and 4.0μm are approximately 0.9μm wide [71].

Tan CARC has a peak at 9.56μm and a dip at 9.16μm. In LWIR and MWIR band studies of a camouflage-netted M-60 tank against desert soil a 9.36/10.0μm band pair

showed considerable reststrahlen-induced coloring from silicate materials. However, in a background of grey grass, MWIR works better. With the tank on a background of scrub brush and soil, a 3.07/3.25μm band pair worked best in contrast enhancement [72].

An interesting result of a similar study by Schwartz, et. al., found that to achieve "good detection", which they define as a signal-to-clutter ratio of 7 or 8, for 90% of cases required three-or-more spectral bands. During this study, for both forested and desert backgrounds an optimized two-band set was found centered at 8.75μm and 9.10μm [73].

Brown painted metal, as is commonly found on military vehicles, has a nominal reflection of 0.05 and a peak of 0.12 at 9.1μm approximately 1μm wide. An additional peak exists between 3.5-5.8μm. The nominal reflectance for grass is 0.02 [20].

In a study of green-painted panels placed amongst vegetation, optimal spectral band pair selection was determined. All filters had a bandwidth of 100nm. The study used 8.73/9.23μm, 4.09/4.56μm, 3.75/4.00μm and 4.00/11.95μm pairs. The MWIR bands performed best at night and during the early morning (before the thermal crossover at approximately 7am). At all other times, the LWIR band performed best. Additionally, in this study single-band operation falls off as bands become wider than 0.2μm. This is because very narrow spectral features of the paint are being exploited for object detection and contrast enhancement. However, there is a tradeoff for sensitivity and SNR with the decreased filter bandwidth [74].

For mine detection, in the 9μm $\pm$ 1μm waveband, there has been an observed contrast difference of between 2% and 34% of disturbed vs. tamped vs. undisturbed soil emissivity [19].

In studies of surface mine detection in both short and tall grass environments image contrast differences between several spectral bands has been demonstrated. In Haskett's, et. al., study, several different mine types were observed in grass and non-grass environments. A 1-3% contrast difference was observed in the 3-5μm band versus the 3-4μm, 4-4.5μm, and 4.5-5μm bands. Additionally, 1-2pm sunlight created the best contrast. The 3-4μm region maximizes contrast at all times during the day

versus the other bands studied. Haskett attributes this to sunlight reflectance at 3-4μm has 30% better contrast than 3-5μm on average. Additionally, in non-senescent short grass, the 3-5μm and 3-4μm region shows significantly higher contrast than long grass [75].

In studies of man-made object detection, one study used 3.9μm, 4.7μm, and 4.7μm filters to differentiate a 2.5-ton truck, M60 tank, M-110 tank, HEMMT, 5-ton truck, and an M2 tank from natural backgrounds. The filters had 300nm spectral bandwidth. Additionally, CO_2-blocking filters from 3.6-4.1μm and 4.5-4.9μm were used. These studies, in the MWIR, were performed during daylight hours. The CO_2 filters were used to block vehicle exhaust signatures. However, fieldable systems, filters looking for the CO_2 features of running vehicles, or helicopters, could be useful [76].

2.2.4 Aerosol and Atmospheric Environment

For the detection of chemicals, such as methanol, dimethylmethylphosphonate (DMMP) – a chemical used in the synthesis of Sarin gas and used as a Sarin training simulant, diisopropylmethylphosphonate (DIMP) – a side-product of Sarin nerve gas production, and other toxic industrial chemicals, two-band narrow-bandpass systems have been used to differentiate and detect the presence of expected but unwanted aerosols. Such aerosols tend to have the highest level of differentiation in the 8-12μm regime [22].

For volcanic clouds, of especially recent concern, it has been demonstrated that a two-band detector, with center wavebands at 11μm and 12μm is able to assist in differentiation between clouds formed by condensed water vapor and clouds formed from volcanic ash. Volcanic eruptions themselves as well as forest fires (as opposed to smoke) show up best in the 3-5μm region [65]. This can be important for aviation, as volcanic clouds and natural clouds are difficult to distinguish in the visible. However, flying though volcanic clouds can lead to catastrophic engine failure.

2.2.5 Naval and Marine Environment

In studies of aerosol particle scattering above large water surfaces, significant scattering and refractive effects have been observed (such as mirages). This occurs when there is a large thermal variation between the water and air column above it. So, at temperatures significantly different between air and water, undesirable spectral and polarization effects can occur [77].

Indeed, additional infrared-refraction studies have shown that to achieve significant refraction of light across the ocean surface, the air temperature had to be at least 4-5°C cooler than the ocean or just 1°C warmer. Also, since there are many large aerosol particles near the surface of the water, there is much more absorption in the LWIR than in the MWIR–approximately three times as much [77].

Object	Em.,Absor. (E,A) Refl.,Trans. (R,T)	Waveband/ Wavelength	Bandwidth	Reference
People, External Temp Low (22°C)	E	9.82μm		Blackbody & Calculated, [24]
People, External Temp High (37°C)	E	9.34μm		Blackbody & Calculated, [24]
Ambient Atmosphere Low - Fire (150°C)	E	6.85μm		Blackbody & Calculated, [25]
Ambient Atmosphere High - Fire (350°C)	E	4.65μm		Blackbody & Calculated, [25]
Backdraft / Flashover - Fire (500°C)	E	3.75μm		Blackbody & Calculated, [25]
Fire (Forest) (1200°C)	E	1.63μm		Blackbody & [23]
Industrial Toxic Chemicals	E/R/A/T	8-12μm	Narrow	[22]
Volcanic Clouds	E/R/A/T	11μm and 12μm	¡1μm	
Sniper Location System	E	3-5μm, 8-12μm solar glint	Wideband Blackbody	[10]
Mine Detection: Soil Water	E/A	2.7μm, 6.3μm	Narrow	[17]
Mine Detection: CARC	E/A	8.73μm, 9.23μm	0.25μm	[17]
Vehicle Detection/Descrimination: MWIR	E/A/R	3-5.3μm, 3.5-4.1μm, 4.5-5.0μm	Wide and Narrow Band	[59]
Vehicle Detection/Descrimination: LWIR	E/A/R	8-13μm, 7.81-9.80μm, 9.98-11.41μm, 10.497-10.857μm	Wide and Narrow Band	[59]
Atmospheric Peak Transmittance	T	3-4.25μm, 8-10μm		[69]
MTI DOE Satellite: Daytime Characterization	E/R	3.50-4.10μm, 4.87-5.07μm		[61]
MTI DOE Satellite: Water Vapor and Quartz	E/R	8.00-8.40μm, 8.40-8.85μm, 10.2-10.7μm		[61]
LANDSAT 7: Moisture Content Plants and Soil	E,R,T	1.55-1.75μm		[63]
LANDSAT 7: Thermal Mapping and Soil Moisture	E	10.4-12.5μm		[63]
LANDSAT 7: Hydrothermally Altered Rock & Minerals	E,R	2.08-2.35μm		[63]
Mars Global Surveyor	E/R/A/T	6.25-50μm	143 equally-spaced channels	[63]
AVHRR: Green Vegetation and Water	E/R	3.55-3.93μm		[65]
AVHRR: Temperature Sensing of Rough Ice	E/R	10.3-11.3μm		[65]
AVHRR: Temp Sens. Rock, Soil, and Senescent Veg.	E/R	11.5-12.5μm		[65]
AVHRR: Hydrocarbon Absorption Band Troughs	A	3.4μm, 3.5μm		[65]
Disturbed Soil vs Undisturbed: High Contrast	E/R	9μm	2μm	[19]
CO_2 Absorption Line for Vehicle Identification	A	4.2μm		[75]
Mine Contrast Enhancement: MWIR	R	3-5μm¿ 3-4μm, 4-4.5μm, 4.5-5μm		[75]
Military Vehicle Detection	R	3.9μm, 4.7μm, 4.3μm	0.3μm	[76]
Green CARC	A	4.4μm (trough), 3.4μm (trough)	0.2μm	[71]
Green CARC	R	3.25μm (peak), 4.0μm (peak)	0.9μm	[71]
Tan CARC	R	9.56μm (peak), 9.16μm (trough)		[72]
Tan CARC vs. Scrub Brush and/or Soil	E/R	9.36/10.0μm (just soil), 3.07-3.25μm (scrub)		[72]
Desert and Military Vehicles (Optimal 2-Band Set)	E/R	8.75/9.10μm		[73]
Green Painted Panel (Metal) in Vegetation	E/R	4.49/4.56μm nighttime, 8.73/9.23μm daytime	0.1μm	[74]
Brown Painted Panel (Metal)	E/R	9.1μm, 3.5-5.8μm	1μm, 2.3μm	[20]

Table 2.1: Potential signatures of interest in the infrared as documented in the literature.

2.2.6 Spectral Curve Bandwidth

The choice of bandwidth is highly-dependent on application, but there are a few general rules a designer can follow. For most thermal imaging applications, ideally a broadband signal of bandwidth $> 1\mu$m is desirable. This includes: black-body signature recognition in the MWIR and LWIR and reflection signatures in the MWIR (from the sun and surroundings). Broadband ($>1\mu$m) bandwidth filters are ideally suited for object *detection* due to the increase in available photons, and the subsequent increase in signal-to-noise in an image, and due to the smoothing effect over environmental irregularities (chemical obscurants, aerosols, etc.).

Narrowband signatures ($<1\mu$m) are best suited for chemical absorption signatures and emission signatures (e.g. CO_2 from vehicles) in the LWIR. Narrowband signatures are also best for clutter reduction and object *discrimination*.

For object detection and recognition at large stand-off distances, the most promising choices of spectral regions-of-interest within the IR bands, due to atmospheric absorbance, is 3-4.25μm in the MWIR and 8-10μm in the LWIR. An overview of spectral bands and bandwidths of interest can be found in Table 2.1.

2.2.7 Spectral Curve Overlap

For wideband signatures, it can be advantageous to have overlap between each passband. In general, moderate transmission curve overlap from adjoining passbands is better than no overlap at all [78, 13]. This is especially true when using neural-network or retinal-models for contrast enhancement of low-contrast signatures (e.g. polarization or spectral differences in the MWIR and LWIR).

2.3 Overview: Polarization Signatures of Significance

Polarization in the MWIR and LWIR can come from either electromagnetic emission or reflection. More commonly, MWIR-originated polarization is due to reflection from

dielectric surfaces. In the LWIR, polarization comes from both reflection (surrounding thermal radiation reflects from dielectric surfaces) and emission.

Common sources of IR polarization include waxy surfaces (e.g., leaves), plastics (e.g., mines), cut or altered surfaces (such as wood chips or bark), and flat objects or objects with faceted surfaces (e.g., asphalt, vehicles, man-made or man-altered installations).

Polarization also depends on time of day. During the day, MWIR light tends to have a dominant TE component and LWIR light tends to have a dominant TM component. During the day, LWIR, in the natural environment, almost always exhibits a greater degree of linear polarization than does MWIR light.

Additionally, specular reflection dominates the scene when sun light or moon light shares a common plane of incidence, and thus reflective polarization effects dominate.

For the most part, MWIR and LWIR polarization is a a result of dielectric emission and reflection from surfaces. Therefore, angular dependence of polarized light in MWIR and LWIR can be predicted by Fresnel's equations.

Next this document examines specific cases of polarization signatures.

2.3.1 Mines and Unexploded Ordinance (UXO)

A degree of linear polarization (DoLP) of between 0 and 0.02 for CARC (chemical agent resistance coating) paint in reflectance [17] has been demonstrated. Sandy asphalt and CARC are not differentiable by polarization alone, but are with the addition of multi-band spectral filtering. Objects like cut wood (mulch), asphalt, plastics, metals, and non-rough dielectric surfaces show polarization signatures. To look for mines with polarization signatures, you must also combine different multispectral filters depending on the embedded soil type.

2.3.2 Naval and Marine Environment

In the naval environment, there is a particularly strong degree of polarization between the water and surface objects. Indeed, in emission, a DoLP of up to 5% has been

observed. Contrast enhancement of up to 30% can therefore be achieved in both the LWIR and MWIR, depending on the time of day [79].

Vertical polarization is predominately due to surface emission in the 8-12μm LWIR band and such polarized emission is governed by the Fresnel equations.

Horizontal polarization is predominately due to reflection in the 3-5μm MWIR band.

Consequently, due to the large degree of surface emissive polarized LWIR radiation, there is much more polarized electromagnetic energy in the LWIR than in the MWIR. In the MWIR, surface reflections tend to be horizontally polarized during daylight. Indeed, if sun glint occurs over 0.3% of the observed scene, the MWIR-LWIR spectrum tends to appear horizontally polarized. And, a clear sky will lead to more vertically polarized light than a cloudy sky [80]. Additionally, independent on time-of-day, there is more polarized energy given off in the LWIR than polarized reflection in the MWIR. In fact, the DoLP for the sea surface ranges between 7% and 30%. Ship targets have been shown to have a DoLP of up to 4.75%, much less than the emissive DoLP from the sea surface. MWIR polarized light originates mostly from sun-light reflection or moon-light reflection, so is highly correlated with time-of-day and weather [79].

2.3.3 Other Natural Objects

In studies of various foliage, specifically Laurel and Mullein leaves, polarization signatures were observed in direct proportion to waxy-surface content of those leaves. Laurel leaves demonstrate preferred p-polarization in self-emission due to their waxy surface. Mullein leaves, on the other hand, little polarization in either s or p orientations due to a relatively low amount of surface wax [81].

In moon-landing studies, surface dust (as found on rocks and spacecraft) caused de-polarization in the infrared and lead to increased surface brightness. In general, rough surface backscattering has twice the scattering as a diffuse surface, but was also measured to be much higher. Additionally, in an extraterrestrial environment, polarization has been used to determine cloud structure on Venus.

Throughout the UV to Near IR, for rough surfaces polarization has been shown to be an inverse function of surface brightness. This is attributed to the fact that powders have enhanced multiple scattering compared with geometrically rough surfaces, which then leads to de-polarization [82]. For this to be scaled to the MWIR and LWIR, the associated powder sizes and surface roughness would have to be scaled as well.

2.3.4 Other Man-Made Objects

Most man-made objects emit or reflect with somewhat linearly-polarized light. However, scattering from birefringent objects, highly absorbing objects, or metallic objects can lead to circularly polarized light.

In general, polarization from particle scattering is higher from dark surfaces at large scattering angles. This leads to positive polarization at large phase angles and negative polarization at small phase angles [37].

2.3.5 Non-Linearly-Polarized States

Since most man-made and non-made made objects radiate with either unpolarized, or slightly linearly-polarized light, for most cases it is not advantageous to be able to detect right-hand or left-hand circularly-polarized light.

2.3.6 DoLP Sensing Requirements

For the purpose of determining man-made from non-man-made objects, a degree-of-linear-polarization of less than 0.05 is required. Such a DoLP is achievable with polarizers with a cross-polarization extinction ratio of 20:1. However, ideally, we want to be able to distinguish between polarization signatures in the natural environment. Such signatures need a DoLP of at least 0.002. This gives a cross-polarization extinction ratio of 500:1. In practice, a metallic subwavelength grating structure can achieve a cross-polarization extinction of at least 100:1. With multiple-layered subwavelength gratings, it is possible to approach a cross-polarization extinction ratio of 500:1. However, such a requirement brings about additional concerns with detector

signal-to-noise as well as the thermal emissivity of the spectral/polarization filters. As such, while theoretically obtained results of cross-polarization extinction of >500:1 are reported in this thesis, experimental verification is required, as well as further exploration of signal-to-noise effects within the coupled detector/filter structure.

Chapter 3

Multispectral and Polarimetric Filter Technologies

This chapter presents a general overview of past, current, and proposed multispectral design concepts. The advantages and disadvantages for each multispectral design method is discussed with respect to the solid-state metallo-dielectric spectro-polarimetric filter designs proposed in this thesis.

3.1 Sensor Design Concepts

In Chapter 1 of this thesis, the need for a rugged, real-time, multispectral polarimetric sensor was demonstrated. In Chapter 2, the spectral regions of interest as well as the polarization-sensing requirements were outlined. Now, another question presents itself: *which technology suites itself best for the qualities outlined in Chapter 1 and the requirements outlined in Chapter 2?*

This Chapter explores some of the cost-benefit issues involved with the current multispectral polarimetric sensor technologies, including size, cost, development effort, and efficacy in meeting the imaging needs of the intended user.

3.1.1 Color-Wheel Filter Imagers

Multispectral filters, using color wheels, have the advantage of easy swap-in and swap-out of spectral filters. Additionally, such systems can incorporate anywhere from two to tens of possible passbands. To achieve polarization selectivity, these systems may also incorporate rotatable polarizers, or polarizers on a secondary filter wheel. The disadvantage of these systems is their size (color wheels take up additional space), the need for additional mechanical resources (to drive and sync the filter wheels with the imaging system), and their inability to take data at multiple wavelengths and polarization states at the same time. While it is possible, in theory, to achieve near real-time data acquisition at many wavelengths and polarization states [much as how man modern digital light processing (DLP) and liquid crystal display (LCD) technologies incorporate a color wheel for projection], these systems are not suitable for rugged environments and moving platforms.

3.1.2 Realtime Bore-Sighted Multi-Sensor

Bore-sighted multi-sensor systems–systems that share the same telephoto optics but then split optical path to separate sensors, usually with dichroics, are very effective at imaging one, two, or three separate spectra simultaneously. These systems are very good at collecting real-time data, and capturing image data simultaneously at several wavelengths and polarization states. However, due to the multiple sensor requirements, and the complexity of the optics and alignment required, such systems are very expensive to develop and manufacture and are usually rather large. Often, such systems are used for astronomical observation, or in high-end military imaging systems. The optical engineering required to make a highly-efficient bore-sighted system is expensive, and the effort required to maintain alignment for the optics and each sensor in such a system increases dramatically for each additional wavelength or polarization state.

3.1.3 Time-Sequenced Full-Frame Adaptive Filters

Time-sequenced full-frame adaptive filters can come in several forms. Either the spectral filter uses an adjustable cavity-length filter (in the form of MEMs controls or a piezoelectrically modulated Fabry-Perot cavity) or another form of electro-optic or mechano-optic mechanism for full imaging-frame passband control. For polarization, such systems usually incorporate liquid crystal cells for polarization selection, at least in the visible spectrum. Since liquid crystals, MEMs structures, piezoelectric transducers, and electro-optic crystals can usually be modulated very quickly, such systems are capable of video-rate multi-spectral and polarimetric imaging. Though, each captured image only contains information about an individual passband and polarization state. Such systems are better than color-wheel systems for use in observing fast-moving objects or with when used on fast-moving platforms (like on aircraft, on moving vehicles, or on mounted or dismounted infantry). However, such systems are not as good as bore-sighted systems for real-time data acquisition at multiple wavelengths for fast moving objects. Adaptive filters also have the benefit of greater real-time flexibility in the choice of wavebands and polarization states of interest than do either boresighted or color-wheel filtering technology.

3.1.4 Bayer-Type Spectral and Polarization Filters

Using Bayer-type filters, such as those found in most modern CMOS cameras (not all though, some have multiple layers of detectors, sensitive to different parts of the visible spectrum), is the method for creating multi-spectral and polarimetric filters recommended in this thesis. Bayer-type filters use separate color filters for each pixel in an imaging array. The work presented in this thesis and Don Kim's thesis [34] expands this idea to incorporating not only separate color filters for each pixel, but separate polarization filters for each pixel. Bayer-type filters can have anywhere from two different color filters, alternating filters between pixels, to as many color filters as there are pixels. In practice, two to four color filters are chosen. The concept behind the Bayer filter is to interpolate color data, since colors tend not to change rapidly

in most photographed scenes, but make sure that any rapid contrast changes are captured (by having lots of pixels). Indeed, this applies even better to the thermal infrared, where temperature variations across an imaged scene tend to be smooth. Additionally, natural scenes tend not to show a tremendous range of polarization-shifts from pixel to neighboring pixel. This concept becomes even more powerful as the spot size of the imaging optics becomes significantly larger than a pixel, and thereby the same 'spot' is imaged to several pixels, each with their own spectral and polarization filters.

The benefit of Bayer-type filters is that they allow for imaging optics of relatively simple design (since only one image is formed, and there is no need for intermediate filtering within the optical chain). They also allow for real-time image data acquisition of several wavelength and polarization states simultaneously. They can also be produced cheaply and can be mass-produced. The disadvantages of Bayer arrays is that they are limited to a predetermined set of spectral and polarization signatures. To change the spectral or polarization characteristics of such systems usually requires replacement of the entire Bayer-type filter array.

The ideal system would incorporate the arbitrary polarization-selective and frequency-selective properties of a an adaptive system with the real-time multispectral and polarimetric properties of a Bayer-type system. Such a system would have pixel-level control over spectral and polarization selectivity, and be capable of adapting to a scenario in real-time. Such a real-time adaptive Bayer-type system is beyond the scope of this thesis.

3.1.5 Lenslets Array Filters

The lenslet array concept is used widely in modern adaptive-optics systems. In this system, a lenslet array is used to form multiple images on a single detector array. For each lens, a separate polarization and spectral filter is chosen, so that the number of wavebands and polarization states that can be imaged at any one time depends only on the number of lenses and the size and number of detectors in a detector array.

Lenslet array systems are capable of real-time imaging at several polarization

states and spectral wavebands. However, because of the limited size of the detector array, for each additional waveband and polarization state, the number of available pixels to resolve the image decreases approximately as $1/n$. Therefore, the overall imaging system resolution drops dramatically with increased spectral and polarization selection requirements.

A benefit of this system, is that the optical setup is significantly simpler than that of bore-sighted system with an equal number of passbands and polarization filters. However, due the the decrease in resolution, a Bayer-type system has a significant advantage over the lenslet array method. Lateral resolution is not sacrificed for additional spectral or polarization discrimination.

3.2 Filtering Technologies

The filters designed in this thesis, to be compatible with the Bayer-array concept, incorporate both spectral and polarization filtering into one metallo-dielectric structure. These structures are capable of being easily fabricated in a mosaicked filter array.

These metallo-dielectric structures can be categorized as: 1) grating metallic filters with dielectric fill, 2) integrated polarizer / Fabry-Perot etalons, and 3) frequency selective perforated grid structures with embedded dielectrics.

1) **Metallo-Dielectric Grating Filters:**

   These filters include stacked polarizers with alternating grating periodicity and heights. These structures resemble photonic bandgap (PBG) structures currently being researched for use in optical communications. However, instead of hundreds or thousands of layers, the structures for infrared spectral and polarimetric filtering have one, two, or three stacked grating layers. Two forms of stripline structure are shown in Figure 3-1. In Figure 3-1 (a) is a diagram of the unit-cell of a four-layer stripline side-lobe suppression filter commonly used as a microwave filtering structure. In Figure 3-1 (b) a dual-stripline polarization and spectral filter is shown for reference.

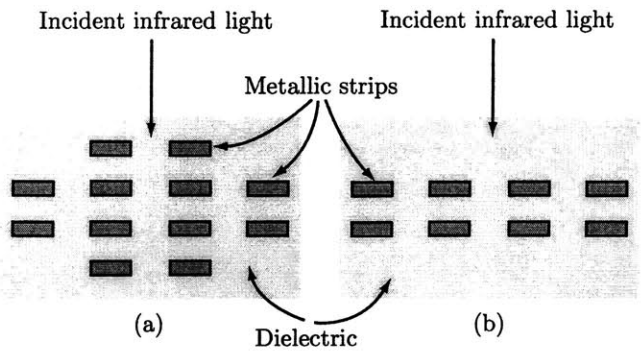

Figure 3-1: Diagrammatic side-on view of stripline filter designs, achieving both polarization and wavelength filtering by use of metallic strips.

2) **Integrated Polarizer / Fabry-Perot Etalons:**

These types of structures have the advantage of an increased TM vs. TE cross-polarization extinction ratio (as compared against separate polarizers and spectral filters of similar combined thickness) as well as enhanced frequency/wavelength selectivity. This wavelength selectivity can also be modified by changing the position of the polarizer within the etalon (and by placing it in different layers of the dielectric quarter-wave stack) or by embedding multiple polarizers or chirped polarizers within the etalon. Fabry-Perot interferometers are well-known for their ability to select narrow wavelength bands for transmittance. Fabry-Perot etalons are also easily tunable by varying their cavity length. It is also possible to create a cavity with a sandwiched layer of metallic polarizer. Furthermore, it may be possible to modulate the cavity length so that we may scan a range of wavelengths-of-interest for an imaging system.

It has been demonstrated that long-duty-cycle polarizers within the Fabry-Perot cavity polarize light to a higher degree than do similar polarizers located outside of the cavity. See Figure 3-2 for a diagram showing the Fabry-Perot / polarizer described above.

In the initial stages of this project, numerical simulations were performed on periodic metallic grid structures imbedded within a Fabry-Perot etalon to determine the spectral and polarization filtering efficacy of such coherently-coupled

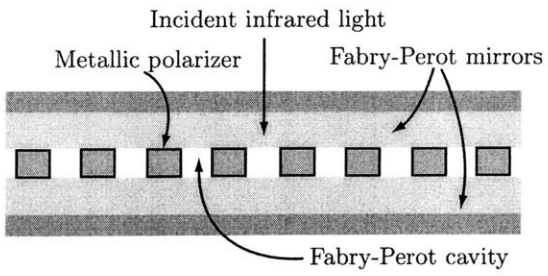

Figure 3-2: Another possibility for a frequency-selective, polarization-dependent filter is a Fabry-Perot spectral filter with an internal polarizer. Such a device might possibly be tuneable with the aid of piezoelectric spacers.

structures (compared to the filtering efficacy of un-coupled, spatially separated Fabry-Perot etalon and wire-grid structures). An increased extinction ratio between TM and TE polarizations was observed around the design wavelength for coherently-coupled structure.

3) **Frequency Selective Perforated Grid Structures with Embedded Dielectrics:**

These structures consist of one or more perforated metallic films deposited within or outside of layers of dielectric. The use of perforated metallic grids, embedded within dielectric layers, results in an increased wavelength selectivity and polarization selectivity while minimizing the total depth of the system. Only one to two layers are needed in such structures as compared to the tens of layers required for equivalent dielectric stacks. Similar structures are used for frequency and polarization selection in RADAR filters. The dielectric layers of the proposed structures are made of either dielectric gratings or uniform dielectric material. Shown in Figure 3-3 are two top-view examples of perforated metallic grid structures. Shown in Figure 3-3 (a) is a diagram of a slotted grid structure that both exhibits polarization and spectral selectivity. The structure represented in Figure 3-3 (b) exhibits spectral selectivity with minimum polarization selectivity.

By combining the refractive properties of dielectric materials with the reflective and absorptive properties of metals, one can achieve better polarization and

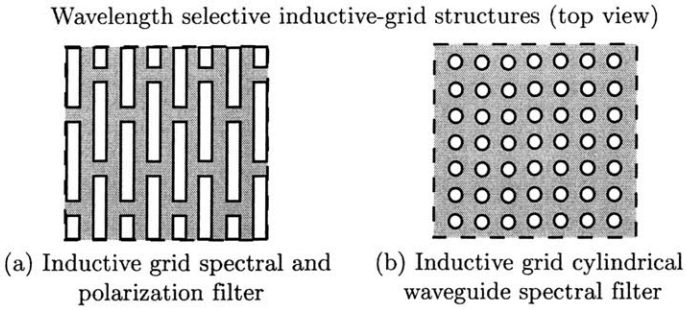

Figure 3-3: Top-down view of two wavelength-selective periodic structures: (a) achieves both polarization and wavelength selectivity (b) achieves only wavelength selectivity

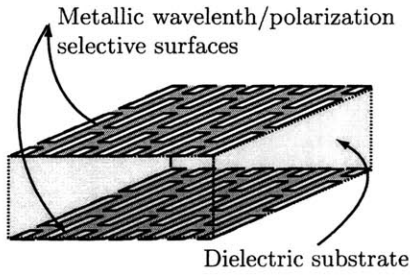

Figure 3-4: By sandwiching a dielectric layer between two wavelength and polarization selective structures, greater control of wavelength and polarization selectivity may be achieved.

wavelength selectivity than with separate metallic or dielectric filters while still using current manufacturing technology. It is this combination of materials, used in novel ways, that produces the most encouraging results.

There are other classes of structures used in RADAR beam-forming and filtering that have potential as filters in the infrared. With the addition of high-index dielectrics, these structures can be designed in a way that further increases their efficacy and decreases their loss. Such a structure, utilizing two two-dimensional arrays of inductive slit metallic filters separated by a narrow sheet of dielectric material is drawn in Figure 3-4. In Figure 3-1 a filter with four layers of metallic strips, which is a natural extension from two sheets of polarizers, is shown.

3.3 Summary

Usually, the best-engineered system uses the least complex design to achieve the most robust results. In the case of the proposed Bayer-filter-type topology, with individually designed and bulk-manufactured macro-pixel arrays, the simplest design to achieve both spectral and polarimetric filtering should be chosen. For the concept of coherently-coupled metallo-dielectric structures, single and double-layer structures are chosen due to their manufacturability and their capacity to perform spectral and polarization filtering within the criteria set forth in Chapter 2. Additionally, the simplest type of two-dimensional frequency-selective-surface, a slotted grid, is analyzed in both single and double-layer configurations as an infrared multispectral-polarimetric filter in the following Chapter.

Chapter 4

Metallo-Dielectric Spectro-Polarimetric Filter Design

Integrated metallo-dielectric structures promise the ability to perform spectral and polarimetric filtering without the need for multiple stacked layers of independently-designed spectral and polarization filters. By eliminating the need for separate polarization and spectral filtering elements, a combined spectro-polarimetric filtering structure enables the construction of completely solid-state filters, greatly reducing post fabrication integration and alignment issues, especially when such structures can be fabricated directly on top of, or within, current MWIR and LWIR detector arrays.

4.1 Filter Design Considerations

The single or multi-layer metallo-dielectric filters discussed in this chapter, are designed with the purpose of overcoming issues that plagued previous multispectral polarimetric filter designs. These include: eliminating high-order diffractive effects, environmental instability of large dielectric stacks, and detector-filter compatibility.

4.1.1 Diffraction Effects Due To Filter-Detector Offset

When fabricating filters, both spectral and polarimetric, diffraction effects can play a significant role in decreasing the signal-to-noise ratio between neighboring pixels. In previous designs [34], the spectral filter, polarization filter, and detector were all designed and fabricated as separate elements in an infrared imaging system. The advantage of such a design methodology, is that individual filter or sensor layers can be readily retrofitted as the application changes. Also, this decreases the design sensitivity, in that, as long as elements are spaced far enough apart, each filter or sensor layer can be simulated and designed as un-coupled structures. As long as the coherence length of light being detected, such as from a thermal black-body source such as the sun, with coherence length on the order of l_c=0.6μm, is shorter than the distance between optical elements, each element can be treated as an independent filtering entity.

However, the spatial coherence of thermal sources can be quite large, and therefore diffractive effects from the limited aperture sizes of individual spectral filters or the wavelength-scale sizes of polarizer elements can also be substantial. Indeed, in this thesis, designing polarization filters to specifically utilize such anomalies to aid in the design of the spectral filtering curve is explored. The Woods-Rayleigh anomalies, as they have come to be called, will be described in a subsequent section.

Additionally, since light enters into a filtering structure from a range of angles and not in a collimated beam, a necessary consequence of most multi-lens imaging systems, the likelihood of cross-talk between pixels is increased. The more layers a filter contains, and the larger the space from filter to detector, the more light that is allowed to escape to neighboring pixels and thereby decrease image contrast.

To ensure that cross talk does not become an issue, complex baffle designs can be implemented, or each filter element can be thinned and abutted to ensure the minimum possible optical path between filter layers and detector.

To simplify filter design, filters can be fabricated directly on top of one another, still acting as un-coupled spectral and polarization filters. This complicates the fab-

rication of such structures dramatically due to alignment issues as well as the need to create tall dielectric stacks (for spectral filtering) which often have weak adherence to the multi-layer metallic grating structures used as polarizers.

In this document, the design of spectral and polarimetric filters is taken an additional step forward. Instead of thinking of the spectral and polarization elements as separate, they are thought of as coupled devices whose spectral filtering characteristics can be mutually beneficial. With coupled devices, where a single filter layer performs both spectral and polarization filtering, we can eliminate our concerns over crosstalk between pixels. We can also belay concerns over ruggedness, adherence, and material compatibility between spectral filtering and polarization filtering layers since the combined structure is embedded instead of 'stacked.'

4.1.2 Dielectric Stack-Only Filters

Dielectric-only stacked filters (dichroic filters) are extremely common for use in spectral filtering. Like any spectral filtering technology, they have advantages and disadvantages over competing technologies. The transmission or reflection spectra for dichroic filters can be designed within extremely sharp bandwidth and band-peak tolerances. They can have extremely high transmission or low transmission over nearly arbitrary design wavelength intervals. The theory behind designing dichroic filters is extremely well developed, and handbooks of filter designs are available for the optical engineer to create most any filter of interest. However, while stacked dielectric films can give the designer a lot of flexibility in their spectral characteristics, a rather large price is paid: the price of space.

Dielectric stack filters, in order to achieve almost arbitrary bandwidth and center-wavelength control, except for special cases, usually need to be made with many layers. Each layer is often on the order of a quarter to a half-wavelength of the light to be filtered. And many layers of dielectric, each with its own refractive index, and its own material compatibility to the adjacent layers, must be stacked one on top of the other to form the desired spectral filter. While peel-off, which happens when layers do not stick together with enough force to overcome friction, outgassing, or

expansion or shrinkage, can be controlled with large-area dielectric films stacks (such as those found on dichroic mirrors found in most optics laboratories), it is difficult to control peel-off when stacks are particularly tall with respect to their width.

When dielectric stack filters are made small, in a transverse sense, they do not tend to be as stable as wide filters, with lots of surface area to adhere to the previous and next layers. For many filters, especially in the visible, NIR, and MWIR wavelengths, this does not present as much an issue as it does for LWIR or FIR wavelengths. This because dichroic filters in the visible, NIR, and MWIR do not require stacks of as prodigious a height as is required in the LWIR. Additionally, in the visible and NIR, there are more materials that are optically and mechanically compatible to work with and design around.

To get around the fabrication and environmental issues that come with dielectric stack filters, this thesis proposes using metallic structures to amplify the spectra filtering ability of an embedded dielectric layer. Or, thought of another way, this thesis proposes using dielectric fill to improve the spectral filtering of periodic metallic TM-waveguide structures.

4.1.3 Metallic Polarization Filters

Metallic polarization filters are very common in MWIR or LWIR polarization filtering. Whereas in the visible spectra, where film with herapathite crystals, plastic with iodine, or liquid crystals can readily perform polarization filtering, in the IR, our choices are quite limited. For thin polarizers, as opposed to beam-splitter-type polarizers or dichroic polarizers, in the IR we usually use absorptive-type wire-grid polarizers. These can come in the form of Aluminum, Gold, or hybrid material wires on an IR-transparent substrate such as ZnSe, CaF_2, or Ge. The wire spacing is usually on the order of 0.25μm. The closer the grating pitch of the wire-grid polarizer comes to the filtering wavelengths, the less efficient the polarization structure becomes. Indeed, the closer the grating pitch is to the filtered wavelengths, the more non-flat the polarizer spectral transmittance curve becomes for TM light, and indeed, as the design wavelength approaches the grating pitch, substantial spectral anomalies

result.

Determination of Stoke's Parameters

The purpose of a polarizer, or any polarization-selective structure, is to enable differentiation between polarization states. In the cases of the metallo-dielectric spectro-polarimetric filters studied in this thesis, each filter is designed to transmit the TM (or p-polarized) component of an incident optical field. As discussed in the first chapter, one of the goals of this filter is to be able to distinguish man-made from natural objects by looking at their spectral and polarization signatures in the infrared. It was also discussed how man-made objects are distinguishable from natural objects by their significant linear polarization components (whether reflected by the sun or emitted as its own black-body source). Very few objects, man-made or natural, reflect or emit light in a way that results in circular polarization. Especially in real-world scenarios, such as search and rescue missions or in object detection and discrimination, it is unlikely to encounter objects that emit or reflect large amounts of circularly-polarized light. Therefore, when determining the polarization state of light emitted or reflected from a scene, we will ignore circular polarization, and only concern ourselves with linear polarization. Specifically, of interest to this thesis, is the ability to distinguish orthogonal states of linear polarization. In other words, we need to be able to determine three of the four Stoke's parameters. With the Bayer-type filter array, this means that we want to detect at least three linear polarization states with three separate filters. By using three linear polarization filters, the first two orthogonal, and the last one at either 45° or -45° to the axis of either polarizer, we will be able to determine the degree of linear polarization (DoLP) and the angle the polarization vector makes with the detector in order to infer the orientation and type of object under observation.

4.2 Single-Layer Metallo-Dielectric Filter

Single-layer metallic gratings of one dimension with dielectric fill present the simplest design for a multispectral, polarimetric filter. The design of such structures is discussed in this section. The manufacturing benefit of one-layer metallo-dielectric gratings is that they have relatively low transmission loss due to absorption, and can be made much thinner than filters of separate dielectric stacks and polarizer that have similar bandwidth and transmission efficiency.

4.2.1 Fabry-Perot Effects of Single Layer Wire Grids

Metallic two-walled slab waveguides (the same as a parallel plate transmission line) can be used for the spectral filtering of electromagnetic signals. Indeed, a parallel plate transmission line, that is long enough, behaves very much like a Fabry-Perot cavity.

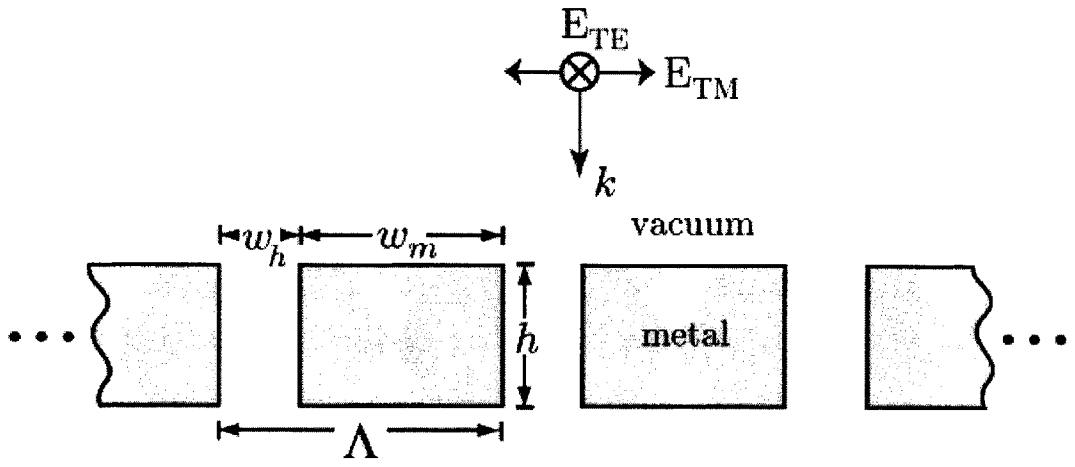

Figure 4-1: Single-layer rectangular-cross-section metallic grating structure. Light is nominally incident from the top. The polarization vector for TM light is in the same plane as the grating vector. w_m is the width of each metal element in the grating. w_h is the width of each free-space region of the grating. h is the height of each metal element of the grating. Λ is the grating pitch.

Independent of the spacing between parallel plates in a parallel plate waveguide, the fundamental TM_0 mode is able to propagate in the waveguide. In our case, we will be dealing with subwavelength gratings, so only the TM_0 mode can propogate.

All TE light is rejected from passing through the structure by means of absorption or reflection. Indeed, layers of dielectric slabs can be analyzed using the mathematics of the lumped element theory of transmission lines. A parallel plate waveguide can conversely be viewed as a dielectric of some thickness having a certain electromagnetic impedance. This equivalence holds ever more true, the longer the waveguide becomes with respect to the size of it's opening. In other words, the higher the aspect ratio of waveguide length to waveguide opening, the closer the guide becomes to looking like a Fabry-Perot cavity.

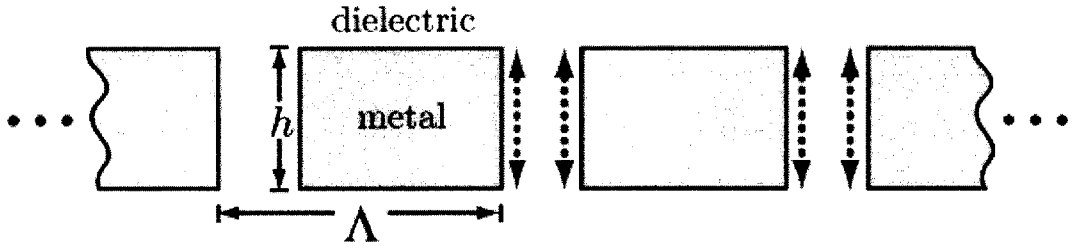

Figure 4-2: This diagram defines the vertical resonances in a single-layer metal grating structure. The vertical resonances exist primarily between the top and bottom surface of the grating–where light entering the grating from the top reflects off of the bottom and top interfaces of each 'parallel-plate' transmission line element. Fringing fields are not depicted; only the nominal propagation direction of the vertical resonances (drawn as red dotted lines with arrows) are shown.

While a single parallel-plate transmission line will create a Fabry-Perot-like effect, a large number of such transmission lines, all transmitting in parallel, and coupled through horizontal grid resonances (as will be discussed in the next section), will produce a very high transmission response at the resonant wavelengths of the Fabry-Perot-like cavity.

Such transmission peaks, for a structure that exhibits a large enough aspect ratio (that is $w_h >> h$, should be near the expected Fabry-Perot etalon peaks of $\lambda = 2h/m$, where m is a positive integer. Indeed, this resonant effect, which can exist for rectangular cross-section metal gratings in vacuum, can also exist within the same metallic structures embedded within a dielectric. Embedding the metal in dielectric, as will be shown, greatly magnifies the spectral filtering ability of such a structure.

It is important to note that the Fabry-Perot-like vertical resonances (as opposed to the horizontal grating resonances), are not exactly the same as the Fabry-Perot

resonances that result for a dielectric slab structure. These resonances result from the impedance change observed by the electromagnetic wave as it passes through the structure as well as diffractive effects from the finite-width aperture and edges of the structure. Indeed, since the effective parallel-plate transmission line is not infinite, one would expect fringing fields at both ends of the waveguide, which would in turn make the waveguide appear to be slightly longer in terms of the height, h, than a Fabry-Perot cavity with the same longitudinal dimensions. So, in fact, the peaks should appear close to the expected Fabry Perot peaks of $\lambda = 2h/m$, but with a small effective height increase due to fringing fields, that we might call ϵ. Thus, we would expect the actual vertical resonance peaks to appear at some $\lambda_{\text{peaks}} = 2(h+\epsilon)/m$, where h is the measured height of the metal in the direction parallel to the propagation vector, k, of incoming light, and m is a positive integer.

To demonstrate the Fabry-Perot-like effect of vertical-resonances in a rectangular cross-section metallic grating, I have included the Figures 4-4 and 4-3. Both of these Figures result from the FDTD simulation of the rectangular metallic grating structure sketched in Figure 4-1.

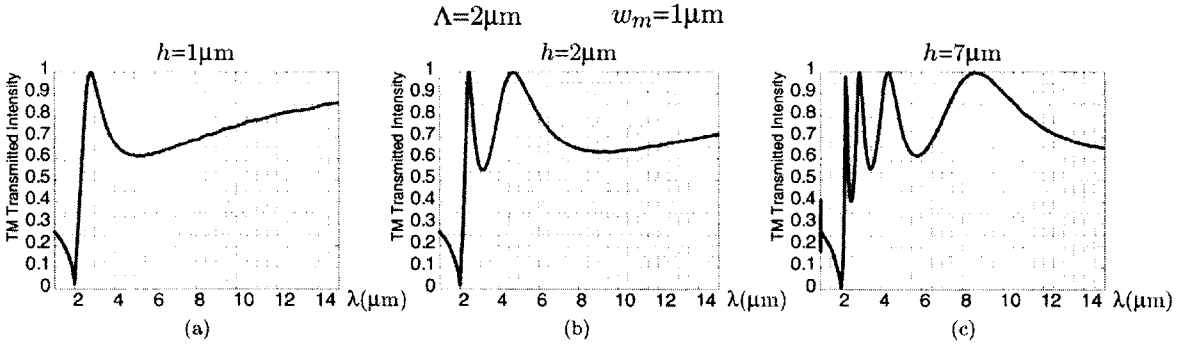

Figure 4-3: Simulated TM intensity transmission curves for single-layer metal gratings of constant pitch and metal width, and varying height. **(a)** Λ=2μm, w_m=1μm, h=1μm, **(b)** Λ=2μm, w_m=1μm, h=2μm,**(c)** Λ=2μm, w_m=1μm, h=7μm

To create Figure 4-3, the metal width and grating pitch of the single layer grating structure have been kept constant at w_m=1μm and Λ=2μm respectively. The transmission curve was generated using a simulated broadband TM source. In Figure 4-3 (a), (b), and (c), there are nulls at λ=2μm. This will be explained in the subse-

quent section discussing horizontal resonances. For a classical Fabry-Perot cavity of cavity-length, h_{FP}, one would expect peaks at $\lambda_{\mathrm{FP}} = 2h_{\mathrm{FP}}/m$, where m is a positive integer.

For the case of the simulated structure, where three heights were simulated: h=1μm, h=2μm, and h=7μm, the Fabry-Perot equivalent would indicate the existence of a peak near $\lambda_{\mathrm{FP}} = 2\mu$m for h=1μm, $\lambda_{\mathrm{FP}} = [4, 2]\mu$m for h=2μm, and $\lambda_{\mathrm{FP}} = [14, 7, 4.67, 3.5, 2.8, 2.33, 2]\mu$m for h=7μm. This only accounts for the resonances above the limiting horizontal grating resonance at λ=2μm. In figure 4-3, once can see these resonances, but due to the fringing fields at the top and bottom surfaces of these structures, at slightly longer wavelengths. However, due to the anomaly at λ=2μm, which will be discussed later, not all the resonances near that null appear. The larger the opening, the more red-shift that occurs for longer wavelengths. As shown, while the Fabry-Perot model can be explanative for the peak locations for widely-spaced metals, it is not accurate enough for the purpose of filter design.

The weakness of the Fabry-Perot model is that it does not account for fringing fields. However, if the fringing fields are minimized, by increasing the aspect ratio of the grating (by increasing the aspect ratio of h/w_h), or–as will be shown later– by adding a dielectric, the Fabry-Perot model can become accurate enough for the purpose of filter design.

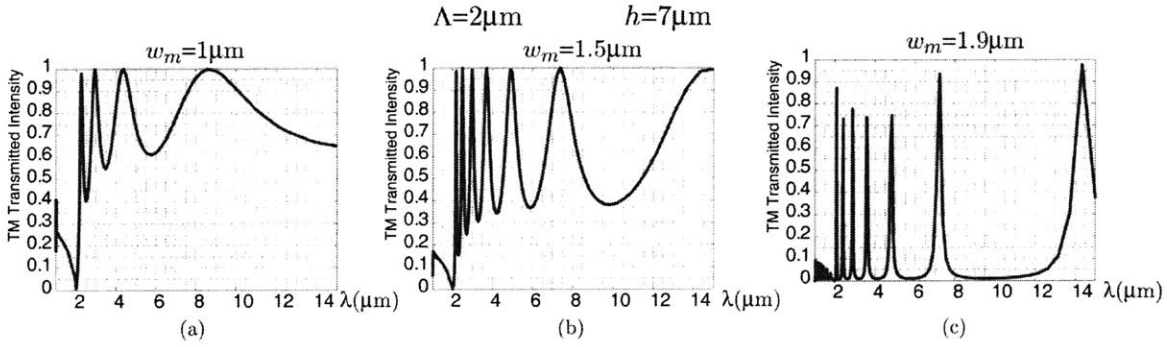

Figure 4-4: Simulated TM intensity transmission curves for single-layer metal gratings of constant pitch and height, and varying metal width. **(a)** Λ=2μm, w_m=1μm, h=7μm, **(b)** Λ=2μm, w_m=1.5μm, h=7μm,**(c)** Λ=2μm, w_m=1.9μm, h=7μm

Indeed, in Figure 4-4, such correlation is shown. In Figure 4-4, the grating pitch

and metal height are kept constant, at Λ=2μm and h=7μm, respectively. From Figure 4-4 (a) to (b) to (c), the metal width is changed from 1μm to 1.5μm to 1.9μm. In other words, the aspect ratio of the vacuum between the metals changes from 7:1 to 14:1 to 70:1. While an aspect ratio of 70:1 would be difficult to fabricate in the optical regime, it demonstrates the accuracy of the Fabry-Perot approximation in the limit as the aspect ratio of the grating becomes very large. Indeed, later in this chapter it will be shown how to decrease the aspect ratio with the inclusion of dielectric fill.

Figure 4-4 (c), with a metal width of w_m=1.9μm, a grating pitch of λ=2μm, and therefore a free-space aperture width of w_h =0.1μm, demonstrates how the Fabry-Perot model can accurately determine the peak locations for such a high-aspect ratio vertical resonant structure. That is, the Fabry-Perot transmission peaks, which were calculated to be at $\lambda_{\mathrm{FP}} = [14, 7, 4.67, 3.5, 2.8, 2.33, 2]\mu$m are all present with minimal red-shift.

4.2.2 Woods-Rayleigh Anomalies of Single-Layer Wire Grids

Besides the vertical resonance internal to the metal grating structure, another resonant effect also plays a significant role in determining the transmission characteristics of a metallic grating structure. The horizontal resonances, due largely to the constructive or destructive interference of light diffracted from the periodic top or bottom surface of the grating, have a significant effect on grating transmission, especially near what are termed the 'Rayleigh anomalies.'

Rayleigh anomalies appear when a diffracted order, either above or below the grating disappear. This occurs when

$$k_{xq} = k_{x0} + \frac{2\pi q}{\Lambda}, \quad q \in [0, \pm 1, \pm 2, \pm 3, ...] \tag{4.1}$$

where k_{x0} is the component of the incident propagation vector projected along the axis of the grating (x-axis), q is an integer describing the order of diffracted light (corresponding to an integer multiple of grating periods), Λ is the grating pitch, and k_{xq} is therefore the resulting propagation vector, projected along the axis of the

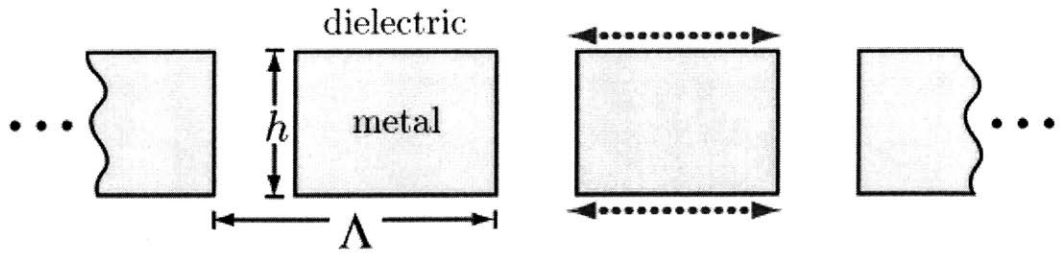

Figure 4-5: This diagram defines the horizontal resonances in a single-layer metal grating structure. The horizontal resonances exist primarily on the top and bottom surface of the grating–where light entering the grating from the the top or exiting the grating at the bottom diffracts into higher order modes that propagate along or near the grating surface. The nominal direction of the horizontal resonances is indicated by the dotted red line.

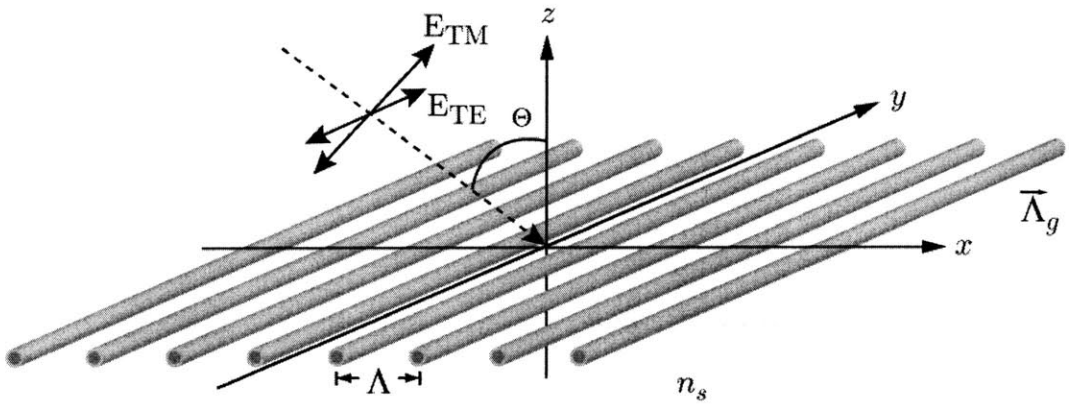

Figure 4-6: Grating definition. For a grating structure, TM light is defined as having its electric field completely within the plane of incidence. The TE component of an incident beam has electric field directed normal to the plane of incidence. When θ=0, TM is defined as having an electric-field vector pointing in the same direction as and parallel to the grating vector, $\overline{\Lambda}_g$. The grating pitch is Λ, the smallest repeating unit of grating symmetry.

grating, of the transmitted beam of order, q.

This in turn can be written in the form of,

$$n_s \sin\theta_q = n_i \sin\theta_i + \frac{\lambda q}{\Lambda}, \quad q \in [0, \pm 1, \pm 2, \pm 3, ...] \tag{4.2}$$

where n_s is the index of refraction of the grating substrate, n_i is the index of refraction for the incident dielectric layer, θ_q is the angle of the transmitted beam of order q, and θ_i is that angle of the incident beam with respect to the normal of the grating, and λ is the free-space wavelength of incident light.

For light at normal incidence, $\theta_i = 0$, this gives us

$$n_s \sin\theta_q = \frac{\lambda q}{\Lambda}, \quad q \in [0, \pm 1, \pm 2, \pm 3, ...] \tag{4.3}$$

and allows us to solve for the transmitted angle of order q,

$$\theta_q = \arcsin\left(\frac{\lambda q}{\Lambda n_s}\right), \quad q \in [0, \pm 1, \pm 2, \pm 3, ...] \tag{4.4}$$

For θ_q to be real for $q \geq 1$, then $|\lambda q/\Lambda n_s| < 1$. Therefore, as the argument of the arcsin approaches 1 or -1 and then exceeds 1 or -1 for a given q and Λ, as λ increases or decreases, the corresponding order of light, q disappears for that wavelength, λ. And, the total transmittance at that particular λ goes to zero. Simply stated, Rayleigh anomalies occur when

$$\lambda = \frac{n_s \Lambda}{q}, \quad q \in [0, \pm 1, \pm 2, \pm 3, ...] \tag{4.5}$$

In Figures 4-3 and 4-4, the Rayleigh anomaly presents itself at λ=2μm since Λ=2μm and grating is simulated to be free-floating in vacuum.

Rayleigh anomalies are omnipresent in simple un-chirped grating structures, as long as the grating pitch multiplied by the substrate index of refraction (this multiplied quantity I will refer to as the 'effective grating pitch') is equal to or greater than the wavelength range of interest.

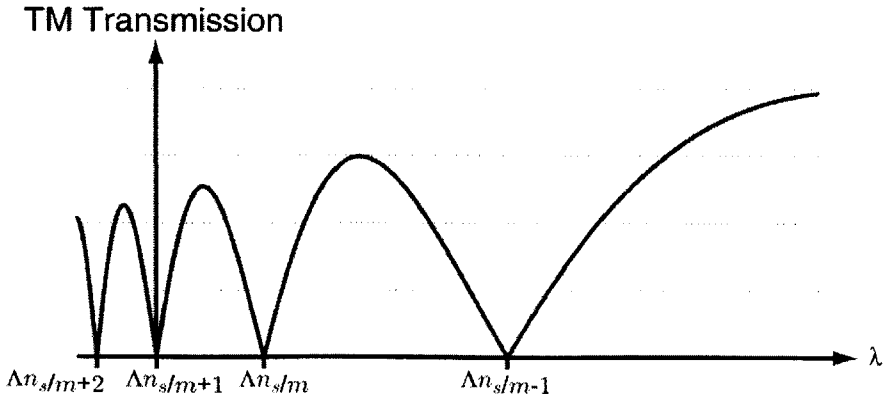

Figure 4-7: Demonstrative diagram of the Rayleigh anomaly. When $\lambda = \Lambda n_s/q$ for $q \in [0, \pm 1, \pm 2, \pm 3, ...]$, the TM transmitted intensity goes to 0. The diagram above shows how this might occur about some arbitrary $q = m$.

Many filter designers, who must fabricate metal-grating polarizers for use in infrared filtering applications, try to minimize the effective grating pitch so that Rayleigh anomalies do not effect in the wavebands they are trying to filter. In general, the smaller the effective grating pitch, the flatter the transmission curve for TM light. Designing a polarizer in this way makes for an excellent system component when tight integration of the spectral and polarization filtering components is not required. However, in this thesis, tight integration is the goal.

Because the Rayleigh anomaly does not depend on the height, h, of the grating, nor does it depend directly on the metal width, w_m, as long as $w_m < \Lambda$, and because the vertical resonances do not rely, in first order, on Λ, this allows us to design a single-layer metallic-grating spectro-polarimetric filter. The methodology follows:

In Figure 4-4 (c), we saw several Fabry-Perot-like peaks. There are resonant peaks at approximately, $\lambda_{\text{FP}} = [14, 7, 4.67, 3.5, 2.8, 2.33, 2]\mu$m. Let's now say that we'd like to create an MWIR filter that only transmits light for the 4.67μm peak. The problem is that the 3.5μm peak will also be transmitted for the same choice of metal width w_m and metal height h. However, we can greatly reduce the intensity of light transmitted due to the 3.5μm peak by making the effective grating pitch 3.5μm, effectively killing that peak. In other words, by appropriately choosing w_m, h, and Λ we can design single-layer metallic-grating filters that can have nearly highly adjustable bandwidth and peak transmittance location in addition to rejecting higher-frequency (lower wavelength) transmitted lobes.

4.2.3 Dielectric Embedding vs. Non-Embedding and Substrate Properties

As demonstrated in the previous section, sharp, narrow-bandwidth peaks can be achieved by making $\Lambda - w_m$ very small. However, this proves impractical very quickly due to the limitations of current semiconductor manufacture technology. Creating wide metals with very narrow gaps is quite difficult, especially for the case of a height to width ratio of 70:1. It is also impractical to have a wire grating suspended in

vacuum without a dielectric substrate.

Embedding the metal grating in dielectric presents several competing factors which we must take into consideration when designing a spectro-polarimetric filter. By embedding the metal grating in dielectric, we push the first zero of the Rayleigh anomaly from Λ to Λn_s. This can allow the design some freedom in choosing dielectric and grating pitch. Additionally, by filling the otherwise open space between the metals within the grating with a dielectric, one effectively increases the optical path by a multiplicative distance n_f as well as an effective width-increase of the non-metal area, m_h. Increasing the effective m_h increases the Fabry-Perot-type resonance bandpass FWHM. And, additional Fabry-Perot-type peaks show up since the effective metal height has changed from h in vacuum to hn_f. By adding dielectric, we are able to effectively increase the height of the Fabry-Perot type cavity.

Most importantly, however, is that by including a dielectric fill, the design does incorporate an actual Fabry-Perot cavity that narrows the bandpass transmissions of the metal-only Fabry-Perot-like vertical resonances. In fact, by including dielectric fill, spectro-polarimetric filters can be designed which are both feasible in a manufacturing standpoint, and are more efficient than previous filters designed using separate dielectric stack filters and polarization filters in performing spectro-polarimetric filtering for their given height.

4.2.4 Single Layer Metallic Grating Filter with Dielectric Fill Design

Using the principles stated in the previous section, a single-layer metallic grating spectro-polarimetric filter with dielectric fill was designed and simulated. In Figure 4-8, a diagram of a proposed metallic-grating rectangular-cross-section dielectric-filled filter is shown.

By varying the width of the grating metal, w_m, to control the width of the pass-band, and by varying the grating pitch, Λ, to adjust the location of the Rayleigh anomaly, and by varying h to control the peak location of the vertical resonances, a

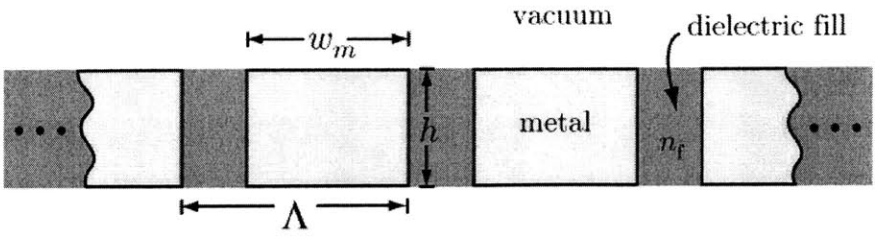

Figure 4-8: Single-layer metallic grating filter with dielectric fill.

polarization-dependent spectral filter design was developed.

To simulate the structure, finite-difference time-domain FDTD numerical calculations were performed. Both perfect-electric-conductor (PEC: $\sigma = \infty$) and modeled Aluminum conductors were used (Al: n =6.43, σ=3.78×10^{7}S m$^-$1) [83] in simulating the structure. The fill material was chosen to be amorphous silicon (Si-a) with an index of refraction, n_f=3.43. For a filter with peak transmittance at λ=4μm and a FWHM of approximately 0.5μm spectral bandwidth, it was determined that h=0.56μm, which with the dielectric fill is approximately a $\lambda/2$ Fabry-Perot cavity. Additionally, Λ=0.72μm, and w_m=0.5μm. This gives a physical aspect ratio for height to aperture of approximately 2.5:1, much more feasible than without the dielectric fill.

Figure 4-9 shows the 4μm peak transmittance filter design using a perfect-electric conductor metal for both TE and TM light. Figure 4-10 shows the 4μm peak transmittance filter design using the modeled Aluminum as the conductor of the metal grating. And Figure 4-11 overlays the TM transmission spectra for both the Aluminum and PEC modeled conductors. Note that while the peaks remain in the same position, there is a 30% drop in transmitted intensity for TM light from PEC to modeled aluminum. For both the PEC case and the modeled Aluminum case, the extinction ratio between TM and TE light was calculated to be greater than 1:2×10^6 for the entire 2μm-15μm spectrum.

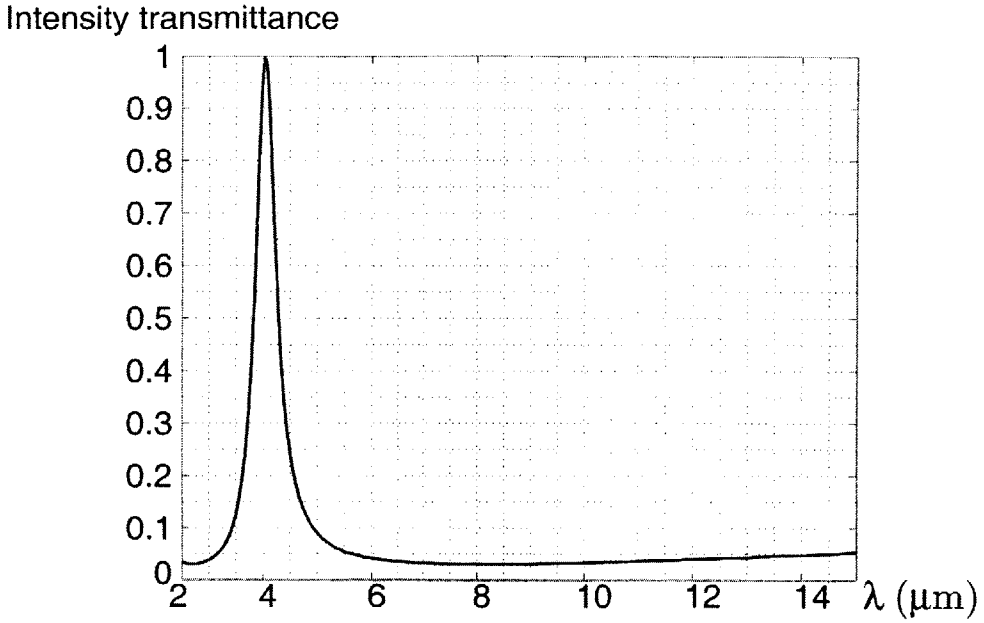

Figure 4-9: Calculated TM transmittance (blue solid line - top) and TE transmittance (orange solid line - bottom) for a PEC-modeled metallic grating with dielectric fill. Simulation parameters: Λ=0.72μm, $n_f = 3.43$, $h = 0.56\mu$m, w_m=0.5μm.

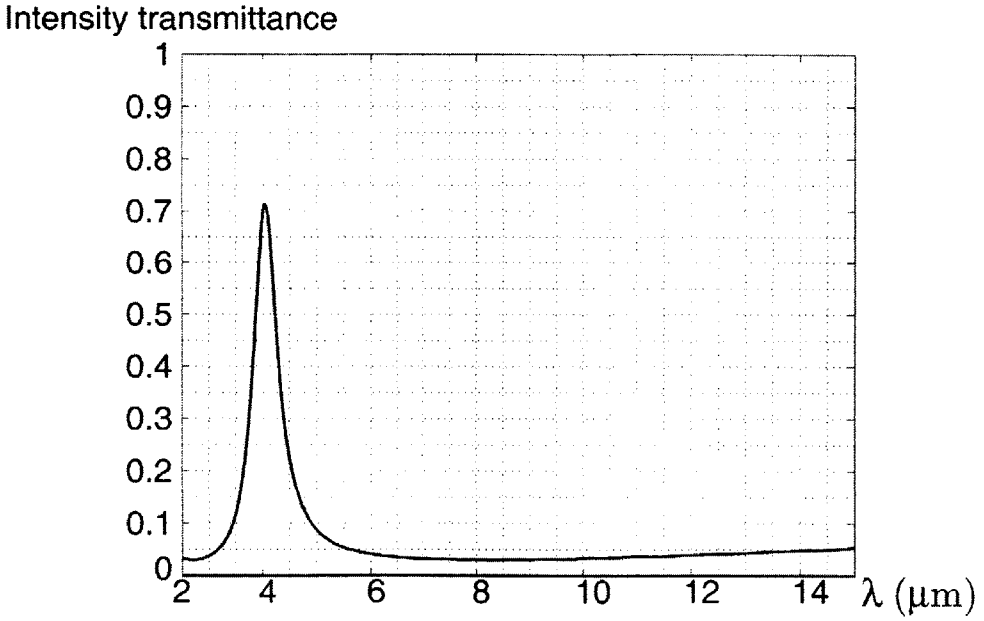

Figure 4-10: Calculated TM transmittance (blue solid line - top) and TE transmittance (red solid line - bottom) for an Al ($n = 6.43$, $\sigma = 3.78 \times 10^7$) modeled metallic grating with dielectric fill. Simulated parameters: Λ=0.72μm, $n_f = 3.43$, $h = 0.56\mu$m, w_m=0.5μm.

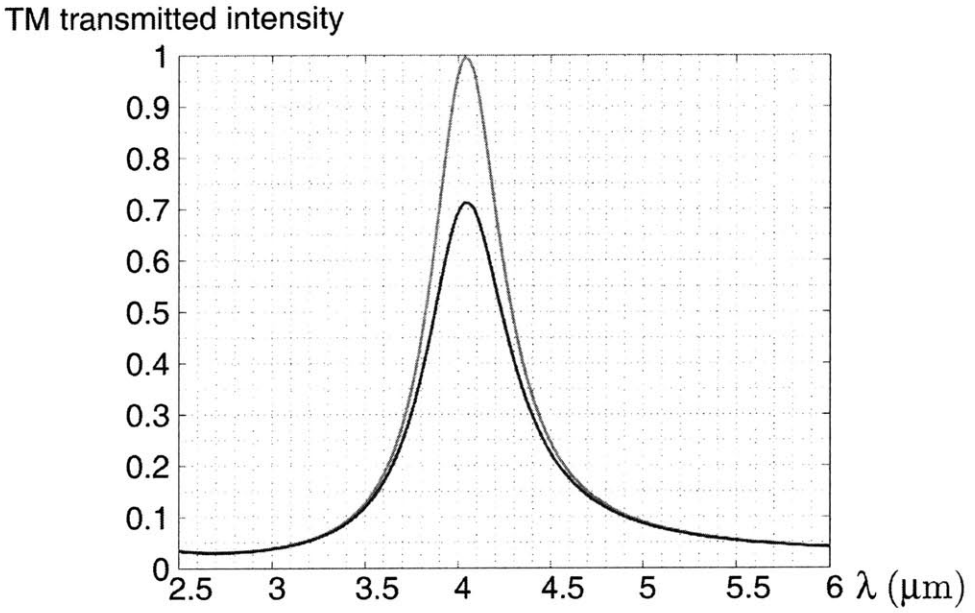

Figure 4-11: Calculated TM transmitted intensity for the single layer metallic grating filter modeled as both a PEC (orange solid line - top) and an Aluminum (blue solid line - bottom) conductor.

Single-Layer Multispectral Filter Design

In order to compare the simulated design of a single-layer metallic grating filter with dielectric fill with previous non-integrated filters designed in the author's research group [5], three filters were designed and simulated using the same criteria as set forth in Kim's thesis [34]. That is, three spectral filters, with approximately FWHM bandwidths of 0.5μm and peak transmittance at λ=3.5μm, λ=4μm, and λ=4.5μm were designed.

Using the same methodology used to create the first filter, three filters were created according to the design criteria. For each of these filters, the grating pitch, Λ=0.72μm was kept the same. Additionally, the metal width, w_m=0.5μm was kept constant. The only variable that changed was the metal height, h. For the 3.5μm filter, the height was calculated to be h=0.5μm. For the 4μm filter, the height was calculated to be h=0.56μm. And, finally, for the 4.5μm filter, the height was calculated to be h=0.62μm. A 0.06μm height difference, roughly translates to 0.5μm peak shift in the MWIR.

For dielectric stack filters, as designed by Kim [5], the optimal heights for the Ge:SiO:Ge filters were 1.39μm, 1.58μm, and 1.78μm for the λ_c =3.5μm filter, the λ_c =4.0μm filter, and the λ_c =4.5μm filter, respectively. While maintaining a similar FWHM bandwidth, the combined spectro-polarimetric design described previously was only 0.5μm, 0.56μm, and 0.62μm tall respectively. This is a height savings of between 0.89μm and 1.16μm on just the spectral filter alone. In Kim's original design, the polarization and spectral filtering components were separate. So this space-savings is in addition to the space saved from eliminating the separate polarizer, and polarizer substrate.

However, even though there is a space savings, both the method of producing a spectro-polarimetric filter with a single-layer metallic grating filter and the method of using dielectric stacks have a similar manufacturing problem. That is, both require each pixel in a multispectral polarimetric array to have a different height than it's neighboring pixel. This is because, to perform spectral tuning, height variations,

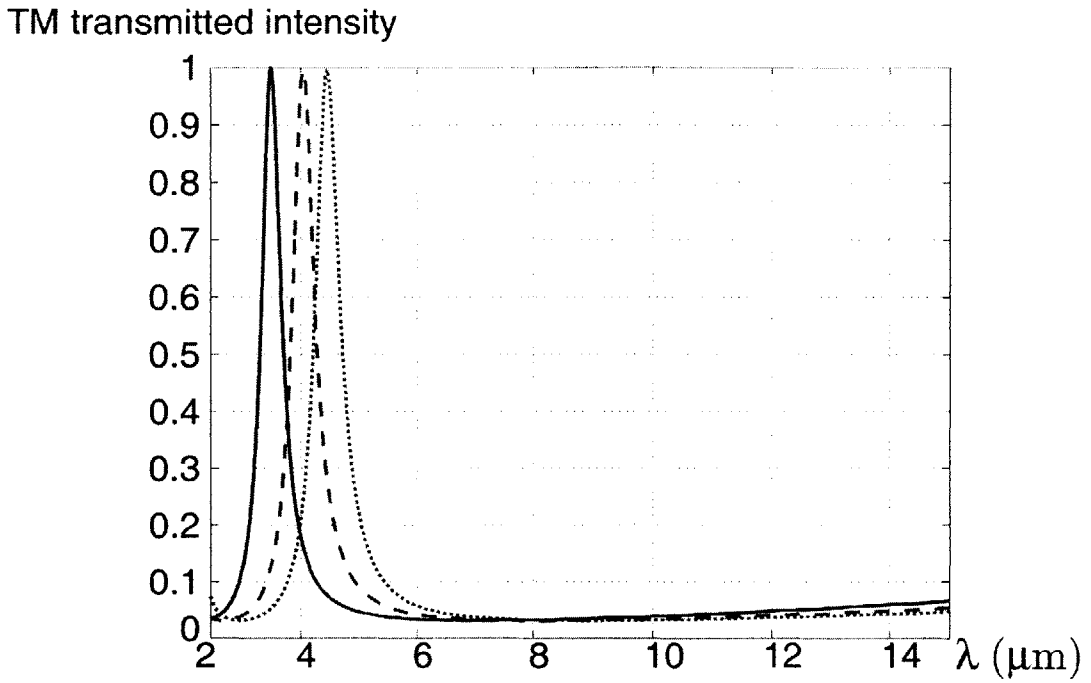

Figure 4-12: TM transmitted intensity for three single-layer metallic-grating filters with dielectric fill plotted across the MWIR and LWIR. For each of the filters, Λ=0.72μm, n_f=3.43, and w_m=0.5μm.. For the 3.5μm peak filter (green solid line), h=0.50μm. For the 4μm peak filter (blue dashed line), h=0.56μm. And, for the 4.5μm peak filter (red dotted line), h=0.62μm.

whether in a dielectric stack, or in the height of the metal filter must occur. In terms of ease of manufacture, this is certainly not ideal. While it is not impossible to perform such fabrication, it would be beneficial to design a spectro-polarimetric filter that could be tuned by adjusting only the transverse properties of the grating filter (that is w_m and Λ) instead of the height of the metal, h. Indeed, while this is not practical with a one-dimensional single-layer grating filter filter, a double-layer metallic grating filter that allows for spectral tuning while keeping all metal and dielectric layers level will be discussed later.

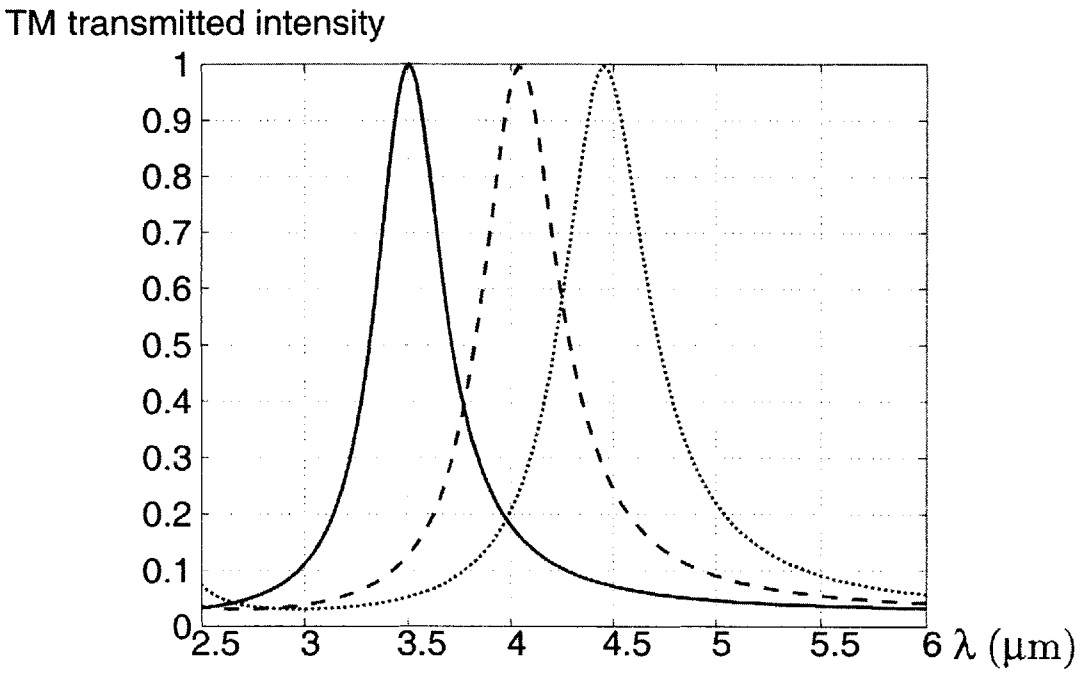

Figure 4-13: Magnified view of the TM transmitted intensity for three single-layer metallic-grating filters with dielectric fill plotted in the MWIR. For each of the filters, Λ=0.72μm, n_f=3.43, and w_m=0.5μm. For the 3.5μm peak filter (green solid line), h=0.50μm. For the 4μm peak filter (blue dashed line), h=0.56μm. And, for the 4.5μm peak filter (red dotted line), h=0.62μm.

Single-Layer Metal-Grid with Extra Dielectric Fill

An additional design possibility, and a demonstrative example, of a single layer-dielectric grid filter is drawn in Figure 4-14. This filter consists of the proposed single-layer metallic grating filter with dielectric fill, discussed previously, but this time in simulated with a dielectric substrate of the same material that is used for the fill, in this case Silicon with n_f=3.43. The benefit of this design is a further narrowing of the bandwidth of the primary transmission peak. The dielectric fill on top of the grating and the grating height were chosen to be the same, at $h = d = 0.5\mu$m. n_s was chosen to be 1, though changing n_s will primarily affect the overall transmitted intensity of the TM light, in accordance with Fresnel's equations, assuming a substrate substantially thicker than the coherence length of incident light. Additionally, the grating pitch, Λ, would also need to be adjusted depending on the index of refraction of the substrate, in order to properly place the Rayleigh anomaly. Due to the increased Fabry-Perot dielectric cavity size $(d + h)$, additional resonant modes appear. To kill the lower-order resonant mode, the grating pitch is chosen appropriately. In this case, Λ=0.72μm, which gives the first Rayleigh anomaly at approximately λ=2.47μm. This can be seen in Figure 4-15 as a null. Like in the previous case, w_m=0.5μm.

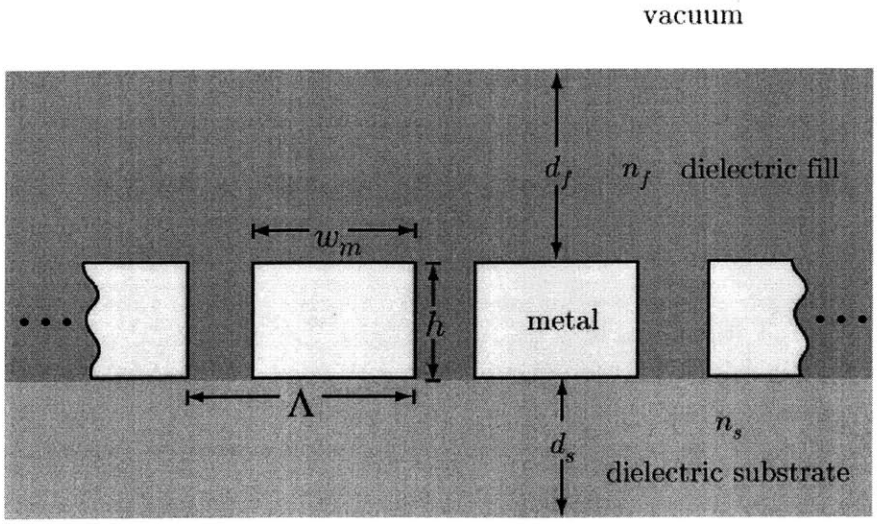

Figure 4-14: Single-layer metallic-grating filter with additional dielectric fill and substrate. Λ is the grating pitch, w_m is the individual metal width, h is the height of the metal grating, n_s is the index of refraction for the substrate, n_f is the index of refraction for the fill, d_s is the height of the substrate, and d_f is the additional dielectric fill height on top of the of the metal grating layer.

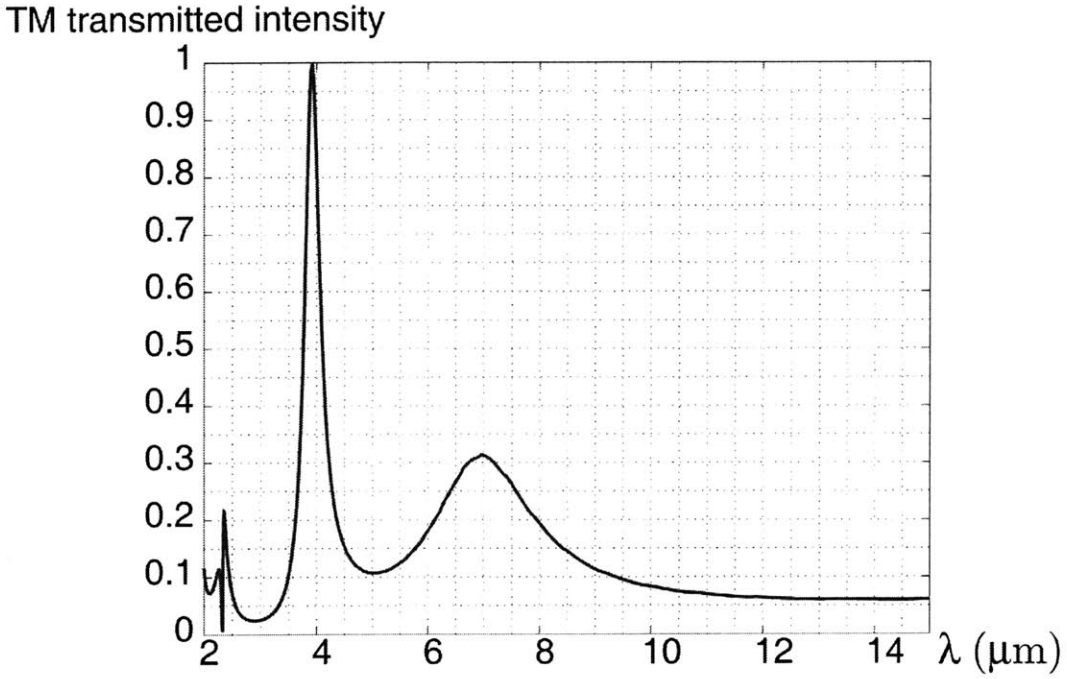

Figure 4-15: TM intensity transmittance for a single-layer metal grating with additional dielectric fill, effectively extending the dielectric Fabry-Perot cavity and further adding to the vertical resonances caused by the longitudinal extent of the metallic grating. Note the Rayleigh anomaly null at λ=2.47μm (the effective grating pitch due to the presence of the dielectric), as well as the additional lobe near λ=7μm, due to the added height of the dielectric cavity (d+h).

4.2.5 Single Layer Metallo-Dielectric Coupled with Absorbing Layer and Fabry-Perot Cavity: Microbolometer Design

The previous single-layer metallic grating designs were compatible with modern cooled MWIR and LWIR detector technologies such as InSb, MCT, or HgCdTe. With such detector technologies, the integrated spectro-polarimetric filtering layer can be deposited directly to the detector surface or placed immediately above the detector's surface on a separate substrate.

However, with the advent of microbolometer technology, additional design criteria are imposed. Current microbolometer technology is useful for uncooled, inexpensive, infrared-imaging applications. Microbolometer arrays are most commonly fabricated using CMOS-compatible processing technology. Thus, a CMOS-compatible spectral and polarimetric filtering technology that could be incorporated into the manufacture of the sensor, might be advantageous in bringing down the cost and increasing the functionality of infrared multispectral polarimetric imagers.

Illustrated in Figure 4-16, is a simplified diagram of a representative microbolometer (with the addition of a spectro-polarimetric filter on top). A microbolometer consists a light-absorbing layer (usually containing iron), a piezoelectric material, and transparent electrodes in the top layer. In order to increase the efficiency of such a microbolometer, most often a resonant cavity is placed behind the absorber and a mirror is formed at the bottom of the structure (usually made from Aluminum or Gold). The vacuum cavity is usually a $\lambda/4$ cavity to the design wavelength, in order to keep as much of the thermal radiative energy from the IR within the cavity, and therefore have as much of it absorbed by the absorbing layer of the microbolometer as possible.

In Figure 4-17 is the model used for simulating the microbolometer and coupled spectro-polarimetric filter design. Light is nominally incident from the top. A single-layer metallic-grating filter of height, h, and pitch, Λ with dielectric fill of index of refraction, n_f, is placed on top of an absorbing dielectric substrate of complex

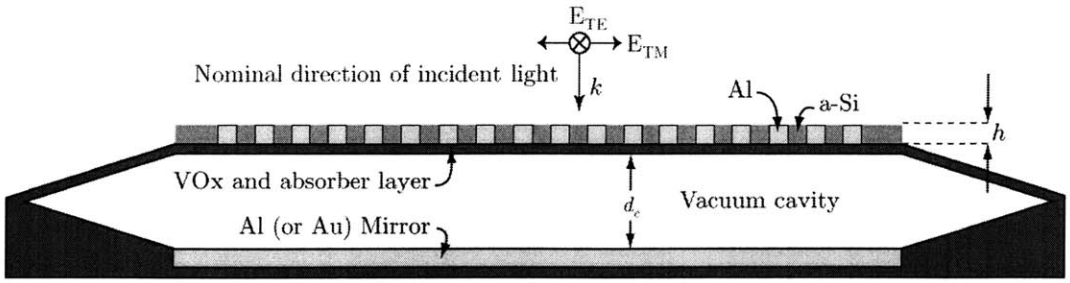

Figure 4-16: Proposed microbolometer design. Light is incident from the top. A metallic-grating structure with dielectric fill is fabricated on top of the piezoelectric and absorbing layers of the microbolometer. Incident light is initially filtered by the metallic-grating structure (grey boxes) with dielectric fill (orange). Additional spectral filtering occurs within the vacuum cavity, which is a quarter-wavelength cavity at the designed operating wavelength. A reflective layer or either Aluminum or Gold is deposited on the bottom layer of the vacuum resonant cavity to ensure optimum absorption by the absorbing layer of the microbolometer.

refractive index, n_s and height d_s. At a distance d_c below the bottom of the dielectric substrate is placed an aluminum mirror.

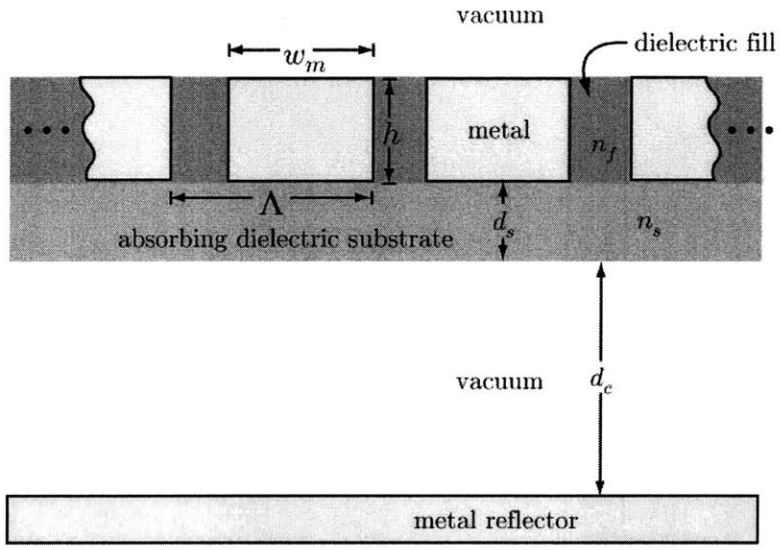

Figure 4-17: Microbolometer model used for simulation. Light is incident from the top. w_m is the metal width, Λ is the grating pitch, h is the grating height, n_f is the index of refraction for the grating's dielectric fill. n_s is the complex index of refraction for the absorbing dielectric layer, and d_s is the thickness of the absorbing dielectric layer. d_c is the cavity length between the absorbing dielectric layer and metal-reflector.

The presence of a coupled external cavity enabled the design of a dual-purpose microbolometer. This filter performs both LWIR and MWIR filtering simultaneously. In order to switch from LWIR to MWIR operation, either a long-pass filter or short-

pass filter would need to be placed in the optical path of the imaging system.

Again, much as in the previous single-layer metallic grating filter design, the grating pitch and metal width is kept constant, and the only variation occurs in h, the height of the metal grating.

For all three spectral designs, Λ=1.8μm, w_m=0.9μm (for a 50% duty cycle), n_f=3.74, d_s=0.1μm, d_c=2.5μm. The values used for d_s and d_c were the actual values used in the manufacture of a current microbolometer arrays [8, 84, 85, 86, 87, 88]. To demonstrate cavity tuning in the LWIR as well as to create a spectro-polarimetric multispectral filter in the MWIR, the grating height, h, was chosen to be 0.6μm, 0.7μm, and 0.8μm for three separate filters.

In Figure 4-18, the simulated MWIR absorption by the absorbing substrate is plotted. Note that the curve is very similar to the transmittance curve of the single-layer metallic grid structure with dielectric fill. However, due to the external cavity, there is now significant MWIR transmission, and the cavity can be tuned by changing the grating height h, as demonstrated in Figure 4-18.

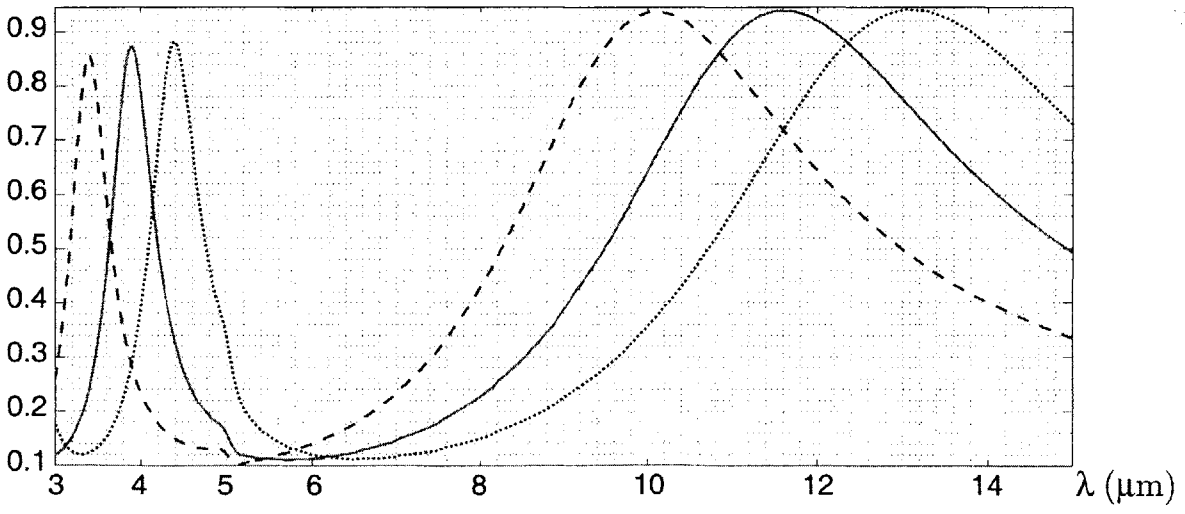

Figure 4-18: Simulated microbolometer detector absorption in the MWIR and LWIR. w_m=0.9μm, Λ=1.8μm, n_f=3.74, d_s=0.1μm, d_c=2.5μm. h=0.6μm (red dashed line), h=0.7μm (green solid line), and h=0.8μm (blue dotted line).

4.3 Dual-Layer Metallo-Dielectric Filter

To overcome the potential manufacturing difficulties associated with a one-layer structure, a two-layer structure was designed for the purpose of infrared spectro-polarimetric filtering. While the one-layer metallic-grating dielectric-filled structure requires variation in grating height to produce spectral tunability, it is much preferred to have each metal and dielectric layer to be of uniform height, independent of the center wavelengths of the filter's transmission peaks. While this leads to additional absorption losses due to the extra layer of metal, it greatly simplifies the manufacture process by only requiring one fabrication mask for an entire filter array. This eliminates a significant number of manufacturing steps and allows for rapid manufacture of filters with different spectral bandpasses. Additionally, a two-layer metallo-dielectric filter structure, while having thinner individual metal layers than the single-layer metallo-dielectric grating design, is taller overall than the single layer design due to the internal dielectric fill layer. However, peel-off problems are not a concern, as they would be with multi-layer dielectric filter designs, since the metal and dielectric layers are of uniform height across the entire surface of a mosaicked filter array.

4.3.1 Two-Layer Dielectric Embedded Design

The two-layer embedded design proposed here has manufacturing benefits over the single-layer design. Namely, by adjusting only the metal width, w_m, in both the top and bottom layers of a two-layer metallic grating structure, wavelength selectivity can be obtained.

Figure 4-19 shows the general setup for a two-layer grating structure. The top-most layer has metal width, w_m, metal height, h, and pitch Λ. The bottom layer, a distance d_f from the top layer, also has metal width w_m, metal height h, and a grating pitch of Λ. Both metal layers are embedded within a dielectric fill of index of refraction, n_f.

As seen for the single-layer problem, the primary MWIR transmission peak location does not depend strongly on the width of the metal, but instead depends more

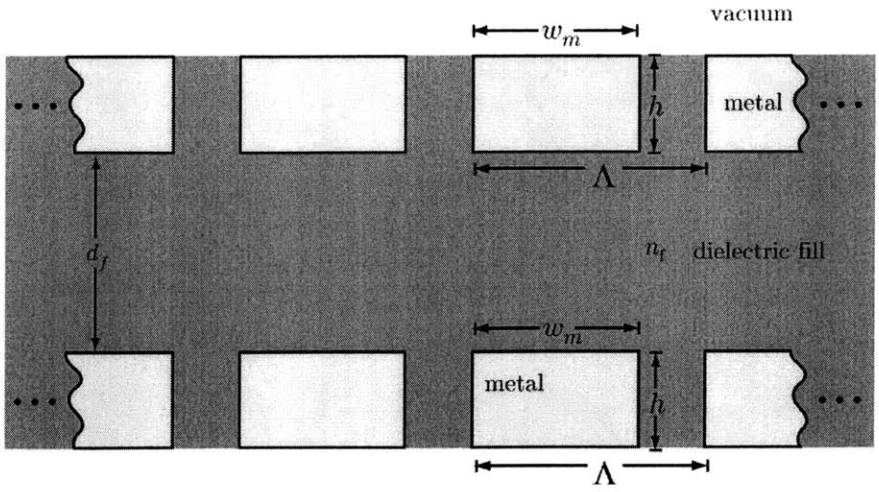

Figure 4-19: Two-layer metal grating with dielectric fill and dielectric spacer. Two metal gratings are embedded within the same material of refractive index, n_f. The gratings are spaced a distance d_f apart. The top grating has a grating pitch, Λ, a grating height, h, and a metal width, w_m. The bottom grating also has a grating pitch, Λ, a grating height, h, and a metal width, w_m. Light is nominally incident from the top.

heavily on the height of the single-layer metallic-grating. However, as seen with the microbolometer design, when a single-layer metallic grating is coupled with an external cavity, LWIR transmission may result. Indeed, through coupling two metallic grating filters, LWIR TM transmission tunability can occur.

By separating two metal gratings with dielectric fill, a psuedo-quarter-half-quarter wave (QHQ) filter is produced. Since light slows as it passes between the metal (slows more for longer wavelengths than shorter wavelengths) of the grating with respect to light traveling unimpeded through the center dielectric fill, this filter is effectively a $Q_H H_L Q_H$ filter. Or by using quarter-wave stack shorthand notation, it acts as a aHLLHs filter. This filter provides high transmittance for it's design wavelength. In the design case presented here, Λ=0.72μm, h=0.24μm, d_f=0.52μm, and n_f=3.43. Therefore, one would expect near unity transmittance at $\lambda = 2d_f n_f$ =3.57μm. Indeed, in Figure 4-20, high transmittance is observed. However, when the central dielectric layer acts as a quarter-wave layer and the two metallic gratings act as eight-wave layers, the entire structure acts more like a low-pass filter (passing longer wavelengths), also shown in Figure 4-20. But, unlike in the MWIR, the spectral resonance effects in the LWIR are not caused by the vertical resonances inside each

metal grating layer. Instead, the peak transmission in the LWIR is determined by the transverse size of the metal.

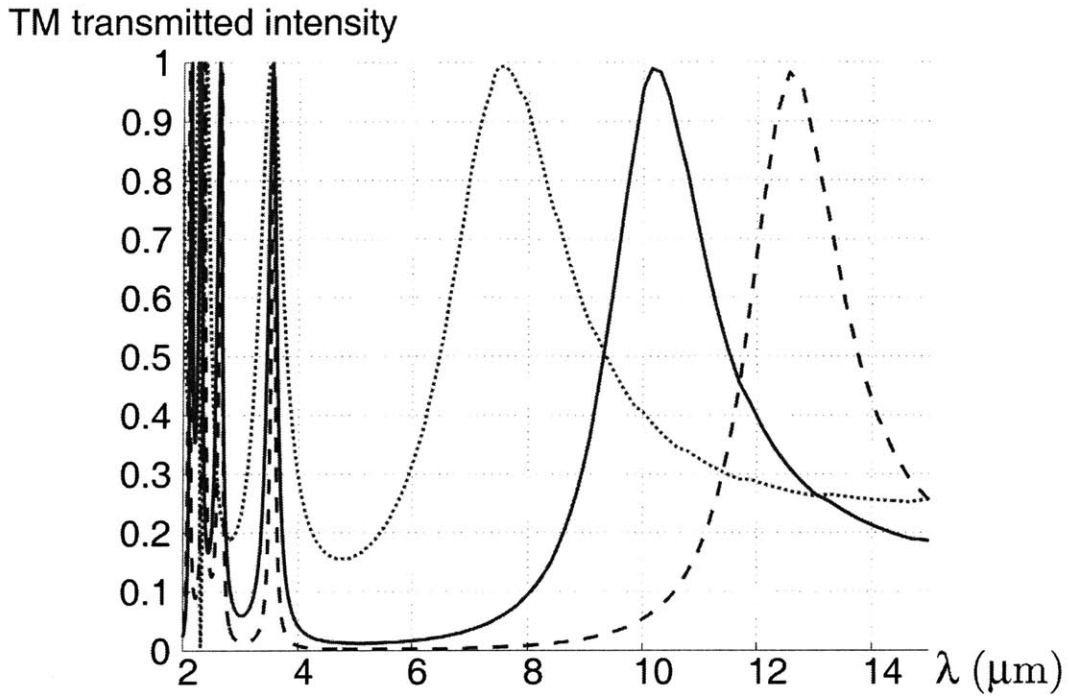

Figure 4-20: Double-layer metallic grating filter TM transmission curves in the MWIR and LWIR. This figure demonstrates the steadfastness of the MWIR TM transmission peak with respect to the LWIR peak as the grating metal width is changed while all other system variables are held constant. Λ=0.72μm, h=0.24μm, d_f=0.52μm, and n_f=3.43. Three different cases are shown, each representing a different metal width: w_m =0.12μm (red dotted line), w_m =0.30μm (blue solid line), and w_m =0.52μm (green dashed line)

Figure 4-21 demonstrates the property that changing metal width, w_m, alters the peak location of the LWIR transmission. By changing w_m, we are able to alter the effective length of the quarter-wave center cavity and therefore the peak transmission wavelength in the LWIR. As the metal widths, w_m get wider, therefore narrowing the dielectric-filled regions of each grating, the LWIR transmission peak moves toward longer and longer wavelengths. As w_m become smaller, the cavity begins to look increasingly like an open cavity of optical path length $n_f(2h + d_f)$.

The curves plotted in Figure 4-21, from left to right, are for w_m =0.12μm, 0.30μm, and 0.52μm.

As demonstrated, the benefits of a two-layer design for long-wave filtering, include

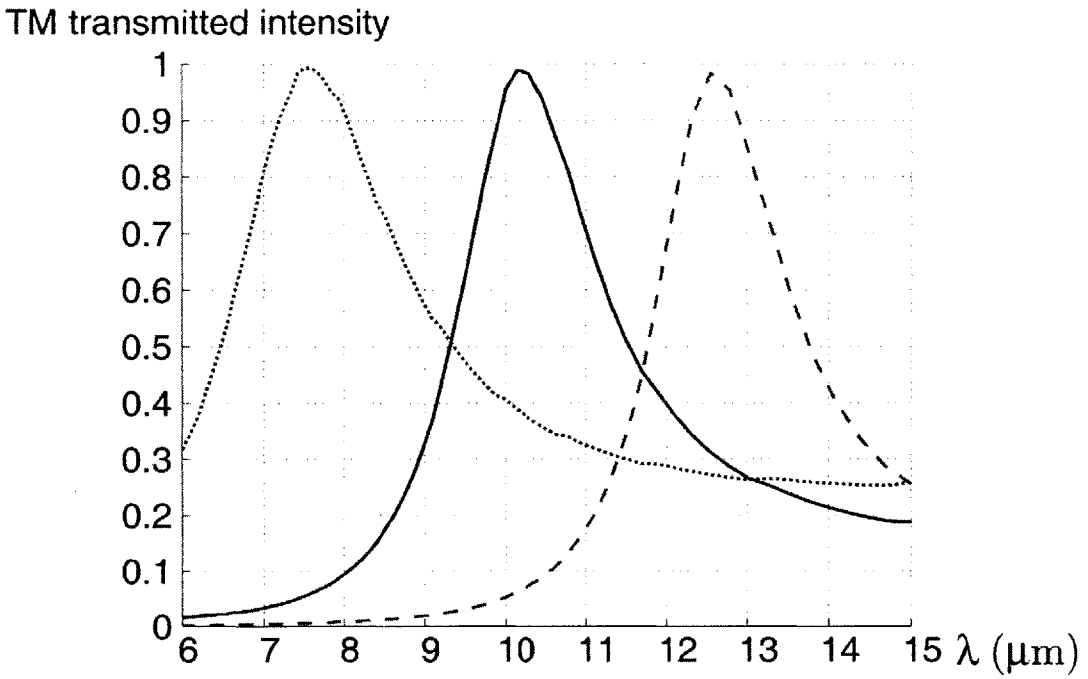

Figure 4-21: Double-layer metallic grating filter TM transmission curves in the LWIR. Λ =0.72μm, h=0.24μm, d_f=0.52μm, and n_f=3.43. Three different cases are shown, each representing a different metal width: w_m =0.12μm (red dotted line), w_m =0.30μm (blue solid line), and w_m =0.52μm (green dashed line)

the ability to adjust peak transmission wavelength by adjusting only the transverse properties of the detector. This enables the manufacture of structures that remain flat across the entire detector surface. This means that complex masking techniques to sputter different heights of metal or dielectric are not required.

However, multi-layer dielectrics have at least one significant disadvantage. In simulation, the interaction between layers is strongly coherently coupled. However, thermal IR sources tend to have short coherence lengths. Indeed, most thermal IR sources have a coherence length on the order of the structure sizes in question. Because of this, spectral peaks will not be as sharp as if the source was a highly-coherent IR source, such as an infrared laser. Another problem with multi-layer structures is efficiency. With each additional layer, less light is able to escape the structure due to absorbance by the metal layers as well as absorbance and scattering due to the dielectric film.

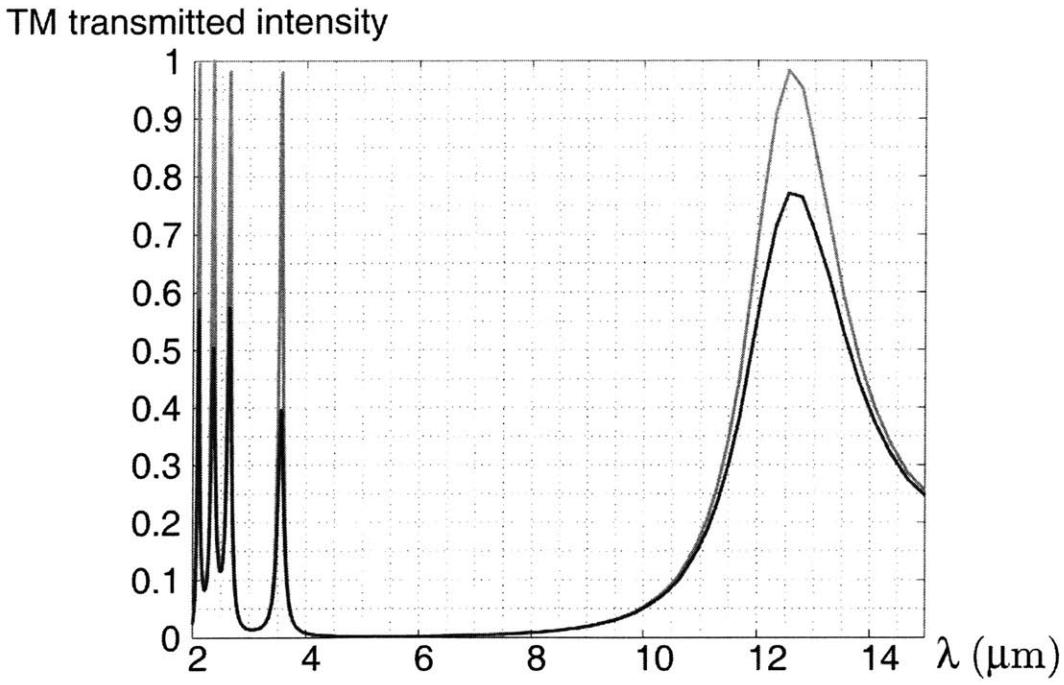

Figure 4-22: Double-layer metallic grating filter TM transmission curve for the w_m=0.52μm case. The top line (orange) is the calculated transmission curve assume a PEC metallic grating. The bottom line (blue) is the calculated transmission curve for an Aluminum grating. It is important to note that only relative peak intensity is reduced, peak transmission wavelengths remain the same.

Effects of Grating-Layer Alignment on Filter Transmission Spectra

A benefit gained by using sub-wavelength multi-layered metal grating filters, is that lateral or transverse alignment is relatively unimportant. As long as there is no rotation between the metal grating layers, the filter will function identically over the design wavelengths independent of any offset between layers. Note, this is only true in the sub-wavelength regime. When the wavelength of incident light and the feature size of the filter structure is similar, all bets are off.

In Figure 4-23, grating parameters are defined as before. However, an additional term, w_o, is included. This is the offset between grating layers. An offset of $w_o = \Lambda$ would be the same as $w_o = 0$, which is the case when both layers are aligned in the vertical direction.

Because the structural components of the filter are much smaller than a wavelength, diffractive effects do not predominate as they would for shorter wavelengths. Since diffractive effects depend on path-length within the filter, one can use ray-optics

to approximate accumulate phase and whether a certain wavelength will experience constructive or destructive interference at the output. However, in the regime where diffractive effects are negligible, that is when the wavelength is much larger than any of the filter components, using ray-trace arguments does not make sense, nor does it lead to consistent answers. Instead, the filter can be viewed as only depending on longitudinal variations for long wavelengths. Therefore, any grating position shift in the transverse direction of one or both of the metallic grating filters has little to no effect on the filter's long wavelength transmission characteristics.

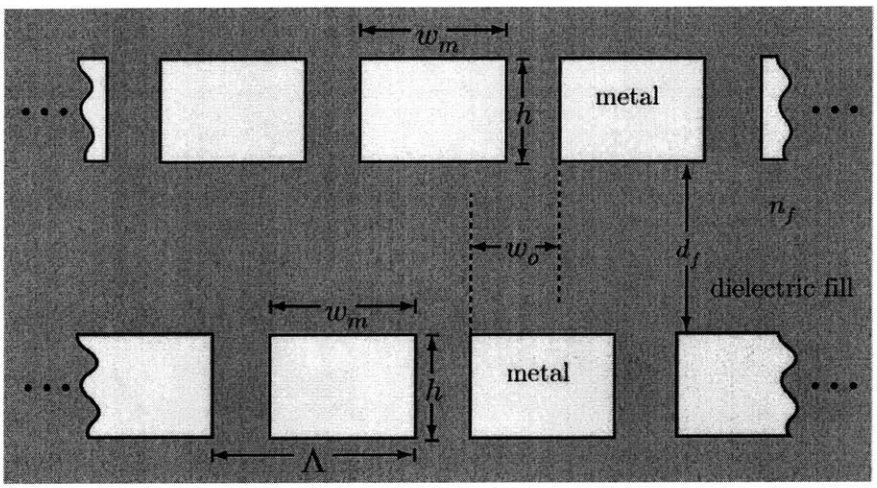

Figure 4-23: Two-layer metallic grating spectral-polarimetric filter. w_o is the relative grating shift of the top grating with respect to the bottom grating. w_m is the metal width, h is the metal height, Λ is the grating pitch, n_f is the index of refraction for the embedding dielectric, and d_f is the distance between metal layers.

In Figure 4-24, the transmission spectra from the two-layer metal grating filter is plotted for a relative shift of $w_o = m\Lambda$, $m \in$ Integers, $w_o = \Lambda(m \pm 1/4)$, $m \in$ Integers, and $w_o = \Lambda(m + 1/2)$, $m \in$ Integers. Note the same transmission curve between all three cases for wavelengths greater than 3μm. While for wavelengths less than 3μm, there is poor overlap, as is expected.

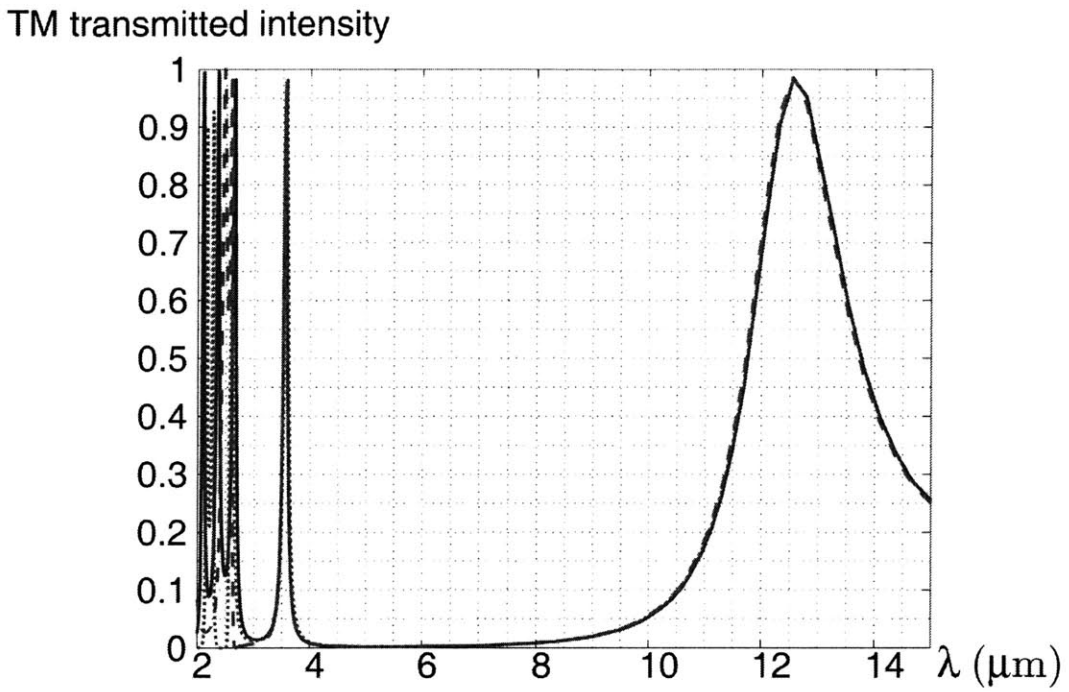

Figure 4-24: TM transmission curve for three two-layer metal grating filters with, each with Λ=0.72μm, h=0.24μm, d_f=0.52μm, n_f=3.43μm, and w_m=0.52μm. Each curve corresponds to a different grating offset, w_o. $w_o = m\Lambda$, $m \in$ Integers (blue solid line), $w_o = \Lambda(m \pm 1/4)$, $m \in$ Integers (red dotted line), and $w_o = \Lambda(m + 1/2)$, $m \in$ Integers (green dashed line).

4.4 Notes on Mutli-Layer Metallo-Dielectric Filters

Multiple-layer metallic gratings have several benefits. This first of these includes sidelobe suppression for the case of non-subwavelength structures. Multiple layer gratings, at least when on the order of the wavelength being filtered, allow for filtering over a large range of angles. Multi-layered filters also enable flatter passbands and sharper band-stops. In microwave spectro-polarimetric filters, multi-layered metallic stripline gratings have been used for nearly half a century. Indeed, it was these stripline structures that originally motivated this thesis. However, in the microwave regime, such multi-layer structures are necessary since a wide variety of high-index dielectrics are not as readily available as in infrared filters. Also, in microwave filtering, problems of metal-dielectric expansion and air gaps play a significant role. Also, metals can be made extremely thin with respect to the wavelengths being filtered for microwave radiation. Ideally, the longitudinal depth of a metal for microwave filtering is on the order of 1/1000 the wavelength being filtered [89]. However, in the IR, metals are necessarily much thicker when deposited on a substrate with respect to IR wavelengths, so many of the microwave design rules are not applicable.

While such multi-layer stripline filters are possible in the IR, several disadvantages indicate that an optimal solution does not require complicated multi-layer (>3 layer) structures.

By using high-index dielectrics, optical filters can be made to operate efficiently over a large range of input angles. There is not a clear need for additional beamforming from multiple layers of metals. Additionally, with each additional layer of metal comes additional ohmic losses and scattering losses due to imperfect fabrication. This is one of the reasons the metals in microwave filters are designed to be so thin. Indeed, in the experiments discussed in the next chapter, each additional layer incurred significant additional TM transmission loss.

4.4.1 Effects of Fabry-Perot TM Cavity Resonances

Also, due to the limited coherence length of thermal IR sources, multiple metal layers are not needed, and indeed not useful as tools for coherently-coupled pass-band formation. When individual elements within the multi-layered grating structure end up longitudinally separated by a distance greater than the coherence length, there is effectively little coherent interaction. So, in terms of practical fabrication, a single layer will only interact with the layer immediately preceding it and the immediately subsequent layer. Adding additional layers does not provide significant benefit in a coupled sense. Practically, a layer greater than a coherence length from any previous or subsequent layer can be treated as an entirely separate system, whose transmission curve can be simply multiplied by the transmission curve any other system component outside of the coherence length.

4.4.2 Effects of Multi-Pitch Metal Wires

Because of the lack of coherent coupling for more than a couple layers of metal gratings and dielectrics, multi-pitched metal gratings can create multiple nulls in the transmission spectrum of TM light. For a coherently coupled system, using a different pitch for gratings at different levels will smooth out the spectrum and wash out the Rayleigh anomaly zeros. Simulating the spectrum smoothing is relatively trivial, but accurate simulation of partially-coupled grating elements is not. For grating elements with absolutely no coupling, simulating a structure is as simple as simulating it's parts, then multiplying the transmission spectra for each part piecewise across all wavelengths.

4.4.3 Multi-layer Power Loss and Increased Polarization Sensitivity

One additional benefit to a multi-layer system is the increased polarization selectivity of the structure. However, this comes at the price of TM power loss for each polarizing layer [66]. And, this is only of real benefit for multi-layered metallic grid structures

that have metal widths, w_m, on the order of the wavelength of light being filtered. For the case of subwavelength gratings, the cross-polarization extinction ratio is large enough not to warrant loosing power in order to gain nominally better polarization selectivity.

4.5 Microwave Spectro-Polarimetric Filtering Structures Scaled to the IR

Inherently, wavelength selective structures can be manufactured for arbitrary wavelengths, as long as conductivity, and dimensional needs are met. However, many microwave structures rely on extremely thin metals. In general, for microwave structures made of two-dimensional metallic gratings, the metals are chosen to be as thin as possible. To be analyzed as purely two-dimensional gratings, they must be on the order of 1/1000-wavelength thick [89], or of the same order of the skin depth of the metal. In microwave radar, this might mean a thickness of several hundred microns. However, for infrared wavelengths, this requires a thickness of 30 to 120 Angstroms. While it is possible to create metal films of this thickness, such films do not act as efficient conductors, and therefore as efficient reflectors at these heights.

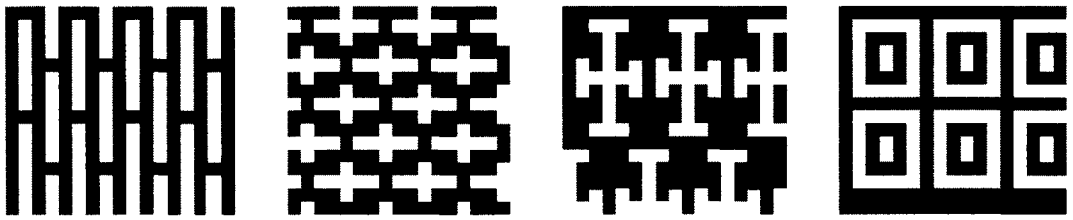

Figure 4-25: Four wavelength-selective structures. If the blue solid region represents metal, than these surfaces can be thought of as band pass filters. If the white cutout regions represent metal, these can be thought of as bandstop filter. For the case of blue representing metal these filters can be described as follows: **(a)** A slotted grid filter with rectangular apertures and a skewed (or brick layer) packing symmetry. For the case of thin slits, this can be viewed as an array of magnetic dipoles. Or, for the case of thick slits, this can be viewed as an array of slots (as opposed to dipoles). **b** A cross-type filter array with skewed packing symmetry. For the case of thin slits, this can be viewed as an array of crossed magnetic dipoles. **(c)** An array of Jerusalem crosses. For thin slits, this can be analyzed as an array of magnetic multi-poles. **(d)** An array of loop-type filters with internal slotted filters, in this case in a rectangular packing symmetry where blue represents metal.

Therefore, infrared filtering structures must be analyzed in three-dimensions, and many of the two-dimensional design rules that come out of RADAR structure engineering do not apply.

For most RADAR structures, whether they be multi-poles, loop-type filters (loaded elements), perforated hole or plate structures (unloaded elements), or combinations of these three types, several design parameters exist mostly independent of element type chosen. These parameters rely only upon the spacing between elements in a filtering array. For most structures, the larger the inter-element spacing, the narrower the bandwidth for a filter. This includes frequency and spatial-frequency bandwidth, since RADAR structures are in essence both frequency and spatial filters. Additionally, the larger the inter-element spacing, especially when the inter-element spacing is near or greater than the wavelength of filtered light, the more grating lobes (or diffracted orders) that will appear. Also, the larger the inter-element spacing, the greater the shift in filter passband frequency due to angle-of-incidence variations.

In RADAR structures, often multiple layers of metals are used. These can either have air-gaps in between, or be spaced with dielectric. Due to the thin nature of these metal layers with respect to the wavelength of incident radiation, these layers act much more like Fabry-Perot mirrors than they do in the infrared. For IR structures, we must be very concerned with the height of each metal layer and how that effects cavity resonances. In the microwave regime, this is not a huge concern.

For microwave structures, such multi-layered metals are used to create sharper passband drops and flatter bandpass tops. But, due to the multiple-layered nature of these systems, they exhibit bandwidth instability with respect to angle of incidence. To overcome the angle-of-incidence limitation for these types of structures, microwave engineers use dielectric layers at the top and bottom of these filters to reduce the sensitivity of these structures to angle-of-incidence, much as we do in the infrared. However, microwave engineers have a problem that we do not have. The center frequency of the passbands relies considerably on electromagnetic interaction at the interface between the dielectric and metal. Because of the way such structures are manufactured, and due to thermal expansion or contraction, it is difficult

to ensure that no air-gaps can form between metals and dielectrics. For the infrared, where our filters are extremely small, and relative contraction and expansion between the dielectric and metal is small, we are not overly concerned with this. But, in the microwave regime, where metals and dielectrics can be very large and experience significant expansion and contraction, this can pose a significant design and fabrication challenge.

In microwave frequency-selective filter design, as the perforated metallic layer becomes taller, the total transmitting bandwidth of a bandpass filter will be reduced. This is also seen in the infrared filters designed for this thesis. However, infrared filters tend to be much thicker with respect to wavelength than even thick microwave filters. So, in the infrared, we will necessarily have narrower bandwidth than for the same filter type in the microwave regime.

For microwave structures, where designers are concerned about angle stability (such as for stealth applications), using multi-pole structures is beneficial, since a very tight packing symmetry is possible. However, with slotted grid structures, because elements must be on the order of $\lambda/2$ in size, elements can not be packed as closely, and therefore side-lobe suppression (higher order mode diffraction reduction) is very difficult. For infrared imaging, this in not as much a concern, since we have tight control over the imaging optics used in such a system, and can minimize the range of input angles for light passing through our filter. In microwave, the presence of side-lobes, for a passive system, can mean easier detection through active RADAR. For an active system, side-lobes affect the ability of a RADAR system to obtain highly spatially-resolved information.

One general rule of microwave-regime frequency-selective-structure design is that the elements and the inter-element spacing should be made as small as possible given a set of design criteria. This is mostly true for the infrared as well. Though, because metal heights tend to be larger with respect to wavelength in the infrared, and this adds an additional design parameter, the requirement is not as strict. Indeed, in this thesis, the fact that the spacing was on the order of the wavelength of light was used as a design criteria, using the Rayleigh anomaly to help form the desired bandpass

structure.

In designing frequency selective structures for the microwave regime, the packing symmetry is very important. For multi-pole structures, using skewed packing symmetries enables elements to be spaced more closely together, and thereby increase the bandwidth of the filter. Additionally, by using skewed packing symmetries, the onset of grating lobes (such as happens with the Rayleigh anomaly) can be "delayed." In other words, for the infrared case, the Rayleigh anomalies can be moved into or outside of the spectrum of interest, and the passband bandwidth can be increased (by squeezing the elements closer together) or decreased (by pushing the elements further apart).

Additional detailed analysis for frequency-selective structures in the microwave regime can be found in [89, 90]. Analysis and experimental results for other authors who used the frequency-selective-structure concept in the infrared can be found in [91, 92, 93, 94, 95].

In the next section, only the single and double-layer slotted grid wavelength-selective structure are explored as a possible infrared filter design. In Chapter 5, results from a single and double-layer slotted grid fabricated using a CMOS process are also analyzed. On the same CMOS chip, several single and double-layer wavelength-selective-structures were fabricated– polarized FTIR transmittance data is presented for these structures in the Appendix. However, only the slotted grid structure is modeled, simulated, and compared with experimental results.

4.5.1 Single and Multi-Layer Perforated Metal Grid Filters

Perforated grids of rectangular apertures are common structures used in microwave spectral and polarimetric filtering. Significantly greater light can pass through a grid of rectangular apertures than a single aperture alone. Though, the spectral filtering characteristics of the single aperture are substantially retained. The perforated metallic grid is one method to perform spectral filtering with only a single metal layer. It was shown that spectral and polarimetric filtering with a single metallic grating with dielectric fill is possible, but in order to adjust the passband location, the height of

the single-layer metallic grating had to be adjusted. In order to overcome this fabrication obstacle, two-layer metallic gratings were proposed that allowed for wavelength selection by adjusting only the transverse values of the metallic grating structures. It would be beneficial to be able to do the same thing, but with a single metallic layer. For a one-dimensional grating, this is difficult. However, with the addition of another dimension, to create a two-dimensional grating, such wavelength selection is possible.

However, as demonstrated in the next chapter, such structures are inherently lossy when structure components are on the order of size of the wavelengths being filtered. And, unlike the metallic grating structures presented earlier, metallic grid structures reject much more of the desired transmitted polarization (TM), and therefore tend to be less efficient. Fabrication-wise, these two-dimensional grating structures are slightly more difficult to manufacture than one-dimensional grating structures, and tolerances to manufacturing errors are quite a bit smaller for two-dimensional gratings than one-dimensional gratings. Of course, extremely high transmittance from two-dimensional gratings has been reported, specifically for the case of subwavelength hole arrays [96]. However, mixed results have been obtained in the laboratory for such perforated metal screens [96]. In order to perform spectral filtering and polarization filtering, the RADAR-based approach of a perforated grid of rectangular apertures is explored in this section.

Single Layer Metallic Grid

For a perforated grid, one can first look at the unit cell as a modified rectangular waveguide. Indeed, the rectangular cell, as illustrated in Figure 4-26, does not act as a perfect waveguide due to its limited height, h. If h were made extremely large compared with w_{hx} and w_{hy}, the transverse width of each rectangular aperture in the x and y directions, such a grid could be thought of as a collection of perfect waveguides and would exhibit a very large range of TE (x-polarized) and TM (y-polarized) modes. However, due the the manufacturing constraints on h, as well as the need to keep TE (x-polarized) transmission efficiency high, h is chosen to be as thin as possible, while still maintaining it's high reflectivity for TM (y-polarized) light, which

means the grating has to be thick enough (much larger than the penetration depth of the metal) to effectively filter TM radiation. In practice, with high-conductivity metals, these metals can be made much thinner than the single-layer metallic grating structure, discussed previously, would allow to perform similar spectral filtering tasks. Indeed, for the simulations presented in this section, the metals were modeled without dielectric fill (ie. metals fabricated on a substrate without additional dielectric added). And, even without the dielectric fill, the maximum metal height used to obtain reasonable transmission characteristics was 3μm in height. However, there is no reason that this height can not be made much smaller (on the order of a few hundred angstroms, as has been demonstrated for other metallic-grid structures in the literature [97, 98, 99, 100, 101, 102].

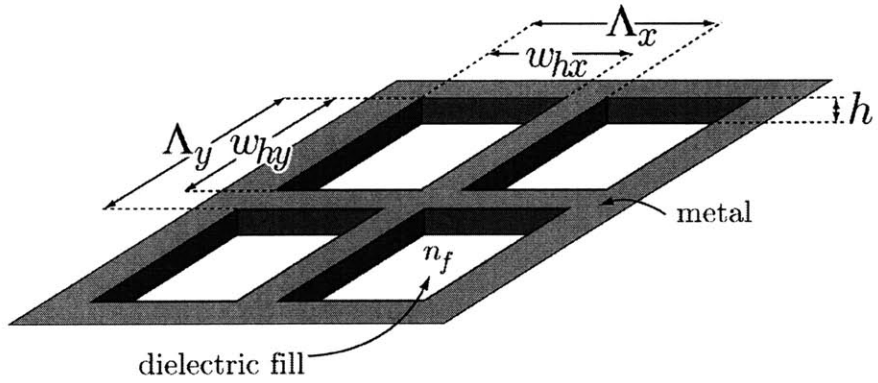

Figure 4-26: Zoomed view of a perforated metallic grid with four rectangular apertures. Rectangular apertures are equally spaced on a rectangular grid.

The design of each cell in the grid, and the corresponding properties of individual apertures in a metal screen, relies on transmission, in waveguide parlance, of TE (x-polarized) light by exciting the TE_{10} mode within the aperture.

Note that we are now using the nomenclature of waveguides instead of gratings, when talking about individual waveguide components. For a waveguide, TE is defined as an electric field whose oscillations are in the direction of the smallest transverse cross-sectional direction. In this case, TE corresponds with an electric field oscillating along w_{hx}, in the x-direction. For the sake of definition, $w_{hx} < w_{hy}$ always. In the extreme case, where $w_{hy} >> w_{hx}$, such that $w_{hy} \rightarrow \infty$ and w_{hx} is finite, the

rectangular grid structure becomes a one-dimensional metallic grating. However, in grating nomenclature, an E-field along x would be considered TM. To reduce confusion, I will refer to TE (with respect to the waveguide) as x-polarized light.

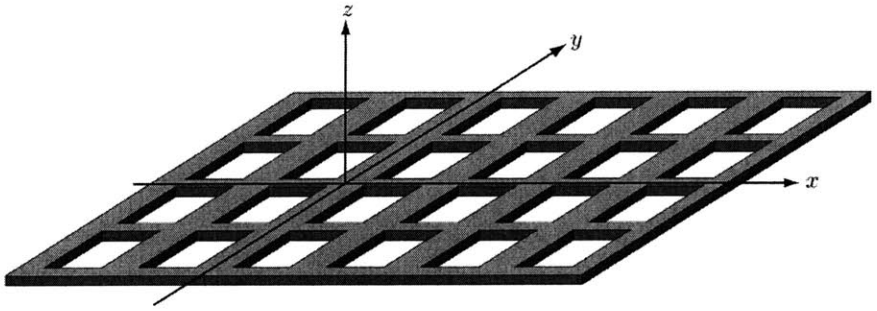

Figure 4-27: Rectangular grid of rectangular holes in a perforated metallic film.

For waveguide cutoff, where only the first mode, TE_{10}, is allowed to propagate, the values of w_{hx} and w_{hy} are determined by the need to eliminate any higher order mode propagation. Additionally, the height, h, of the waveguide must be chosen so that vertical resonances within the spectral filtering bandwidth of interest, are not excited. In general, this means that the height of the structure, h be much less than one-quarter the smallest wavelength of interest. The transverse electromagnetic modes within the waveguide provide us with the cutoff rules that $w_{hy} > \lambda/2 > w_{hx}$. This is a very strict condition. However, if we had enough control over the dimensions of the aperture at subwavelength scales, we could introduce a less stringent requirement that we would allow for dual-mode TE operation. That is, we would allow TE_{10} and TE_{01} mode excitation, and this would give us the guidance condition for our choice of filter wavelength, λ, of $w_{hy} > \lambda/2 > (w_{hx}^{-2} + w_{hy}^{-2})^{-1/2}$ Note, that the TE_{01} mode and the cuttoff condition for the first TM (y-polarized) mode, TM_{11} can, spectrally speaking, occur at very close wavelengths. And, we absolutely do not want TM (y-polarized) modes excited in the waveguide, so the more strict condition is preferred.

Using the design parameters discussed above, the transmission curves seen in Figure 4-28 were obtained. Using the waveguide definition for TE (x-polarized) and TM (y-polarized) light, the blue solid curve is the modeled TE (x-polarized) transmission for a slotted grid of rectangular holes in brick-layer type symmetry (the symmetry

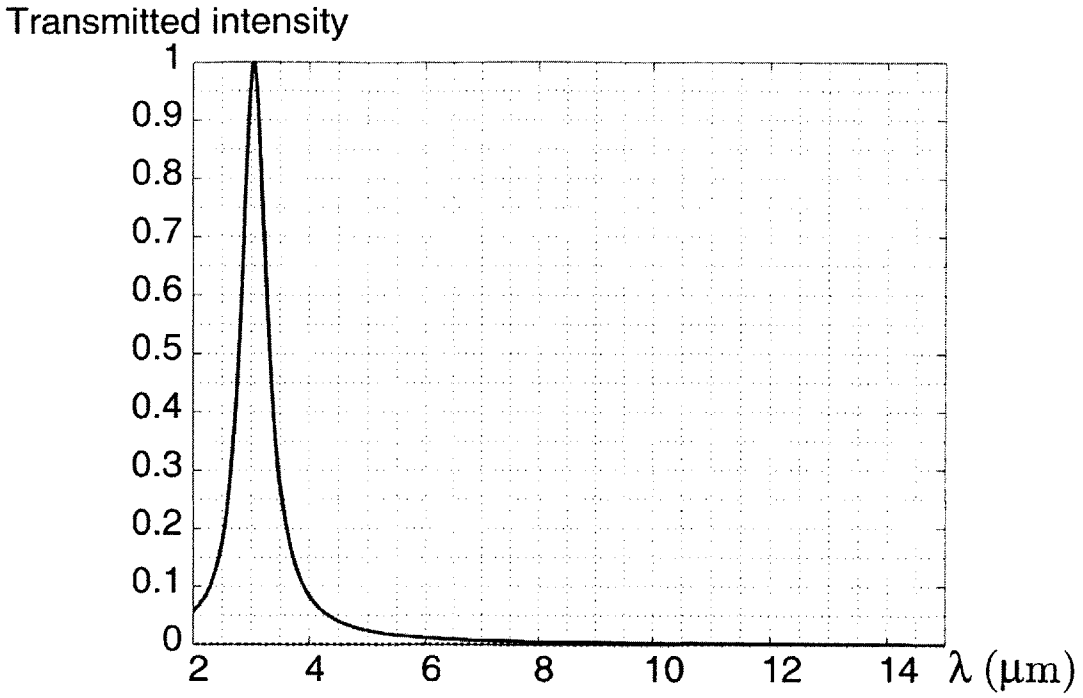

Figure 4-28: TE (x-polarized) (solid blue line) and TM (y-polarized) (dotted red line) (waveguide definition) transmittance for the rectangular slotted-grid structure. $\Lambda_y = 2.1\mu$m, $\Lambda_x = 2.2\mu$m, $w_{hy} = 1.7\mu$m, $w_{hx} = 0.35\mu$m, and h=0.3μm

shown in Figure 4-30). To create this spectrum, w_{hy} was chosen to be 1.7μm and w_{hx} was chosen to be 0.35μm. The dielectric fill was chosen to be air, n_f=1. The grating periodicity in the y-direction was chosen to be Λ_y=2.1μm. And, the grating periodicity in the x-direction was chosen to be Λ_x=2.2μm. The height of the metal layer was chosen to eliminate peaks of shorter wavelength than the primary peak within the spectrum of interest to get h=0.3μm. For computational and modeling simplicity, the metal was modeled as a PEC. Notice that the transmission spectra for TM (y-polarized) light is effectively zero (numerically, it is minimally three orders of magnitude less than the TE (x-polarized) transmittance).

Additionally, the FWHM for the primary transmission peak depends highly on horizontal resonance coupling within the grating. In general, as the spacing between slotted grid elements in the x-direction increases, ie. as Λ_x becomes larger, the transmission peak becomes sharper. As shown in Figure 4-29. For each of the three cases shown, the dimensions of the rectangular holes were kept constant, and only Λ_x was

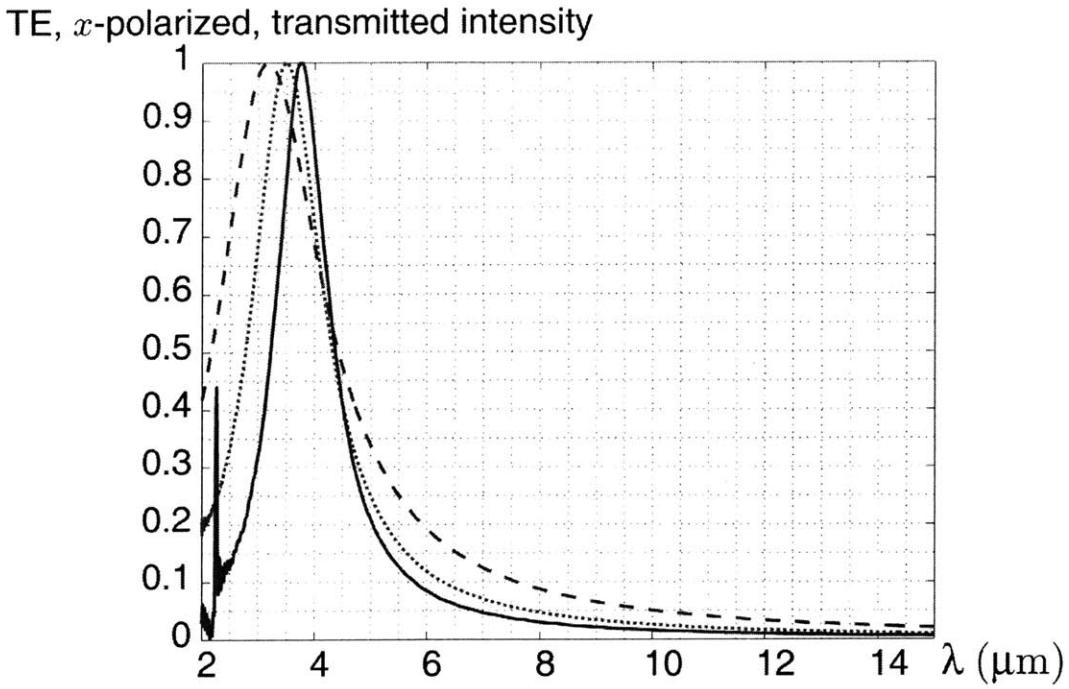

Figure 4-29: TE (x-polarized) intensity transmission for varying grating pitch. The structure is excited with TE (x-polarized) light at normal incidence. Λ_x=1.2μm (blue dashed line), Λ_x=1.7μm (red dotted line), and Λ_x=2.2μm (green solid line). Λ_y = 2.1μm, w_{hy} = 1.7μm, w_{hx} = 0.35μm, and h=0.3μm.

changed. As Λ_x goes from 1.2μm (blue dashed line), to 1.7μm (red dotted line), to 2.2μm (green solid line)), the center of the transmission peak moves toward longer wavelengths, and the bandwidth of the transmission peak also decreases. This ability to control both transmission peak location and width by adjusting the grating pitch, is in addition to the ability to control transmission spectra width and location by adjusting the length and width of the rectangular hole.

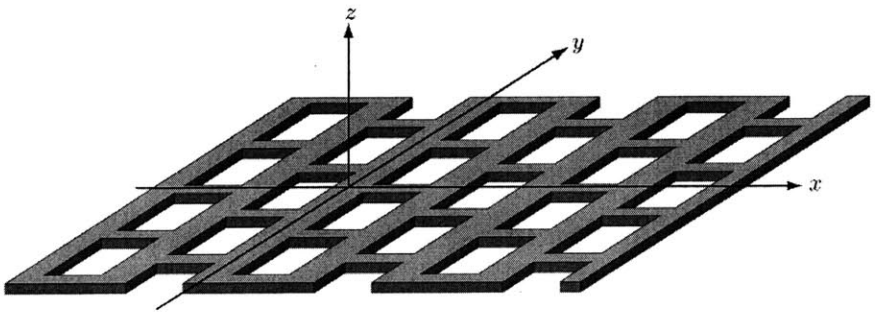

Figure 4-30: Skewed (brick-layer) grid of rectangular holes in a perforated metallic film.

Indeed, there is yet another way of adjusting the peak of the spectral curve in addition to changing it's bandwidth, and that is by changing the topology of how the rectangular holes are arranged on a grid. By using a brick-layer-topology (as shown in Figure 4-30) vs. using the rectangular topology (as shown in Figure 4-27), we can also effectively narrow the bandwidth [89]. Initially, as we made Λ_x larger, we got a narrowing of the spectral transmission bandwidth and a shift toward higher wavelengths. However, by going from a rectangular to brick-layer pattern, we can also reduce the spectral transmission bandwidth, but instead of moving the transmission curve toward longer wavelengths, we can move the curve toward shorter wavelengths. This is demonstrated in Figure 4-31. In this figure, all design variables are kept constant except for the overall stacking geometry. The red dotted line is transmission for a brick-layer topology and the blue solid line is transmission for a rectangular grid geometry.

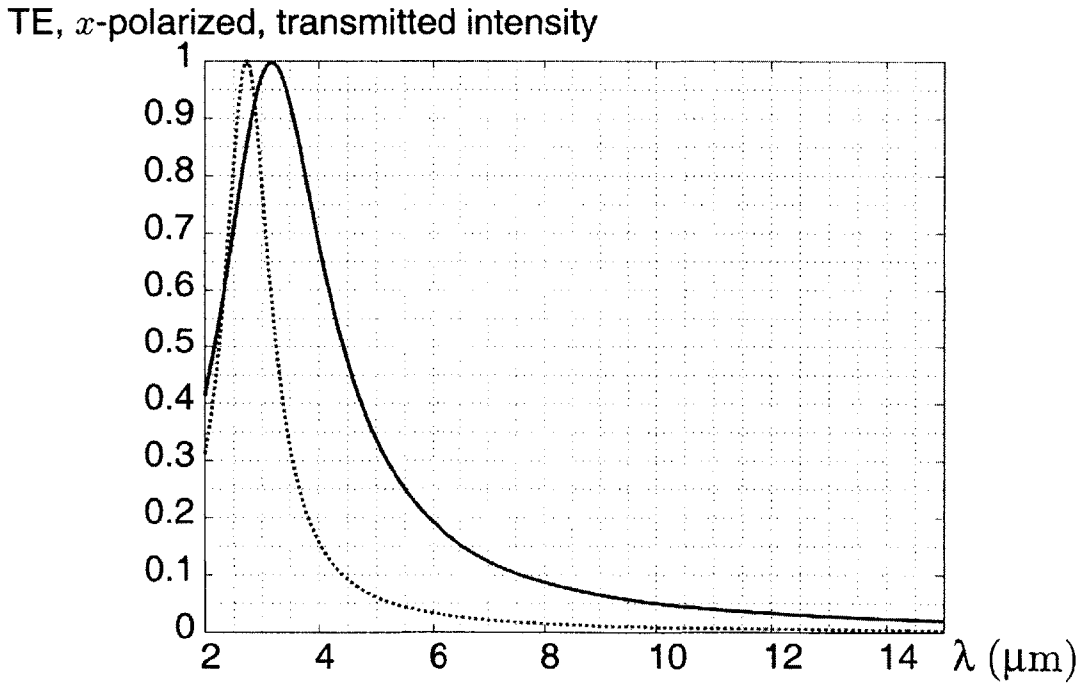

Figure 4-31: TE (waveguide defined) transmission spectra for a grid of rectangular apertures with rectangular packing symmetry (solid blue line) and skewed (brick-layer) symmetry (dotted red line).

In all, the ability to adjust the stacking geometery, the ability to adjust grating pitch, and the ability to adjust the metal width and length, allows for considerable

freedom in designing slotted-grid spectro-polarimetric filtering structures.

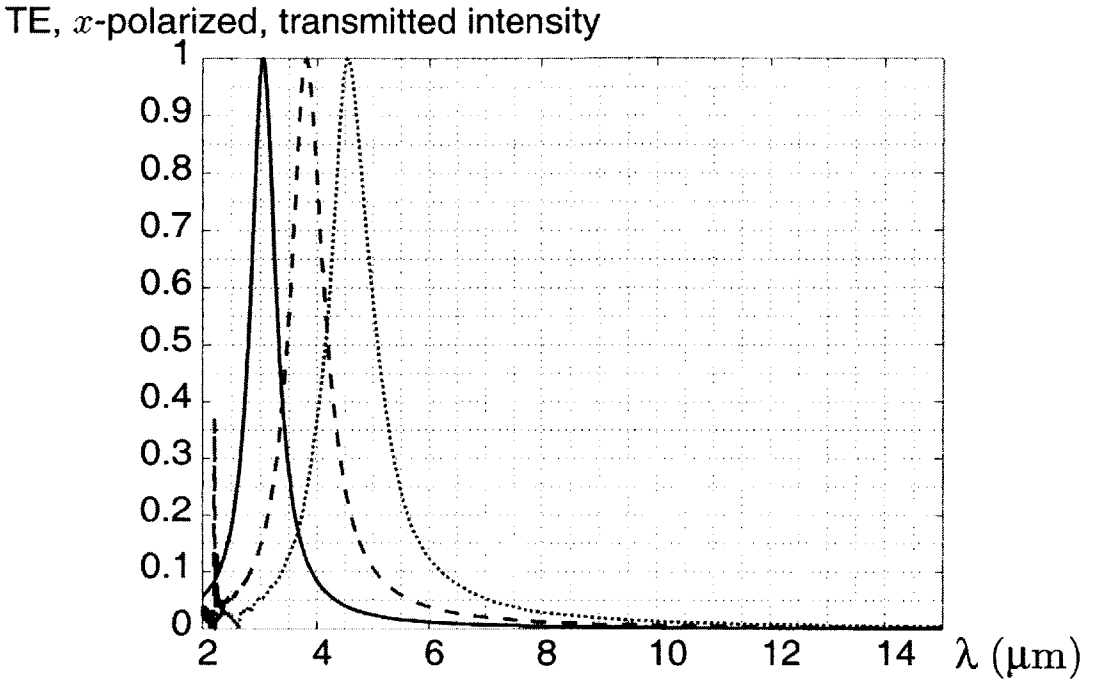

Figure 4-32: Three TE (x-polarized) transmission curves for a rectangular grid rectangular aperture metallic two-dimensional grating. h=0.3μm for each of the three filters. Solid green line: Λ_y = 2.1μm, Λ_x = 2.2μm, w_{hy} = 1.7μm, w_{hx} = 0.35μm. Dashed blue line: Λ_y = 2.5μm, Λ_x = 2.6μm, w_{hy} = 2.0μm, w_{hx} = 0.42μm. Dotted red line: Λ_y = 2.9μm, Λ_x = 3.1μm, w_{hy} = 2.4μm, w_{hx} = 0.49μm.

In Figure 4-32, three filters were designed, with peaks in the MWIR. These were designed by linear scaling of both pitch and metal width. By linear scaling, as the wavelength peak location goes towards longer wavelengths, the bandwidth of that peak also increases. In order to maintain constant bandwidth, the pitch of the grating should be increased faster than the transverse dimensions of the rectangular hole. However, the design tunability of such a structure is evident.

Multi Layer Metallic Grid

With the ability to control the bandwidth and peak location of passbands using a single layer structure, and due to increased losses that occur in multi-layered systems, multi-layered metallic grids do not add significant benefit, at least as they pertain to the scope of this thesis. However, two-layer grids enable flattening of the top of the

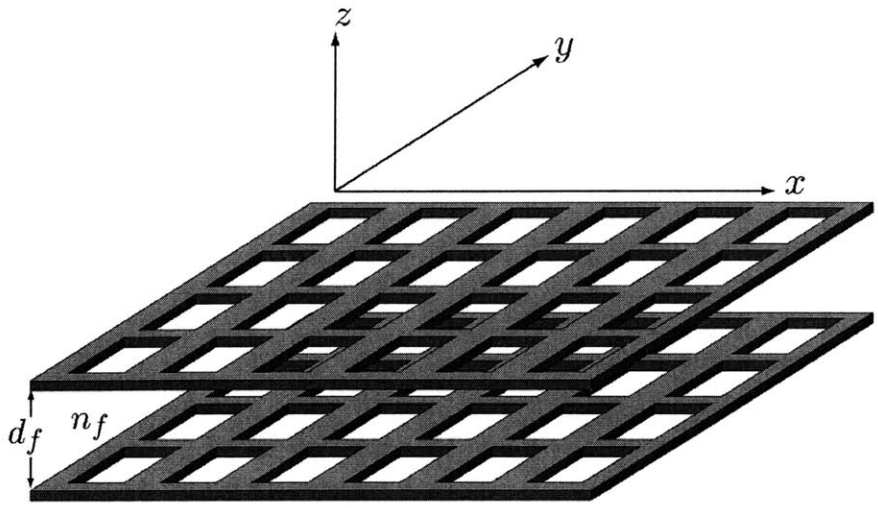

Figure 4-33: Two-layer perforated metallic grid design. Layers are spaced d_f apart.

passband spectra as well as narrowing the FWHM of the transmitted spectra. This narrowing is due to the Fabry-Perot-like resonance between the two metal layers, adding to the spectral selectivity of each layer. The flattening of the transmission curve comes from the adjacency of the peaks of the Fabry-Perot cavity resonance and the metallic grid waveguide bandpass. By aligning the single-layer peak with the Fabry-Perot peak (the physical layers remain aligned), a flattening of the passband occurs, as demonstrated in Figure 4-34. For this case, the distance between the layers was chosen to be the $\lambda/4$, or d_f=0.85μm. In Figure 4-34, the two-layer structure is represented by the solid blue line, and the corresponding transmission curve for the single layer structure is plotted as the dotted red line.

Effects of Spot-Size on Perforated Metal Film Construction

As is discussed in further detail in the subsequent chapter, CMOS manufacture processes use a photolithographic mask to pattern metal layers. Depending on the process used, the light used to create the masks, or the light used to transfer the mask pattern onto the substrate/subsequent CMOS layers, has a finite wavelength. As long as the wavelength is small, you can reproduce the edges of the rectangular aperture with a high degree of accuracy. In practice, it is difficult to reduce the spot size to smaller

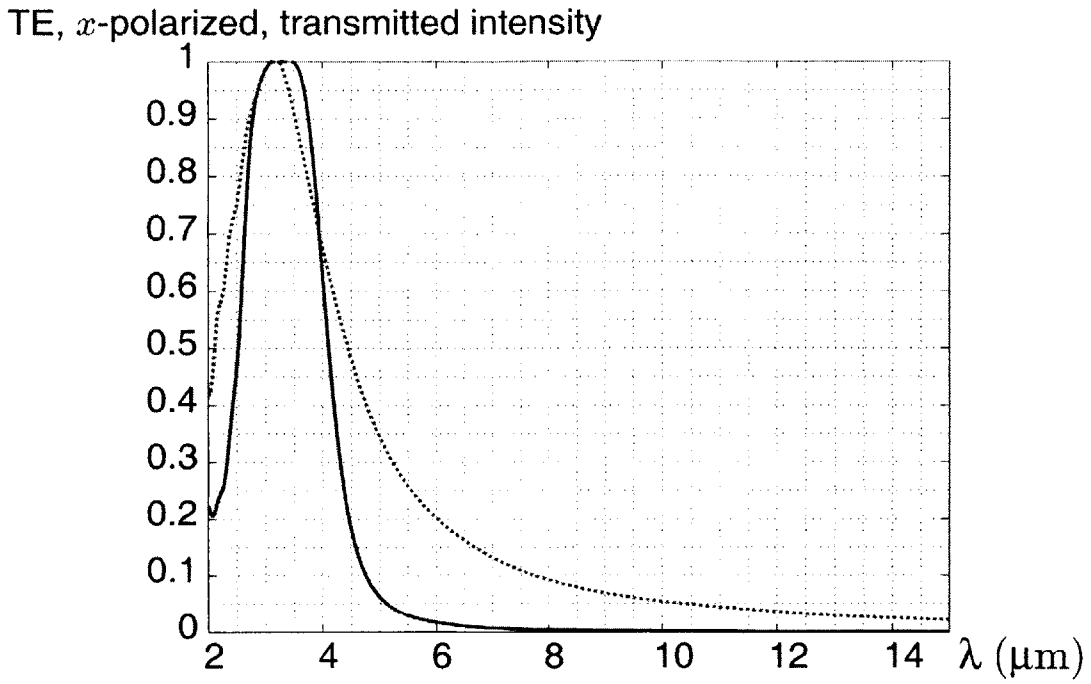

Figure 4-34: Two-layer (solid blue line) and single layer (dotted red line) rectangular grid rectangular aperture metallic grating TE (waveguide definition) transmission spectra. $\Lambda_y = 2.1\mu$m, $\Lambda_x = 1.2\mu$m, $w_{hy} = 1.7\mu$m, $w_{hx} = 0.35\mu$m, n_f=1, and d_f=0.85μm.

than λ/NA, where NA is the numerical aperture of lens system used to create the pattern and λ is the wavelength of light used to write the pattern. Of course, this assumes far-field photolithography. In the near-field, when the mask can be contacted directly with the surface, feature sizes significantly smaller than the wavelength of light used can be obtained. And, if electron beam lithography is used, then spot sizes on the order of a few nanometers are attainable.

However, in an industrial CMOS process, such as the one discussed in the next chapter, the minimum spot size is nearly the same as the minimum metal feature size for the process. So, for instance, in the CMOS process described in the next chapter, 0.9μmwas the minimum feature size for metals, and the spot size was approximately the same. Therefore, the designed rectangular slot ended up being pill-shaped. Thus, if a fabrication process is used that has a smaller minimum metal width, it will produce rectangular apertures that are cleaner the closer to ideal, given that the rectangular aperture is significantly larger than the minimum metal size in the process.

Chapter 5

Polarization-Dependent Wavelength Selective Structure Experiments

Several different types of metallo-dielectric infrared spectro-polarimetric filters were fabricated on a CMOS chip. These filters consisted of either one, two, or three-layer metallo-dielectric gratings. For the two-layer gratings, some were designed with a transverse offset between the metals of each layer in order to determine alignment resilience for metallo-dielectric spectro-polarimetric filter design. Some grating filters were designed with different pitches for each layer to study sidelobe/high-order diffraction suppression. Additionally, microwave-RADAR-inspired wavelength selective structures in one or two-layer configurations were also fabricated. In total, 39 metallo-dielectric filters were fabricated.

Most of the filters on the test chip are multi-layer metallic grating structures. The transmission spectra for those filters in both TE and TM orientation are included in the Appendix. Aside from the slotted-grid RADAR-inspired filter in one and two-layer configurations, the RADAR-inspired structures are not analyzed in the body of this thesis. The Appendix contains the transmission spectra for both TE and TM light for all the different filter types fabricated on the test chip.

5.1 Baseline Results Overview

For all of the grating-type filters, a very high TM to TE polarization extinction ratio was observed. Due to the sensitivity of the FTIR microscope used in determining the transmittance of all the samples in both TM and TE polarizations, and the overall absorbance of the chip (issues that will be discussed in this Chapter), the highest cross-polarization extinction ratio that was observed was >100:1. However, an exact number for this ratio would not be reliable with the FTIR microscope that was used. For TE polarization of incident light on the grating samples, the MCT (HgCdTe) detector in conjunction with the FTIR software was unable to lock-on to the interferogram for the FTIR. The result of this is that all TE data for the grating structures is buried under the noise floor for the entire system. This does indicate, however, that for some of the better samples an extinction ratio of >100:1 was achieved. In Figure 5-1, the transmittance spectra for both TE and TM light for a representative filter is shown. Since the transmittance was normalized to the background reflection of the ZnSe substrate, intensity transmittance can be negative.

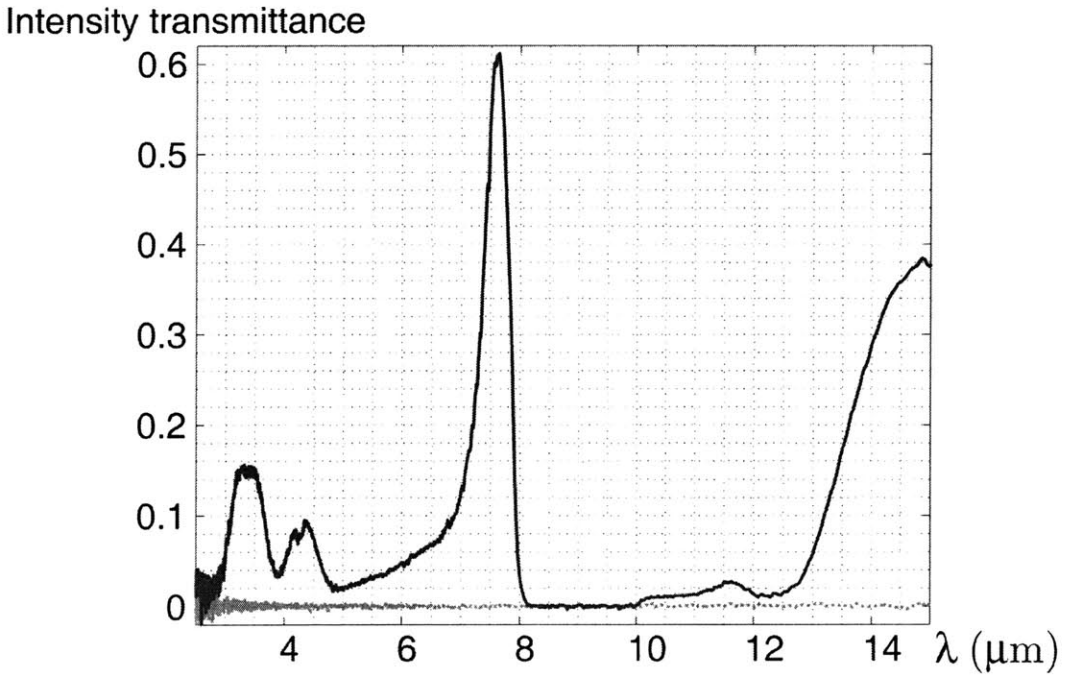

Figure 5-1: Transmission spectra for filter 5, a double-layer filter. TM transmission is shown as the solid blue line. TE transmission is displayed as the orange dotted line.

In Figure 5-2, the TM/TE transmittance ratio is calculated across all wavelengths for one of the filters with highest TM transmittance. The cross-polarization extinction ratio hovers between 50:1 and 100:1 in the LWIR. In the MWIR, it goes past 1000:1 for parts of the spectrum. Again, because we are operating near the noise floor of the FTIR (which can be seen by overall roughness of the TM/TE intensity ratio curve), this demonstrates a need for more sensitive FTIR microscope than was available for these experiments.

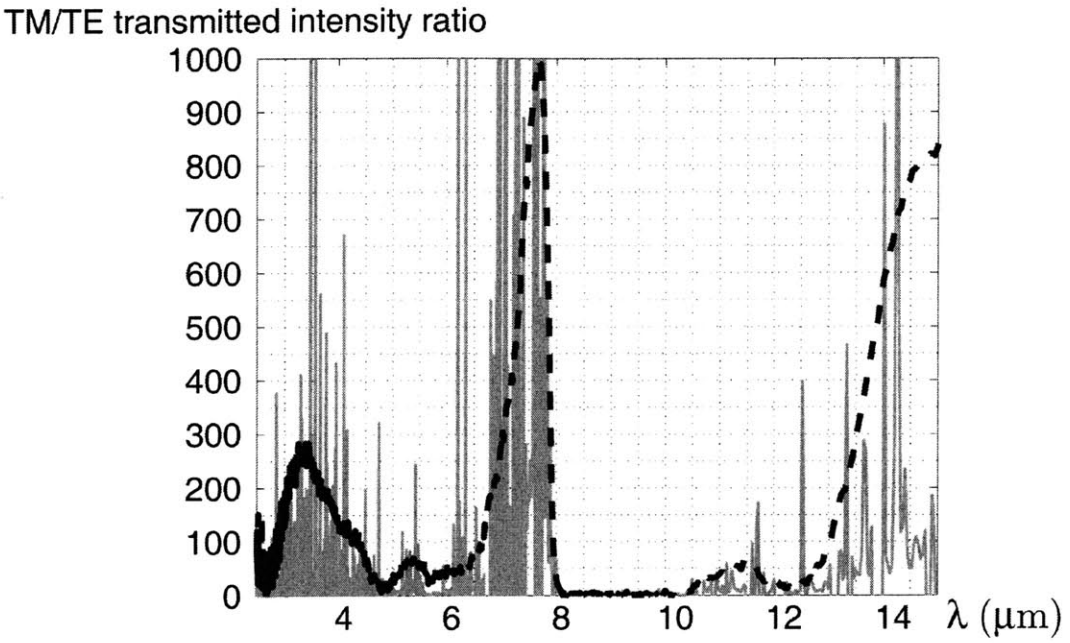

Figure 5-2: TM/TE transmitted intensity ratio (orange solid line) with two-layer (filter 13) transmittance curve overlaid (dashed blue line)

5.2 Filter Fabrication

Thirty-nine infrared metallo-dielectric wavelength-selective polarization filters were fabricated using the AMI Semiconductor mixed signal foundry service using the AMIS 0.5μm process. These filters were sized from 200μm square down to 27μm square (the approximate size of modern infrared detector array pixels). A micrograph of the chip is shown in Figure 5-3. The wire-widths, minimum grating pitch, and dielectric spacing between layers was limited by they process requirements. The only degrees

of freedom allowed in the design of these filters, by using this fabrication process, was in designing a filter that had between one to three layers and the relative pitch of each filter. All filters had to be manufactured using a rectangular grid topology and could only consist of Manhattan-type shapes (ie. wires that ran only horizontally and vertically, not diagonally).

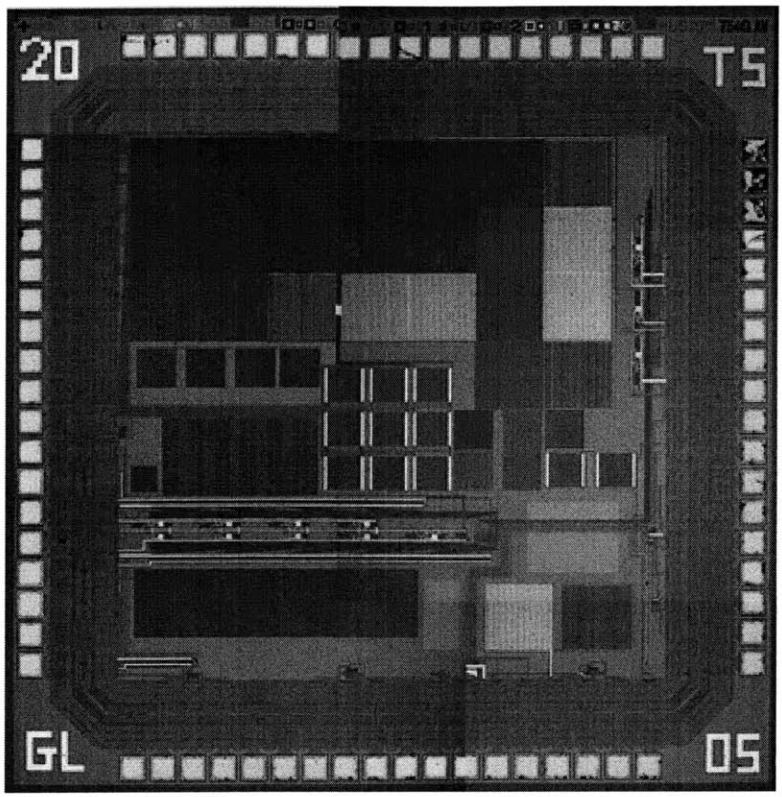

Figure 5-3: Micrograph image of the CMOS test-chip on which 39 spectro-polarimetric filters were fabricated.

A primary reason this method of initial fabrication and test was chosen, was due to cost concerns. The MOSIS foundry service allows small runs of what would otherwise be expensive mixed-signal IC chips to small businesses, colleges, and universities. To decrease the cost of fabricating a chip, the MOSIS service consolidates designs from many sources, in order to share the same silicon wafer, and therefore share the cost. Additionally, money was saved by piggy-backing on a chip that had available open space that was being produced for proof-of-concept as part of the Optoelectronic Neural Network Co-Processor project in the author's research group.

Essentially, optical filters were designed using integrated-circuit design software, to co-exist on the same silicon as a working neural-network processor component. The primary concern of the chip was to ensure that they integrated circuits performed their task, so no steps were taken by the foundry to ensure that the optical quality of the chip was maintained, other than ensuring that electrical routing did not cross over, under, or through optical filter components.

5.2.1 Process

The AMIS 0.5μm process is a standard mixed-signal semiconductor manufacturing process. The process is a three-metal-layer process with a minimum metal grating pitch of 1.8μm for layers 1 and 2 (M1, M2). The minimum metal cell size for design was 0.9μm$\times$0.9μm square for the first two layers. The third layer, M3 (top metal), had a minimum metal width of 1.5μm. Metal widths could be increased in 0.15μm increments, as long as the minimum inter-metal spacing of 0.9μm was obeyed.

The AMIS process uses either doped or un-doped silicon substrates. The choice of substrate depends on the requirements of the entire group whose chips are being fabricated on the same silicon wafer. For the run our chip was placed on, a highly p-doped silicon substrate was used. While bulk silicon is relatively transparent to infrared light, a highly p-doped silicon substrate is not.

The silicon substrate used in the manufacture of the chip has a bulk resistivity of 0.007 Ohm cm. This gives us a P concentration of 1.33×10^{19}. This level of doping is several orders of magnitude greater than necessary to make the silicon substrate transparent [103]. Therefore, to interrogate the sample with a polarized-light FTIR microscope, the substrate was removed.

5.3 Sample Preparation

The chip was fabricated on a 750μm-thick, 8-inch silicon wafer. AMIS then ground and polished the chip down to 250μm thick before each design on the same wafer was cut and distributed to the various groups that shared the same wafer.

Coming to us, the silicon substrate was approximately 250μm thick, and 4mm$\times$5mm on its sides.

Due to the high absorbance of infrared light in the p-doped Silicon substrate on which the sample filters were fabricated, it was necessary to remove the filters from the substrate. To do this, the front surface of the chip was bonded to a transparent IR window, and then the substrate was removed through a series of grinding and polishing.

5.3.1 Bonding of Sample to ZnSe Window

To grind down the silicon substrate, a suitable bonding agent to adhere the front-surface of the chip to the window material, had to be found. The window material was chosen to be ZnSe due to its ability to withstand a moist environment (such as is used while grinding/polishing), its high and relatively flat infrared transmittance across the MWIR and LWIR, and its ready availability and low cost in a small pre-polished form factor (2mm$\times$13mm) that is easily accommodated in a polishing rig.

Many forms of epoxy and other bonding agents are not transparent to the infrared, so a cyanoacrylate (super-glue) adhesive was used. Since Fourier-Transform Infrared Spectrometer (FTIR) transmittance data on cyanoacrylate glue could not be found, transmission data was recorded by sandwiching a thin film of glue between two NaCl optical flats and analyzing the transmittance spectra using a NicPlan FTIR microscope attached to a Magna 860 Thermo-Nicolet FTIR bench. The salt flats were used to test the thin glue layers because they are substantially cheaper than ZnSe, and have very high transmittance across the MWIR and LWIR. Because of their hygroscopic nature, such salt flats would not work for bonding the chip due to their natural deterioration over time due to atmospheric H_2O and due to the wet grinding and polishing environment.

Once the cyanoacrylate glue was chosen as a bonding agent, a drop was applied to the ZnSe substrate and the front surface of the chip was pressed firmly to the ZnSe until the glue dried. The glue was allowed to set for 24 hours before polishing began.

5.3.2 Grinding and Polishing of Sample

To grind and polish away the 250μm thick silicon substrate, a South Bay Technology Model 920 Lapping and Polishing Machine was used. The ZnSe substrate was attached to a micrometer-driven polishing fixture by means of carbon tape.

Initially, a 3μm grit Silicon Carbide 8" Abrasive Film disk was used on the polishing wheel. The polishing fixture was set so that approximately 200μm of material would be removed. The disk was then covered with water, and an initial water drip was started to remove sediment. The polishing fixture was placed on the polisher and adjusted so that the fixture rotated counter to the direction of the lapping wheel. The wheel speed was set so that it completed approximately two revolutions per second.

After the initial grinding stage was completed, the sample was observed to determine relative thickness. The micrometer on the polishing fixture was subsequently set to grind away 10μm of material until, under direct observation, the edge of the silicon substrate could no longer be seen with the un-aided eye.

Next, the Silicon Carbide disk was removed and replaced with an Aluminum Oxide polishing disk with 1μm grit size. The chip was then polished until chip structures were visible with a hand-held microscope in visible light. To remove the final bit of substrate and to polish the surface to optical quality, a felt disc lightly rubbed with 0.3μm aluminum oxide powder and water was used. The sample was polished until a clear and uniform reflection of visible light was obtained.

5.4 Experimental Results

Once the sample was prepared, an NicPlan FTIR microscope with internal polarizer was used to determine the polarization-dependent transmission spectra for each 200μm square filters on the chip. The FTIR component of the microscope shares an optical path with an internal visible-light microscope so that each filter could be aligned. A 100μm aperture size was used to gather a transmission spectra from each part of the chip. Spectral data was gathered from 2.5μm to 15μm. The axis of the internal polarizer were determined by rotating the entire sample in 0.5° increments

under the microscope while maintaining the center of the spot over a part of the chip with a single-layer grid, which also doubled as a polarizer, and observing the quality of the FTIR signal. With the minimized signal, data was taken on all 200μm-square structures on the chip. Then the sample was rotated 90° and samples were again taken on all 200μm square structures on the chip. For a few structures, data was also taken at other angular intervals.

The FTIR microscope has approximately a 15° acceptance angle, so at the filter, the blackbody source is not collimated. Therefore the output spectra should show spectral broadening as compared to theoretical plane-wave solutions.

5.4.1 FTIR Microscope Temporal Coherence

The coherence length of the FTIR microscope is relatively short, as is necessary for an FTIR in order to determine fine spectral transmission, absorption, and transmission characteristics of a sample under test. Though, it still has a much longer coherence length than sunlight. The FTIR uses an everglo blackbody source. This source has a temperature of 1525K, which gives an approximate coherence length of l_c=2.358μm.

5.5 Determination of Structure Values

To determine the actual structure values (metal widths, grating pitches, inter-layer dielectric spacing, metal heights) both simulation and direct measurement were used.

Since the vendor did not supply data as to dielectric layer thickness, or the metal height for the chip, this data could only be gathered through direct observation.

To determine the metal heights and dielectric layer thicknesses, the chip was cut in a transverse plane then polished. It was then viewed under a Zeiss AxioPlan microscope with a calibrated CMOS camera and measuring software. The minimum measurable increment was 0.11μm, so the error in measurement is approximately $\pm$0.055μm not accounting for error in instrument calibration.

To view the cross-section of the chip, first the chip was suspended inside a plastic holder. The holder was then filled with epoxy to stabilize and hold the chip in a ver-

tical orientation. The epoxy was allowed to dry overnight. The plastic/epoxy/chip assembly was then cut with a diamond blade so that an edge of the chip was removed up to the top line of filters (filters 25, 24, 23, 22, 21, 20, and 6 as shown in the Appendix). Using Aluminum Oxide disks, the sample was then polished down using the same SBT Polishing and Lapping machine used for grinding and polishing away the silicon substrate. This process was done by hand. After several seconds of polishing, the sample was observed in visible light to determine the progress of the grind toward the first row of filters. After several iterations, under bright-white-light illumination, the reflected grating rainbow-pattern was visible at the edge of the sample by means of a hand-held microscope and polishing was stopped.

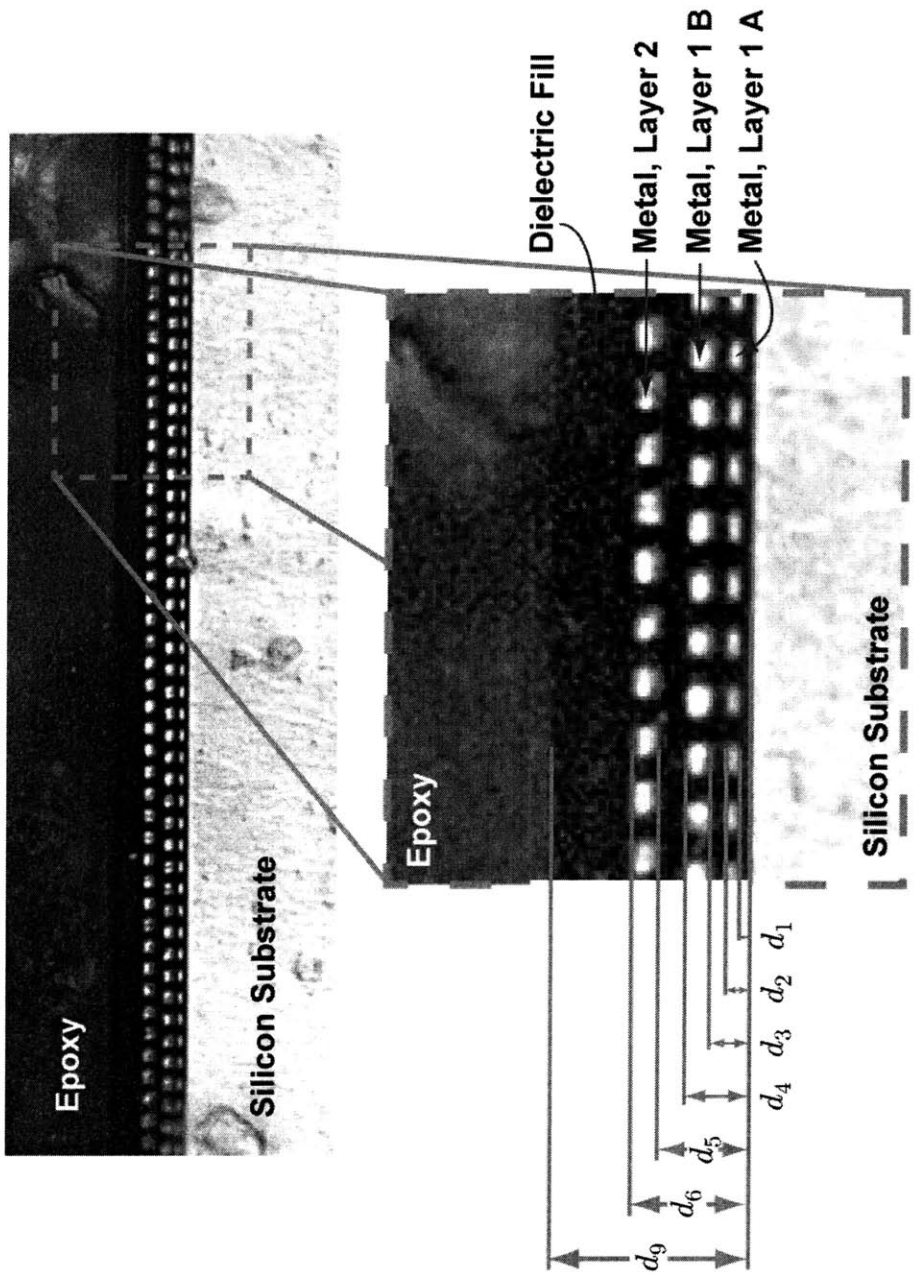

Figure 5-4: Cross section image of two-layer metal grating structure with each layer having a 1.8μm grating pitch. The top layer is offset by the bottom layer by 0.6μm, and is cross-sectional image of filter 20 on the chip.

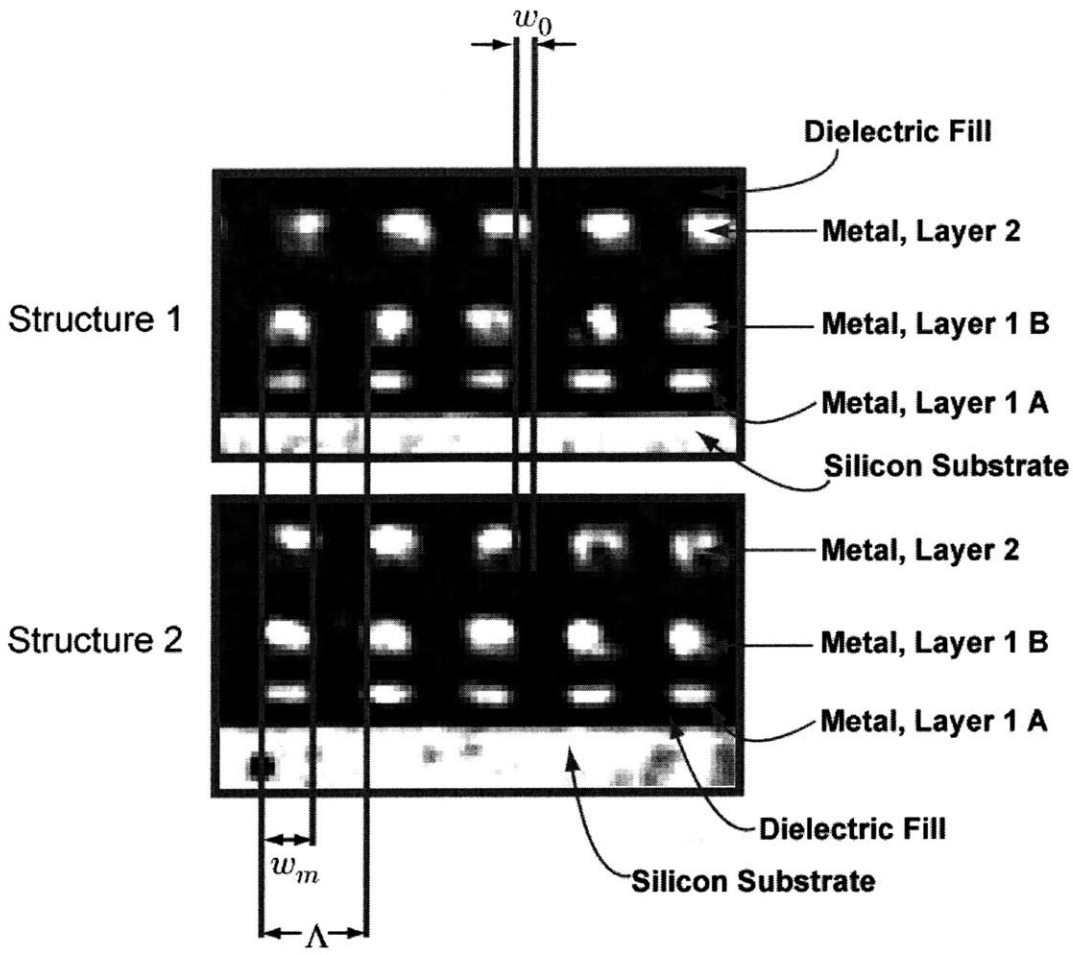

Figure 5-5: Two 2-layer structures in transverse cross-section. Structure 2 (bottom): filter 23 with a relative shift, w_0 of 0.15μm from the bottom row. Structure 1 (top): filter 21 with a relative shift, w_0 of 0.45μm. Λ is the grating pitch of 1.8μm. w_m is the metal width of 0.9μm.

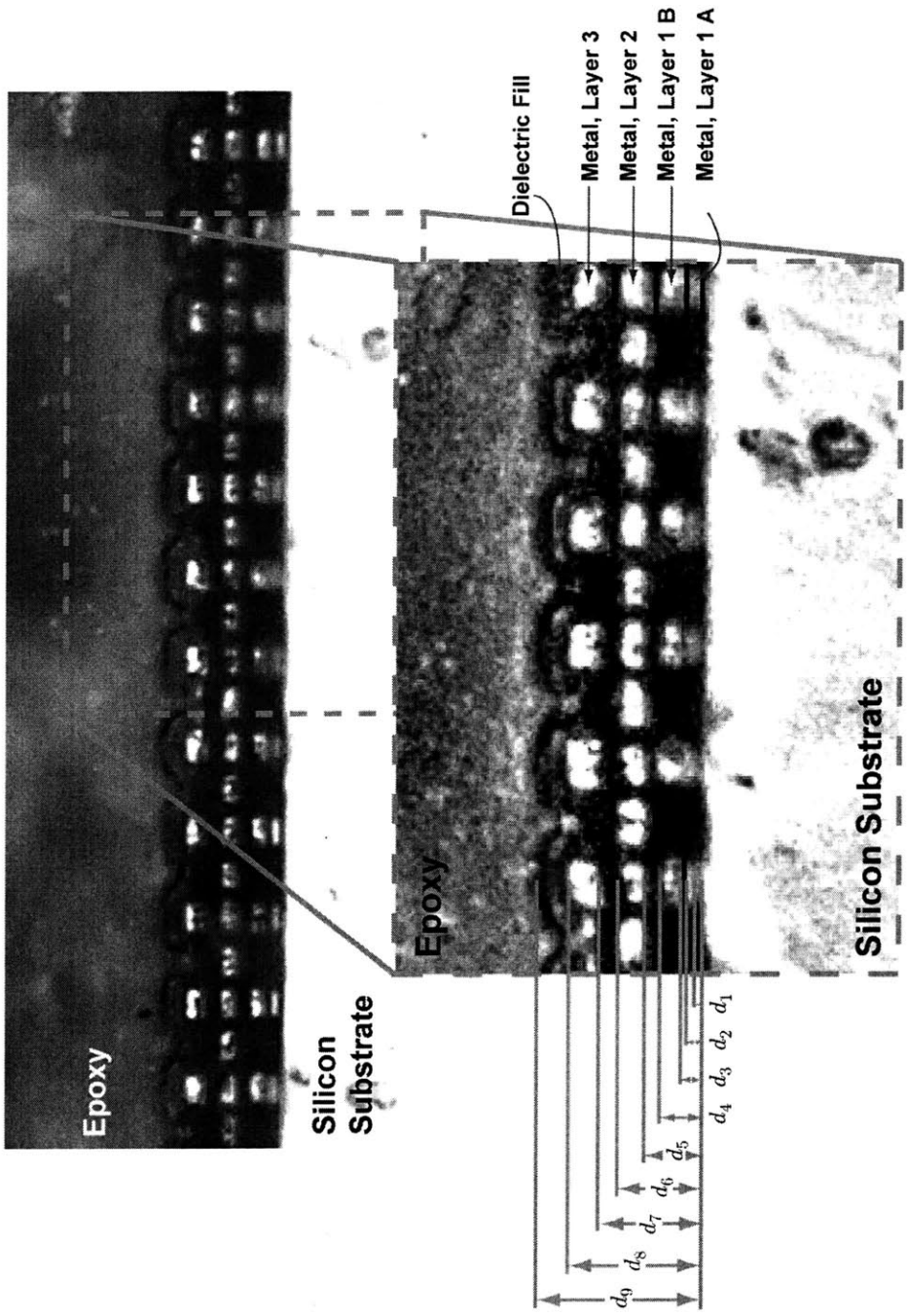

Figure 5-6: Cross section image of filter 6. This filter has a 2.4μm-pitch middle grating with 4.8μm-pitch bottom and top gratings.

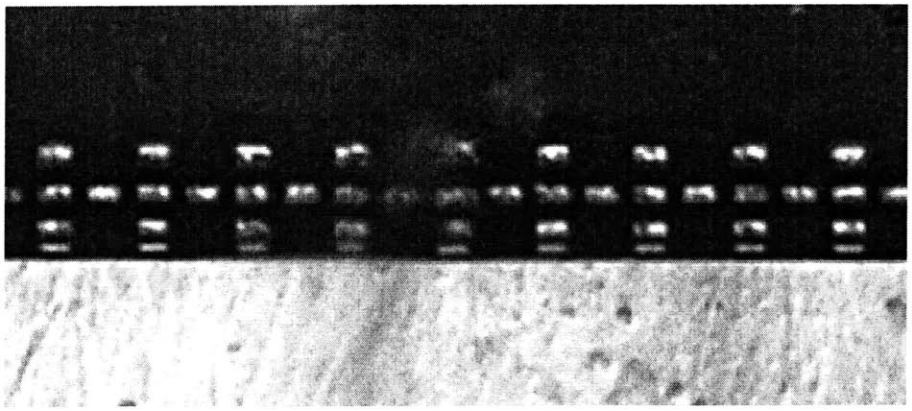

Figure 5-7: Triple layer structure with 2.4μm pitch in the middle layer. Top and bottom layers are double the center pitch, at 4.8μm. For RADAR structures, this type of multi-layer grating is used for sidelobe suppression.

5.5.1 Measured Layer Thicknesses

Figures 5-4, 5-5, 5-6, and 5-7 have been contrast-enhanced to better show the transverse structure of the filters. The reader will immediately note that the "two-layer" structure is in fact a three-layer structure, with the first metal layer (M1) consisting of not one, but two metals of differing thickness but identical widths. For the purpose of analysis, since Layer 1 A always appears with Layer 1 B they will be talked about as just M1 or Layer 1. This additional layer is most likely silicide, and it is present on all structures with metal in Layer 1. It's presence is required to ensure density requirements for the manufacture process.

In both Figures 5-4 and 5-6, the spacing nomenclature remains the same. The top-most layer in each image is the epoxy background in which the chip was suspended for the purpose of polishing and cutting. The bottom-most layer is the silicon substrate on which the chip was fabricated. The distance d_1 is the distance from the substrate to the first metal of Layer 1. $d_2 - d_1$ is the height of Layer 1A. $d_3 - d_2$ is the height of dielectric between the metal of Layer 1 A and Layer 1 B. $d_4 - d_3$ is the height of metal Layer 1 B. $d_5 - d_4$ is the dielectric thickness between the Layer 1 metal and Layer 2 metal. $d_6 - d_5$ is the metal thickness of the Layer 2 metal. For the case of the two-layer filter in figure 5-4, $d_9 - d_6$ is the height of the dielectric cap on top of

the Layer 2 metal.

For the three-metal-layer system, the nomenclature remains the same, but there are the additional values, including: $d_7 - d_6$, the dielectric fill height between the metals of Layer 2 and Layer 3, and $d_8 - d_7$ the height of metal Layer 3. $d_9 - d_8$ in this case is the height of the nitride/oxide passivation layer dielectric. Below is a table of the microscope-measured range of values, and the values used for structure simulation:

Three-Layer Measurement	Value	Two-Layer Measurement	Value
$d_1 - d_0$	0.32μm	$d_1 - d_0$	0.32μm
$d_2 - d_1$	0.32μm-0.42μm	$d_2 - d_1$	0.32μm-0.42μm
$d_3 - d_2$	0.32μm	$d_3 - d_2$	0.32μm
$d_4 - d_3$	0.74μm-0.85μm	$d_4 - d_3$	0.74μm-0.85μm
$d_5 - d_4$	0.95μm-1.06μm	$d_5 - d_4$	0.95μm-1.06μm
$d_6 - d_5$	0.74μm-0.85μm	$d_6 - d_5$	0.74μm-0.85μm
$d_7 - d_6$	0.95μm-1.06μm	$d_9 - d_6$	2.75μm
$d_8 - d_7$	0.85μm-0.95μm		
$d_9 - d_8$	1.69μm		

The only vendor-supplied data about the height profile of the chip, was that there is a 1μm nitride and 0.7μm oxide passivation layer on top of the chip. This correlates well with the $d_9 - d_8$ measured height of 1.69μm.

5.5.2 Spectral Features

On all of the intensity transmittance plots found in the Appendix, the transmitted intensity for both TE and TM light is nearly zero from $\lambda \approx 8\mu$m to $\lambda \approx 10\mu$m with no recognizable transmittance centered about λ=9μm. This uniform nulling of the transmitted infrared light across all filters and even on spaces of the chip with only dielectric is attributed to oxide absorbance [104].

It is only over the waveband of 3μm to 8μm where the filters exhibit interesting behavior, and thus it is over this range that the results are analyzed and simulated.

5.5.3 Dielectric-Only Data and Simulation

Three sections of the chip were selected for the purpose of simulation and verification of device properties. The first of these was an open-space section on the chip. An area was chosen, on the chip, such that no intervening wire or metal layers would obscure the optical field. Transmittance data was then acquired using the NicPlan FTIR, and is shown in Figure 5-8.

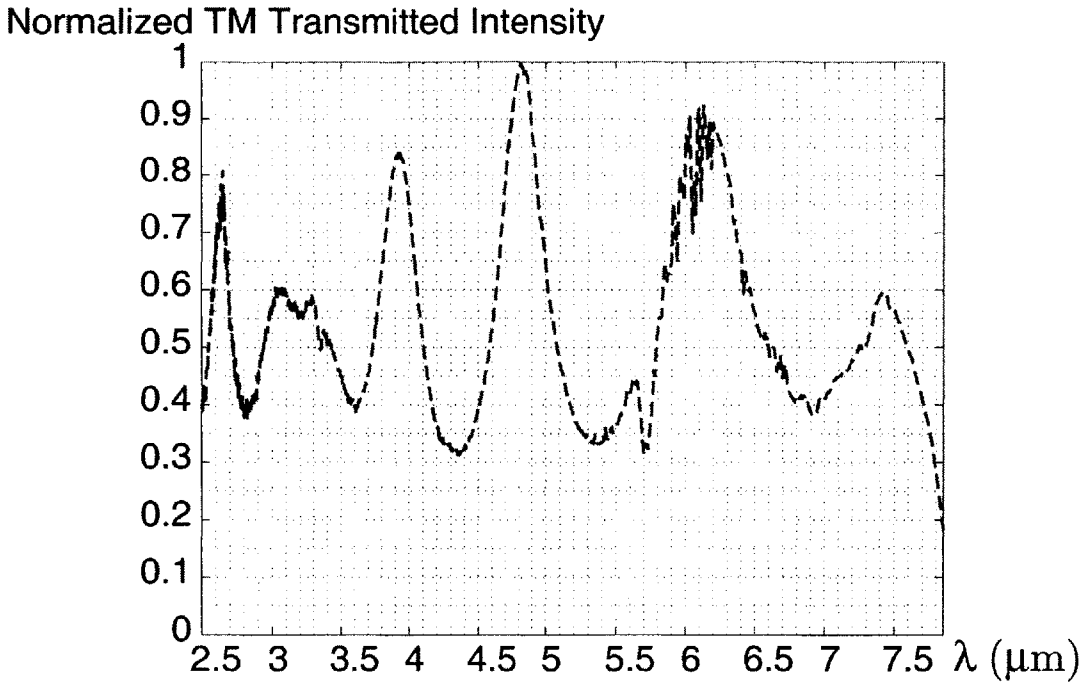

Figure 5-8: Transmission spectra of an open-area (dielectric only) portion of the test chip

To determine the equivalent height and refractive index value for a single dielectric layer, which appears to contribute most to sinusoidal ringing as seen in Figure 5-8, a least-squares method was used.

The wavelength location for the heights of the transmission peaks for the FTIR data was determined with a smoothing filter and followed by direct determination of the location of localized maxima.

The single-layer etalon peaks should have maxima when

$$d = \frac{\lambda_n}{2} \cdot (m + n) \tag{5.1}$$

where d is the dielectric height, λ_n is the wavelength at which a peak forms (of order $m + n$), m is the lowest order of constructive interference in the field-of-view, and n has the integer values 0, 1, 2, 3, etc. such that $m + n$ is the order of interference for each peak seen in Figure 5-8.

Equation 5.1 can be re-written as,

$$2d\lambda_n^{-1} - m = n \tag{5.2}$$

.

Letting the variables $x_1 = d$ and $x_2 = m$, we can write the system of equations as

$$\begin{bmatrix} 2\lambda_0^{-1} - 1 \\ 2\lambda_1^{-1} - 1 \\ 2\lambda_2^{-1} - 1 \\ 2\lambda_3^{-1} - 1 \\ \vdots \\ 2\lambda_n^{-1} - 1 \end{bmatrix} \begin{bmatrix} x_1 \\ x_2 \end{bmatrix} = \begin{bmatrix} 0 \\ 1 \\ 2 \\ 3 \\ \vdots \\ n \end{bmatrix} \tag{5.3}$$

To determine the value of x_1 and x_2 for this over-determined system of the form $\mathbf{Ax} = \mathbf{b}$, where bold represents matrix components, we need to formulate an optimized least squares solution of $\mathbf{x} = \mathbf{A}^+\mathbf{b}$, where $\mathbf{A}^+$ is the pseudo-inverse of $\mathbf{A}$ and is defined as $\mathbf{A}^+ = (\mathbf{A}^\mathrm{T}\mathbf{A})^{-1}\mathbf{A}^\mathrm{T}$. That is, $\mathbf{A}\mathbf{A}^+ - I_n$ is minimized, where I_n is the identity matrix.

From this, we get that the effective dielectric height is approximately $9.25/n$ microns, where n is the dielectric index of refraction for the layer. To determine the effective index of the effective single-layer, surrounded by a free-space vacuum, the minima of the theoretical and actual curves were matched along with their FWHM slope. For a simulated case of $n = 3.8$, the results are shown in Figure 5-9.

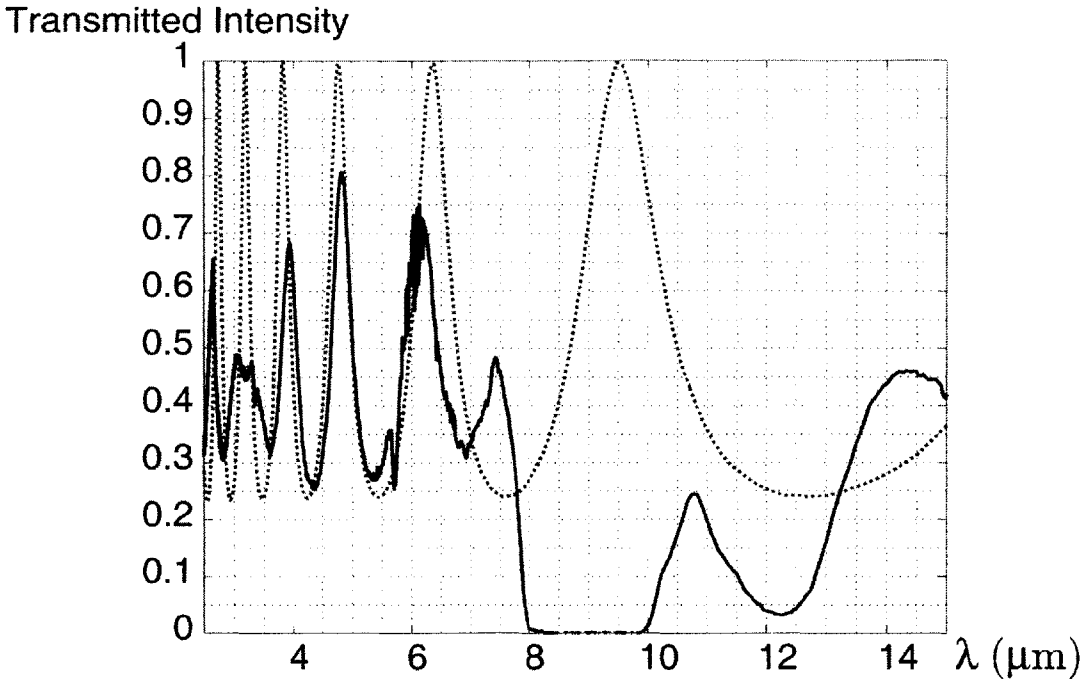

Figure 5-9: Experimentally-measured transmission spectra (solid blue line) in an open space on the sample overlayed with theoretical transmission curve (dotted red line) results.

In Figure 5-9, the blue solid line is the experimental data taken from an open space on the chip using the NicPlan FTIR. The dashed red line is the simulated result using a least-squares method to determine device parameters. In the figure, the large SiO absorbance band can be seen between 8μm and 10μm. Due to this absorbance, no theoretical data is compared with experimental data above 8μm. The effective dielectric layer that contributes to the ringing seen in Figure 5-9 comes from a thin layer of silicon substrate that remained after polishing of the chip.

For a refractive index of $n = 3.43$, a representative refractive index for amorphous silicon in the MWIR, the dielectric stack height would be 2.70μm.

5.5.4 Double-Layer Metal Grating Data and Simulation

A double layer grating as also tested and simulated. However, due to the apparent de-coupling of the dielectric Fabry-Perot effects from the resonant effects of the metallic grating, the metallic grating was simulated as a free-space structure, scaled appropriately due to the effective optical path length differences due to surrounding

dielectric.

Double Layer Grating

Due to the low coherence of the FTIR source, simulation of the three-layer structures does not correlate well with data taken from the corresponding three-layer structures on the chip. Since structures that are significantly separated (with respect to the coherence length of the source) from each other are not coherently coupled, FDTD methods are not well-suited for their modeling. Additionally, since the transmission curves for single layer structures depend highly on the surrounding dielectric layers (for which manufacturer data was not provided), more data as to specific inter-layer dielectric thicknesses and materials would have been required to achieve good correlation between experiment and data. Because of the strong two-layer resonances between metals of adjacent layers, only two-layer metallic grating structures had acceptable correlation between experiment and their corresponding theoretical model. Within regions of coherent coupling, FDTD can be used to indicate overall patterns in the transmittance spectra.

Figure 5-10, presents the simulated and normalized TM transmittance spectra (dotted red line) from λ=2.5μm to λ=8μm for a two-layer metal grating filter.

The important correlations between experiment and theory for the two-layer structure are: (1) the killing of the peak found in Figure 5-8 at λ=6.26μm (caused by the band-stop of the two-layer structure), (2) the transmission peak between λ=3μm and λ=5μm, and (3) the transmission peak near 7μm.

In Figure 5-10, we see good correlation with the simulated transmission spectra and the actual transmission spectra. However, there is substantial broadening of the actual curve near λ=8μm in the experimental data that is not observed in the simulated data. This can be attributed to two factors: (1) the simulation assumes plane-wave excitation, while in fact the FTIR illuminates the chip at a relatively wide range of angles, as discussed earlier, and (2) the simulation assumes a perfectly rectangular conductor as the grating element. In practice, due to finite spot size in the grating-creation process, and the chemistry involved in fabrication, the metals

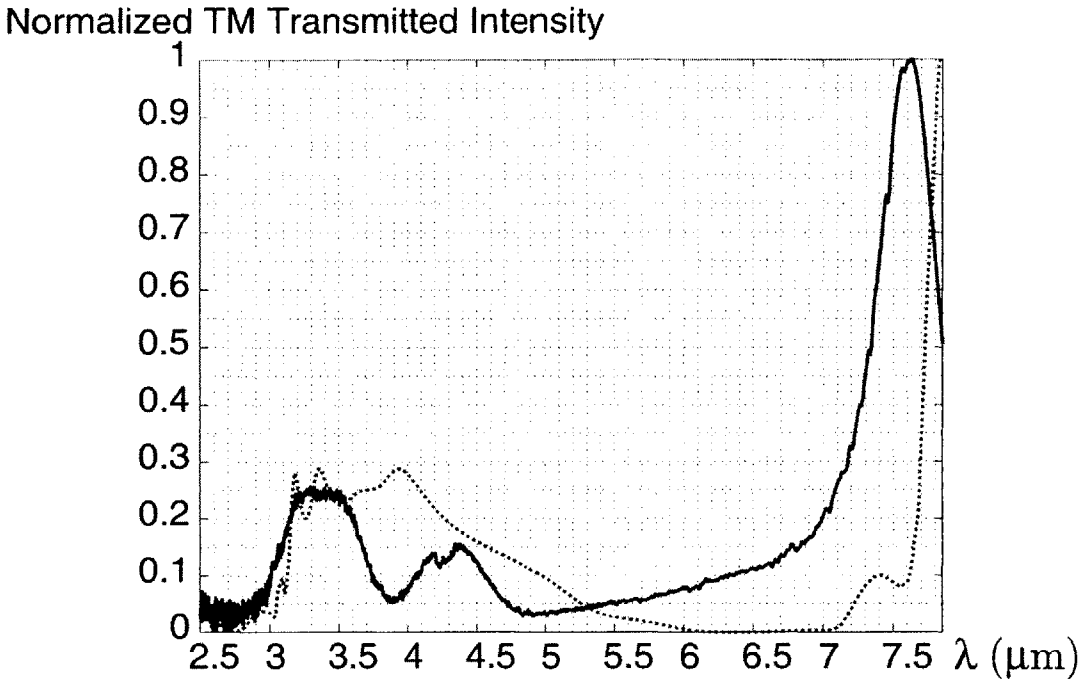

Figure 5-10: Experimental TM transmitted intensity for a single-layer metallic grating (solid blue line), plotted against the simulated single-layer TM transmittance curve (dotted red line).

used in this process are neither perfectly flat nor are the corners perfectly sharp.

Additionally, the transmission peaks for the experimental data between 3μm and 5μm do not follow the theoretical curve precisely. Again, the simulation assumed coherent de-coupling between other resonant structures in the same optical path. So, while the envelope of the transmission curve is governed by the two-layer metallic grating pass-band, there is still a background dielectric resonance caused by the substrate, as seen in Figure 5-8 that leads to this ringing.

5.5.5 Slotted Grid Data and Simulation

One other structure on the chip was analyzed and simulated, and besides the one and two-layer metallic grating filters, it presents the third best possibility for wavelength-depended polarization filtering. Both the single and double-layer slotted grid structures were simulated and compared with TM-polarized FTIR transmittance data.

In Figure 5-11, the blue solid line is the FTIR-measured TM-transmitted light for a single layer slotted-grid filter. The dotted red line is the simulated single layer

structure with height and width profiles measured by the Axioplan microscope while looking at cross-sectional images of the two-layer grating structure.

Good correlation between theory and experiment, at least above λ=4μm is readily seen in both Figures. The single-layer slotted-grid was modeled as a rectangle with rounded corners, a pill-shaped filter. Due to the finite spot size used to create the metallic structures, corners were not flat. However, due to computational limitations, the pill-shaped profile of the slotted grid had to be roughly approximated. With better approximation, the more accurate higher frequencies (smaller wavelengths) can be simulated. Thus, one would expect weaker model-to-data correlation at smaller wavelengths where fine structural details become more important.

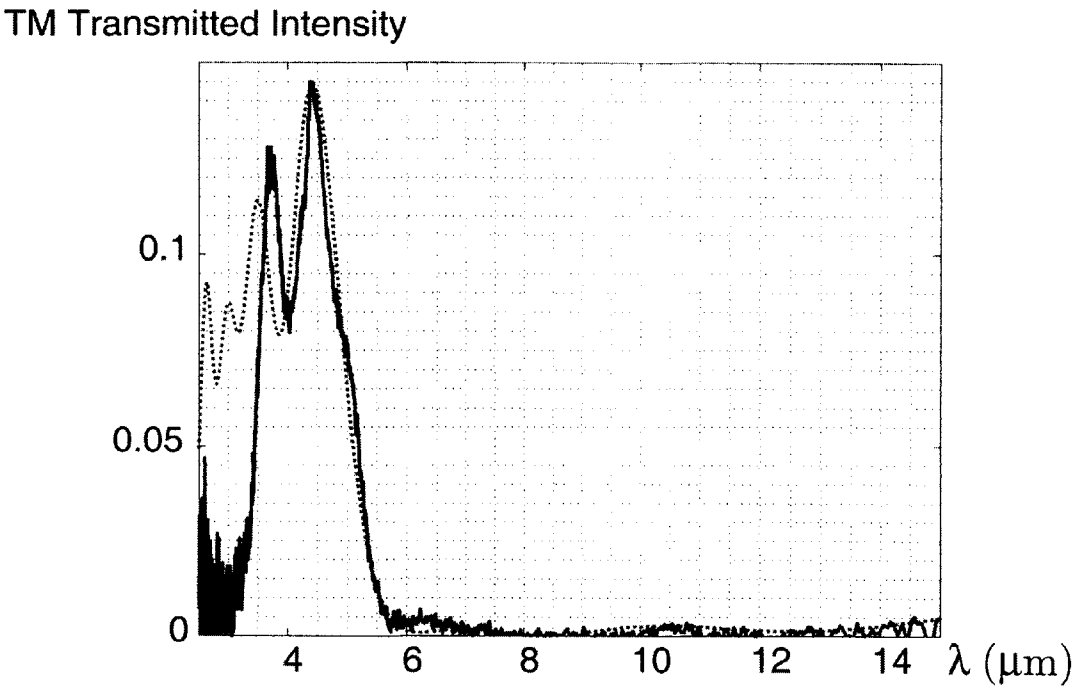

Figure 5-11: TM transmission curve of experimental (solid blue line) and simulated (dotted red line) single-layer slotted metallic grid .

In Figure 5-12, the blue solid line is the FTIR-measured TM-transmitted light for a two-metal-layer slotted-grid filter. The dotted red line is the calculated transmission profile for the structure. Like we see with the single-layer case, the double-layer case also has good correlation between theory and experiment, at least for wavelengths longer than λ=3.5μm. Similarly for this case, due to the rather course grid size

required due to computational limitations for a three-dimensional FDTD simulation, shorter wavelength results are not as accurately represented by the theoretical model.

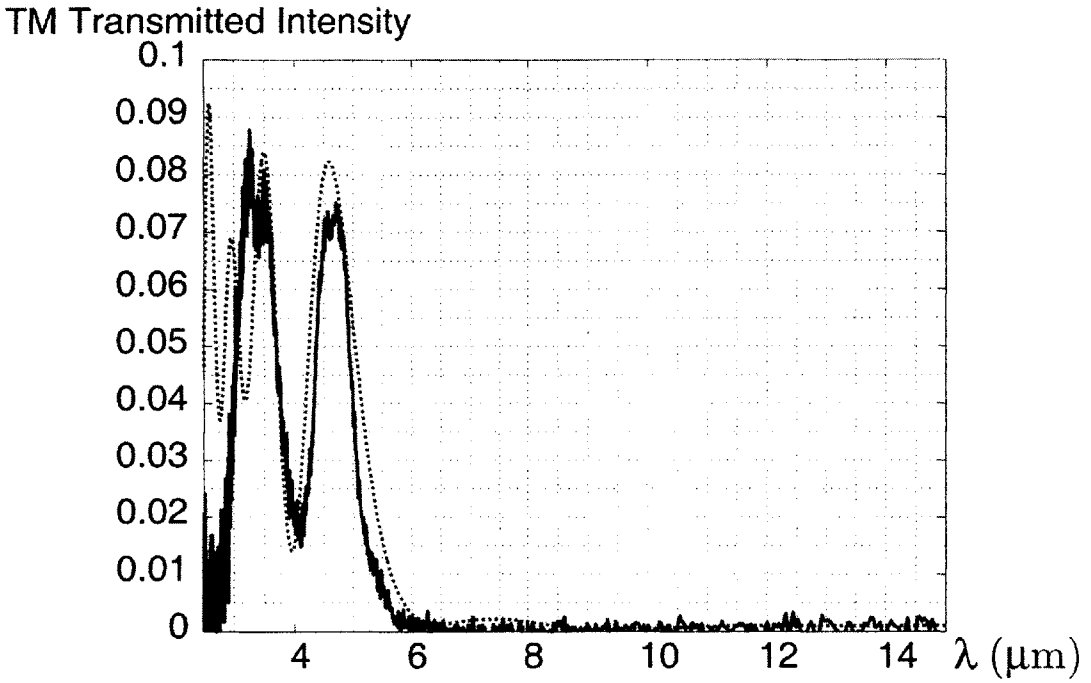

Figure 5-12: TM transmission curve of experimental (solid blue line) and simulated (dotted red line) double-layer slotted metallic grid.

5.6 Lessons Learned from CMOS-Chip Experiment

The first lesson learned was the need to use a intrinsic bulk silicon wafer for fabrication. While in this experiment, the doped silicon substrate was removed with mechanical means, scratches and imperfections did form, especially for a very thin layer of silicon. Also, using glue to bond a new optical substrate to the chip adds for an additional layer of complexity (and corresponding absorption, scattering, and reflectance). Ideally, for future use of CMOS technology for the fabrication of infrared filters, bulk silicon, which is relatively transparent in the infrared, should be used.

As shown in the micrograph side-views of the chip, there is an unexpected fourth layer of metal. This layer was neither reported by the manufacturer nor was it part of the design submitted to the manufacturer. For future design, we need to get

assurances from the fabricator that only the layers we design will be present. And, if that is not possible, we will need to make sure the first layer (the double layer) is not utilized in designs.

The chip has an oxide / nitride top layer. If the top layer of metal was not used, there would not be a need for this layer (which protects the top metal against corrosion, etc.). Having this layer adds resonance effects that are undesirable. To remove this layer post-manufacture requires a significant amount of work. It is preferable to not include this layer, and to instead top the last metal layer with silicon and then chemo-mechanically polish the entire structure flat.

It would also be beneficial to have a little more control over the heights of each dielectric layer as well as each metal layer. For proof of concept, it is acceptable to let one of the possible degrees-of-freedom be set by processing demands, while still allowing for adjustment of all the others design parameters. However, because we shared the fabrication run with numerous other groups, whose purpose was to build useable semiconductor chips, we did not have adequate freedom to fabricate a filter according to the design criteria set forth in the previous chapter.

However, by fabricating this chip, it was shown that the dielectric and metal models used in the previous chapter can approximate the performance of the experimental chip. Also, methods were developed to prepare a future CMOS chip for FTIR interrogation.

Chapter 6

Conclusions

This work is a direct continuation of the work performed by Kim for his doctoral research [34]. The multispectral filtering structure designed by Kim used separate spectral and polarization filtering components. Kim suggested, but did not resolve, methods to fabricate the spectral and polarization filters on the same substrate. No work was done toward integrating the mosaicked multi-spectral polarimetric filtering technology to a detector technology. The work presented in this thesis expanded upon Kim's work on RADAR-type structures and coupled metallo-dielectric structures. Several advantages of the metallo-dielectric spectro-polarimetric filter over traditional spectral and polarization filter designs were also presented.

6.1 Results Summary

Before this thesis, the application space was under-explored. The first chapter of this thesis includes numerous possible applications for an inexpensive, rugged, multispectral polarimetric imaging technology. The first step in addressing this need, is the development of low-cost, robust, rugged filter technologies that can be integrated with other emerging technologies, such as uncooled microbolometer arrays, adaptive optics, low-energy machine processing, etc.

A collection of spectral and polarization signatures of interest were also presented in order to motivate and narrow the design criteria for an MWIR or LWIR multispec-

tral polarimetric imaging sensor.

Several single and double-layer metallo-dielectric spectro-polarimetric filters were designed and simulated. These structures have the benefit of combining spectral and polarization filtering into the same structure. These metallic grating structures utilize the Rayleigh anomaly (an anomaly of horizontal resonance in a grating structure) and waveguide Fabry-Perot-like modes to create filters with fabrication-tunable pass-bands.

The single-layer metallic-grating structures with dielectric fill allows for wavelength tunability in manufacture by varying its height and pitch. Additional tuning is also possible by coupling to an external cavity, such as is found in modern microbolometer technology.

The double-layer metallic-grating structure with dielectric fill allows for wavelength tunability in manufacture by varying the width of each metal. This has manufacturing advantages, since all metal and dielectric layers are of the same height, and only the transverse grating pattern changes.

Slotted grids are also proposed as wavelength-selective polarization-selective filtering devices for IR imaging. By adjusting only the transverse dimensions of a two-dimensional rectangular aperture grating, wavelength tunability in manufacture is demonstrated.

A CMOS chip was designed and fabricated for the purposes of comparing simulation with experiment and to better understand possible CMOS design failure modes for multispectral polarimetric filter fabrication. The metallo-dielectric filters designed for this chip allowed us to perform a preliminary study of the feasibility of using CMOS technology in the fabrication of infrared filters. While the CMOS process does allow for spectro-polarimetric filter construction, optimal optical filter design must allow for control over all design parameters. Using the AMIS 0.5μm process over-constrained the design of the said multispectral polarimetric filters. However, analysis of the chip did demonstrate partial feasibility of using a CMOS process for spectro-polarimetric filter design in the future.

6.2 Future Work

The next step for this research project is the fabrication of single and double layer metallic grating structures as well as perforated grid structures under more controlled conditions than were available using the MOSIS/AMIS process. This will provide additional proof of concept, and hopefully useable filters that can be incorporated into an imaging system. Beyond that, direct integration and test with a full-size IR detector array is suggested. This will likely require close collaboration with a detector manufacturer, as the filter designs are most efficient if incorporated directly into the detector design process.

Appendix A

CMOS IR Filter Test Data

A.1 Chip Layout and Visible Light Transmission and Reflection Micrographs

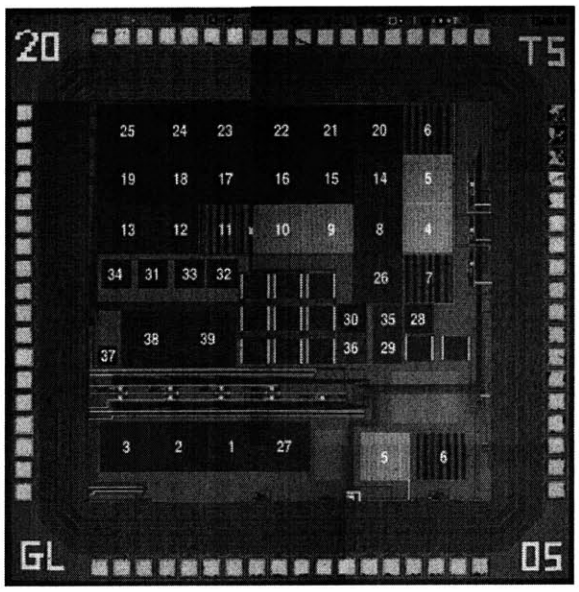

Figure A-1: CMOS chip micrograph with 39 spectro-polarimetric filters. Numbers derived from those submitted in chip fabrication. Image constructed from a mosaic of pictures taken by Axioplan white-light microscope with top illumination.

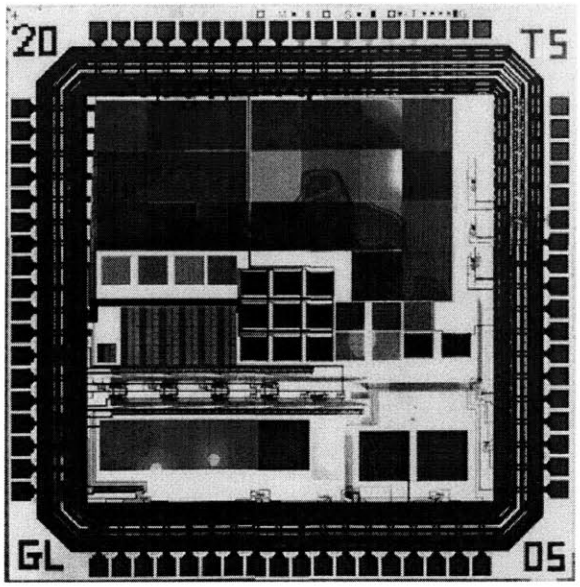

Figure A-2: Thinned CMOS chip on ZnSe substrate. Image constructed from a mosaic of pictures taken by Axioplan with white-light illumination from below.

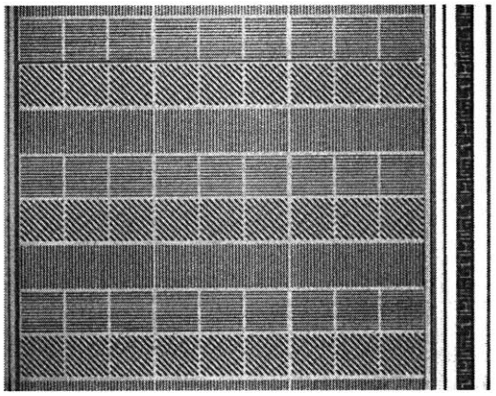

Figure A-3: Three 3x3 cells of wire gratings. Each polarizer of the small wire gratings is 27.6μmsquare. The metal gratings are sized to fit over in a modern IR imaging array.

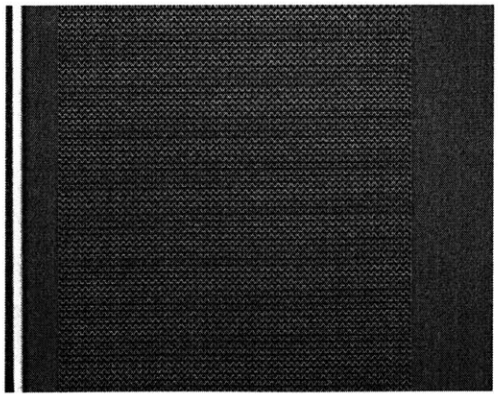

Figure A-4: Micrograph of RADAR-type design Meanderline Polarizer circular-polarization filter.

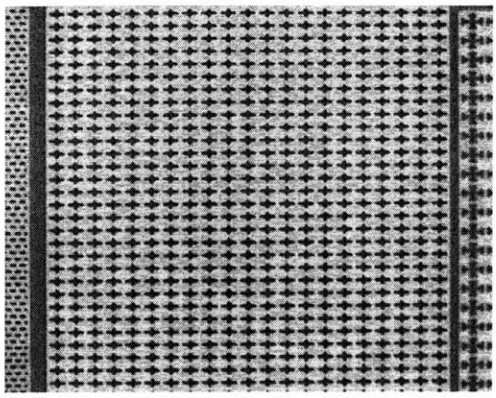

Figure A-5: Micrograph of 100μmsquare array of cross-type filters.

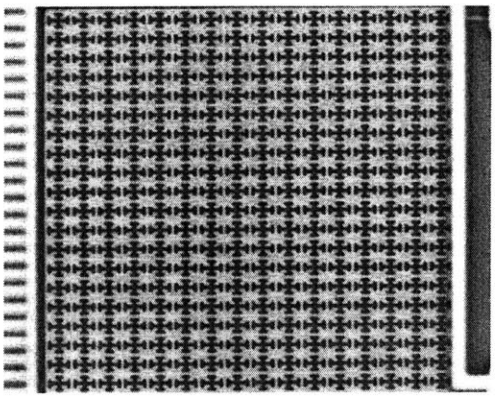

Figure A-6: Micrograph of 100μmsquare array of Cross-Potent filters (sometimes referred to in RADAR design as a Jerusalem-Cross filters

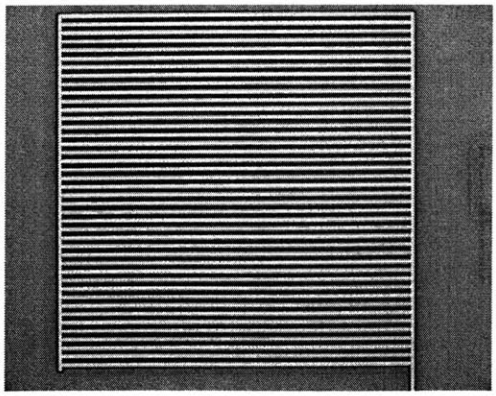

Figure A-7: Micrograph of 100μmsquare filter with 4.8μmpitch

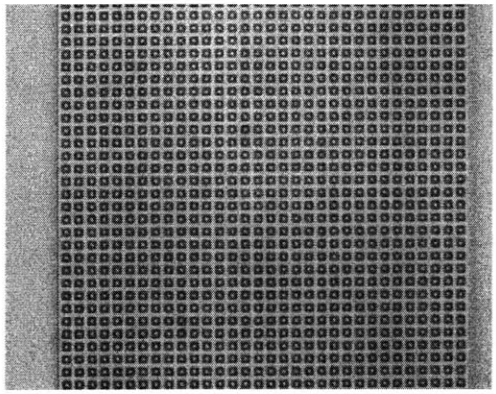

Figure A-8: Micrograph of 100μmsquare filter with eyeball-type filters (often called a square-loop filter in RADAR design).

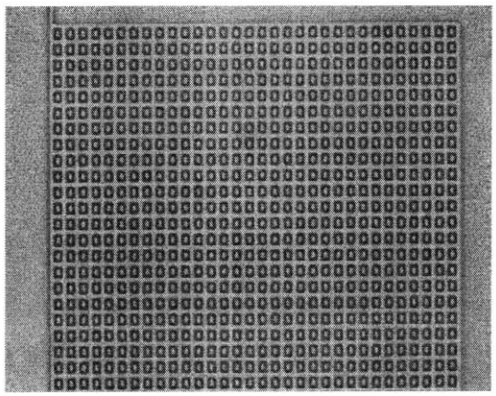

Figure A-9: Micrograph of a 100μmsquare filter with elongated eyeball-type filters (often called a rectangular-loop filter in RADAR design)

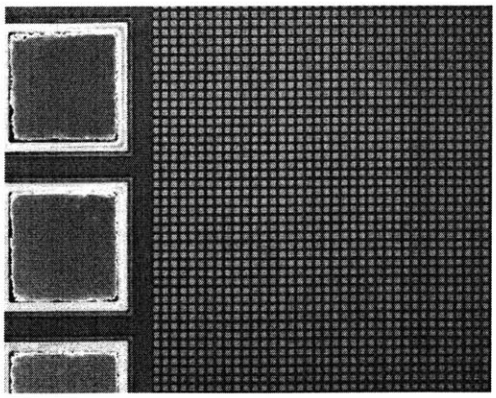

Figure A-10: Micrograph of an area outside of the chip. Effectively, this are acts as a plate-type filter.

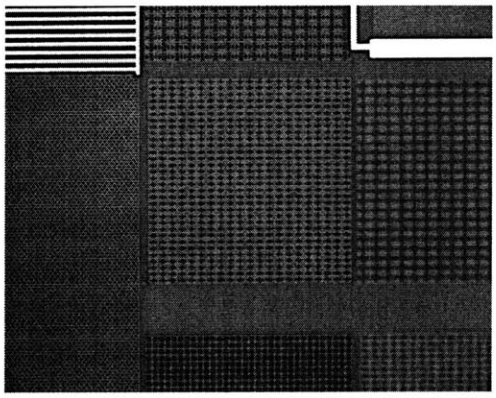

Figure A-11: Micrograph of a location on the chip with several RADAR-type structures.

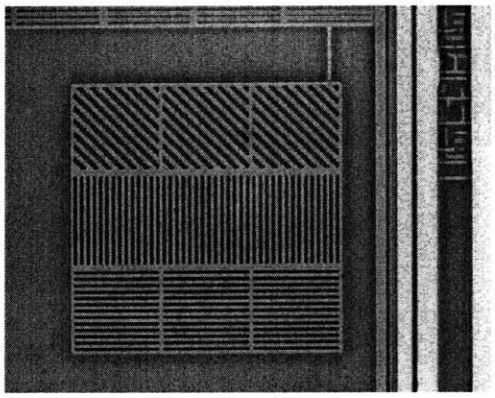

Figure A-12: Micrograph of 100μmsquare filter, with a 3x3 array of polarization subfilters.

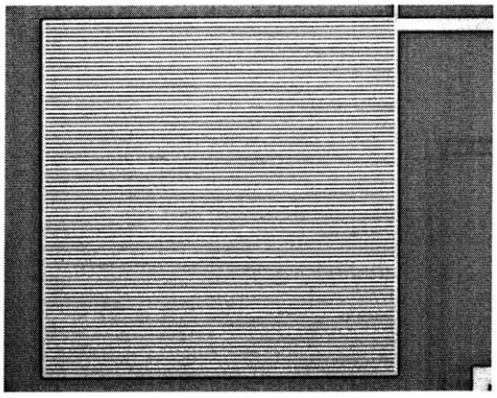

Figure A-13: Micrograph of a 200μmsquare metallic grating with Λ=2.4μm,

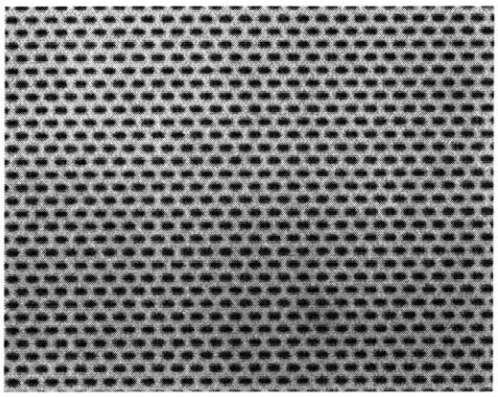

Figure A-14: Slotted grid two-dimensional grating structure. Notice the pill-shape of the individual grating elements. Holes (green) are approximately 0.9μmby 1.8μm.

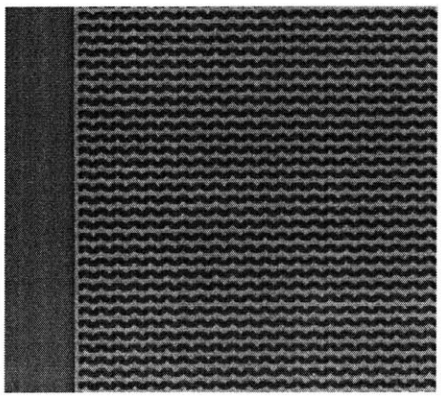

Figure A-15: Magnetic meanderline grating structure for filtering circularly polarized light.

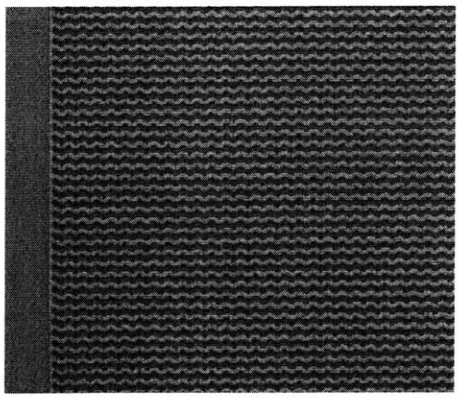

Figure A-16: Meanderline grating structure used for filtering circularly polarized light.

A.2 Single and Multilayer Wire Grid Filters

In the following section are experimental transmission results taken for each of the metallo-dielectric filtering structures fabricated on the chip. All data was taken with a NicPlan FTIR microscope with a HgCdTe detector. An infrared polarizer was placed in the beam path, in order to interrogate the structures with polarized light. For each of the structures TM light (top curve, in red) and TE light (bottom curve in blue) results are presented. The spectrum analyzed was from a wavelength of 2.5μm to 15μm.

A.2.1 Single Grating, 1.8μm Pitch (Layer 1 - Minimum Spacing)

(Filter 25, Name: polarizer1)

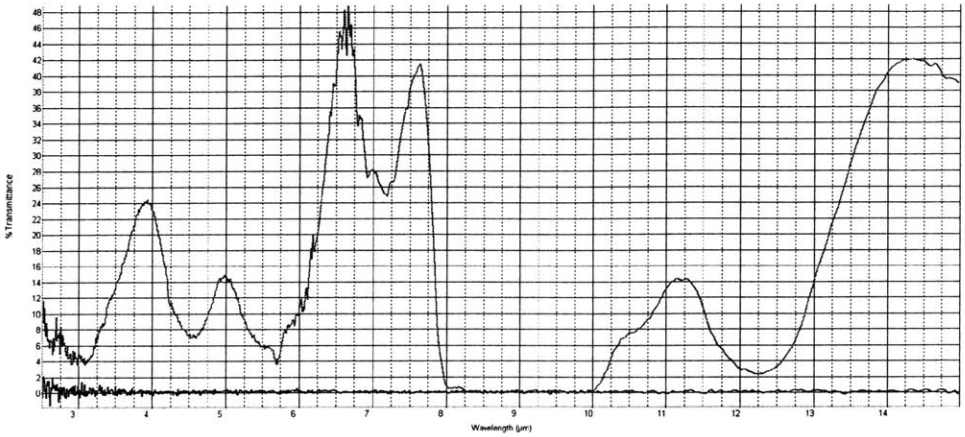

Figure A-17: Single grating, 1.8μm pitch (layer 1 - minimum spacing) TM (red) and TE (blue) intensity transmittance vs. wavelength.

A.2.2 Single Grating, 1.8μm Pitch (Layer 2 - Minimum Spacing)

(Filter 16, Name: polarizer1_layer2)

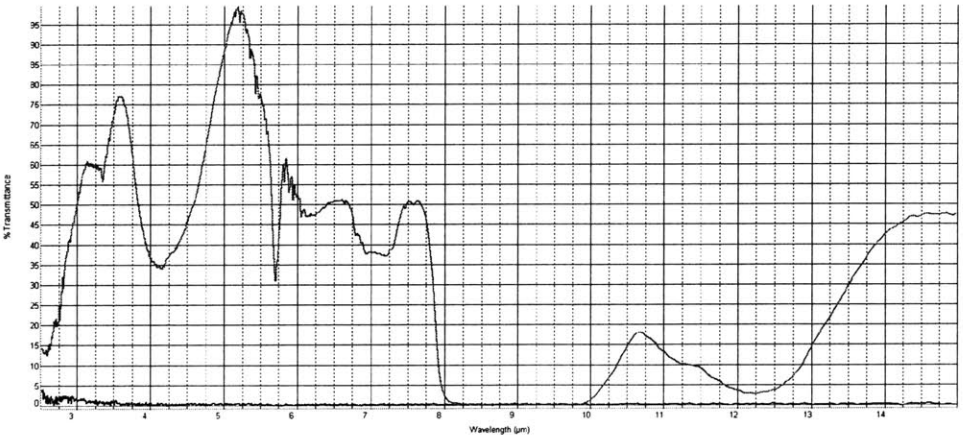

Figure A-18: Single grating, 1.8μm pitch (layer 2 - minimum spacing) TM (red) and TE (blue) intensity transmittance vs. wavelength.

A.2.3 Two-Layer Grating (Layer 2 - Minimum Spacing, 1.8μm Pitch ; Layer 1 - Double Pitch)

(Filter 15, Name: polarizer1_layer2_dp1)

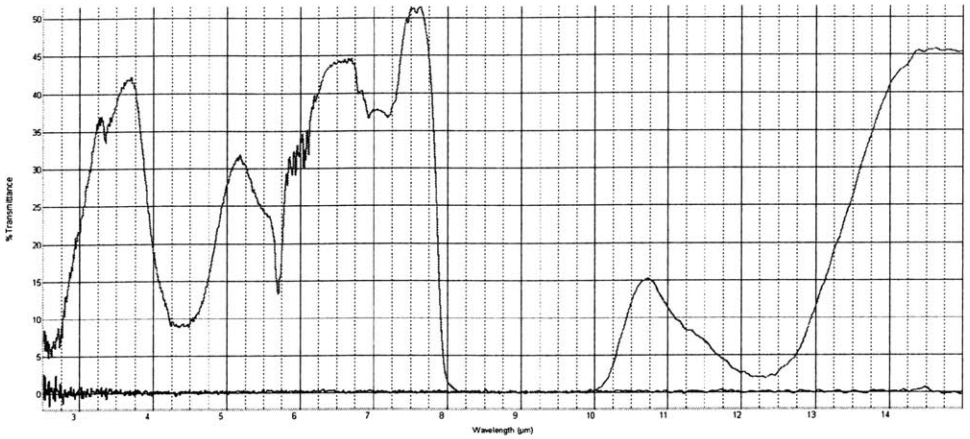

Figure A-19: Two-layer grating (layer 2 - minimum spacing, 1.8μm pitch ; layer 1 - double pitch) TM (red) and TE (blue) intensity transmittance vs. wavelength.

A.2.4 Two-Layer Grating, 1.8μm Pitch (No Relative Shift)

(Filter 24, Name: polarizer1_2layer)

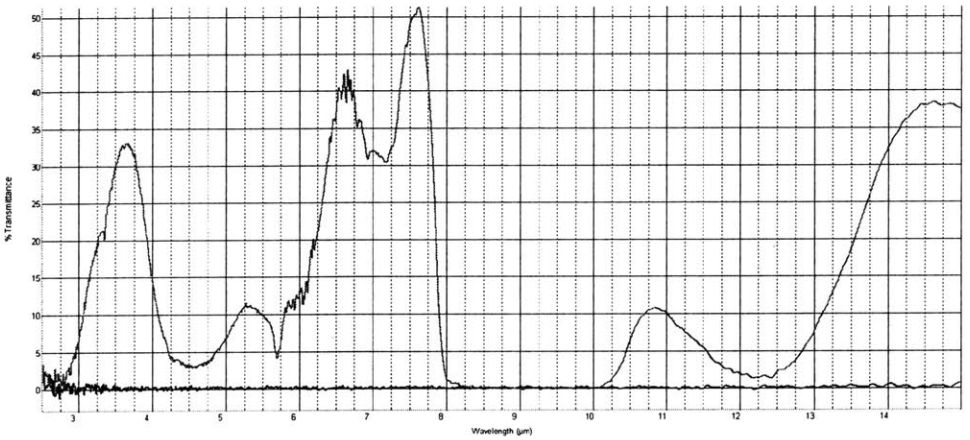

Figure A-20: Two-layer grating, 1.8μm pitch (no relative shift) TM (red) and TE (blue) intensity transmittance vs. wavelength.

A.2.5 Two-Layer Grating, 1.8μm Pitch (0.15μm Relative Grating Shift)

(Filter 23, Name: polarizer1_2layer15)

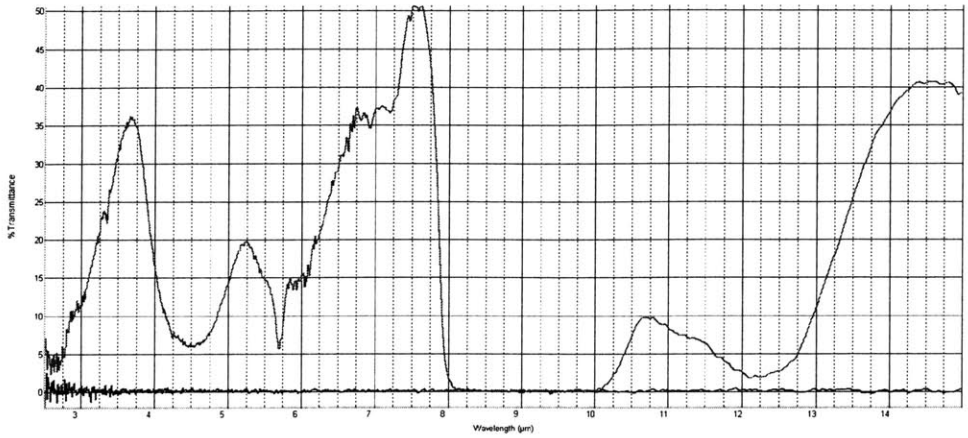

Figure A-21: Two-layer grating, 1.8μm pitch (0.15μm relative grating shift) TM (red) and TE (blue) intensity transmittance vs. wavelength.

A.2.6 Two-Layer Grating, 1.8μm Pitch (0.30μm Relative Grating Shift)

(Filter 22, Name: polarizer1_2layer30)

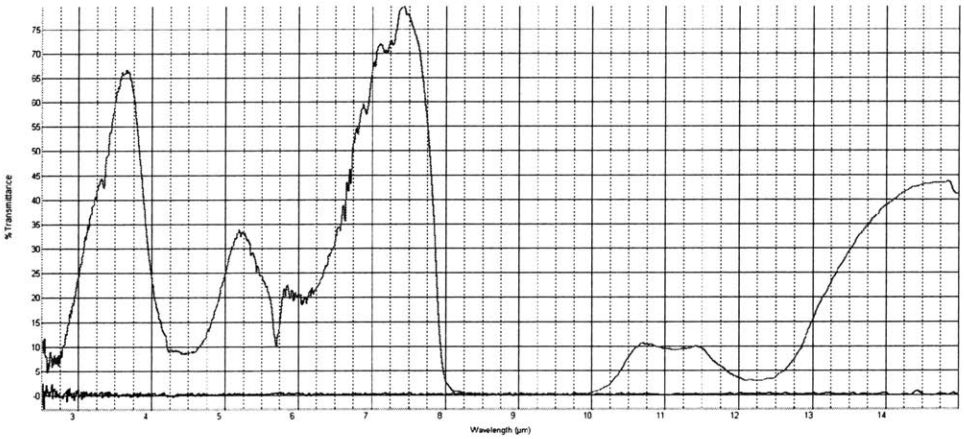

Figure A-22: Two-layer grating, 1.8μm pitch (0.30μm relative grating shift) TM (red) and TE (blue) intensity transmittance vs. wavelength.

A.2.7 Two-Layer Grating, 1.8μm Pitch (0.45μm Relative Grating Shift)

(Filter 21, Name: polarizer1_2layer45)

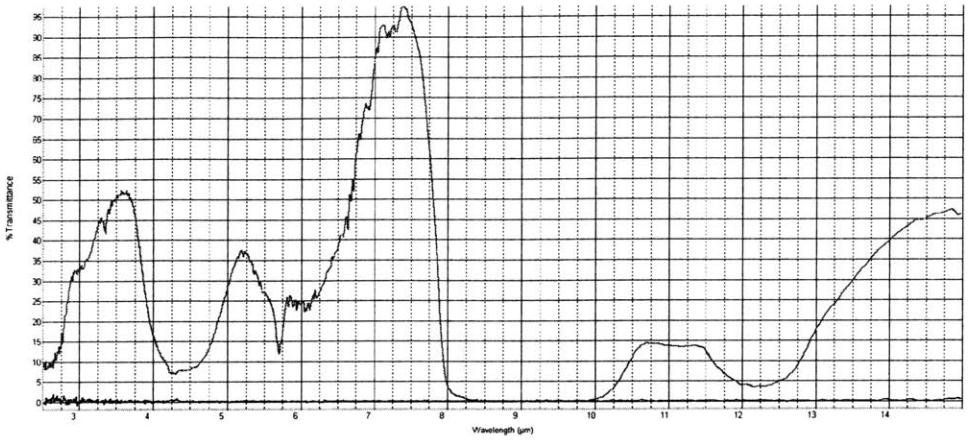

Figure A-23: Two-layer grating, 1.8μm pitch (0.45μm relative grating shift) TM (red) and TE (blue) intensity transmittance vs. wavelength.

A.2.8 Two-Layer Grating, 1.8μm Pitch (0.60μm Relative Grating Shift)

(Filter 20, Name: polarizer1_2layer60)

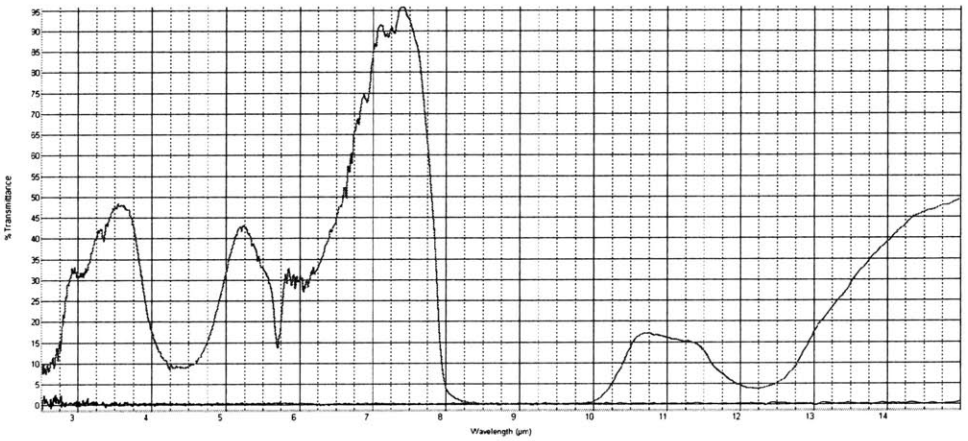

Figure A-24: Two-layer grating, 1.8μm pitch (0.60μm relative grating shift) TM (red) and TE (blue) intensity transmittance vs. wavelength.

A.2.9 Two-Layer Grating, 1.8μm Pitch (0.75μm Relative Grating Shift)

(Filter 19, Name: polarizer1_2layer75)

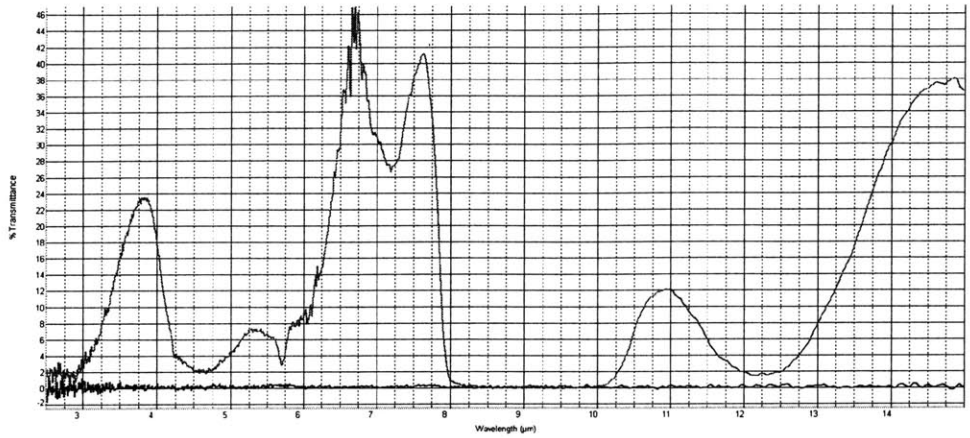

Figure A-25: Two-layer grating, 1.8μm pitch (0.75μm relative grating shift) TM (red) and TE (blue) intensity transmittance vs. wavelength.

A.2.10 Two-Layer Grating, 1.8μm Pitch (0.90μm Relative Grating Shift)

(Filter 18, Name: polarizer1_2layer90)

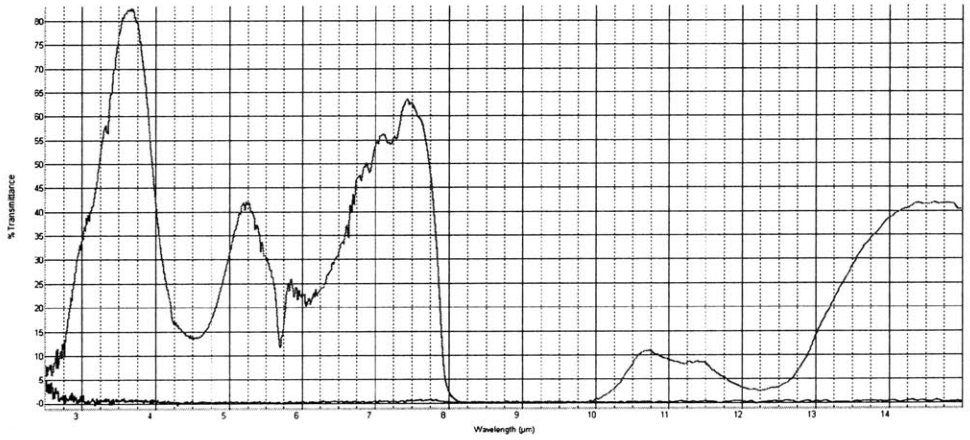

Figure A-26: Two-layer grating, 1.8μm pitch (0.90μm relative grating shift) TM (red) and TE (blue) intensity transmittance vs. wavelength.

A.2.11 Crossed Gratings, 1.8μm Pitch (Layer 1 and Layer 2)

(Filter 17, Name: polarizer1_layer1and2_crossed)

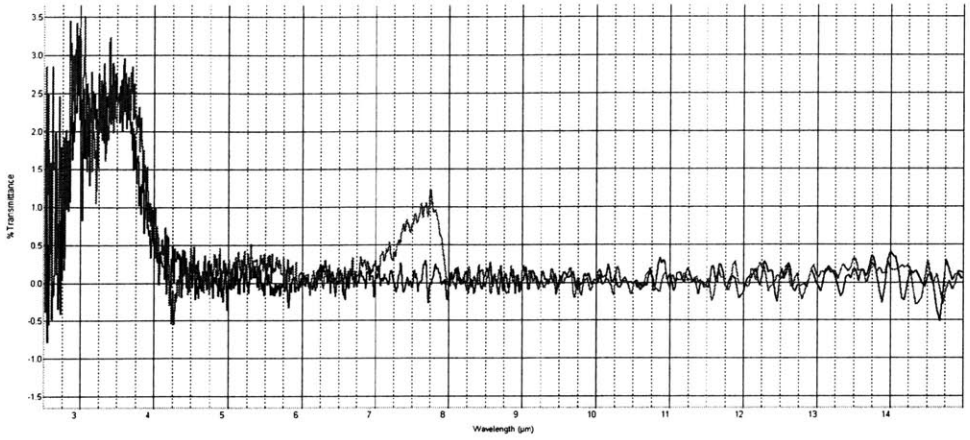

Figure A-27: Crossed gratings, 1.8μm pitch (layer 1 and layer 2) TM (red) and TE (blue) intensity transmittance vs. wavelength.

A.2.12 Single Grating, 2.4μm Pitch, Layer 1

(Filter 14, Name: polarizer2_layer1)

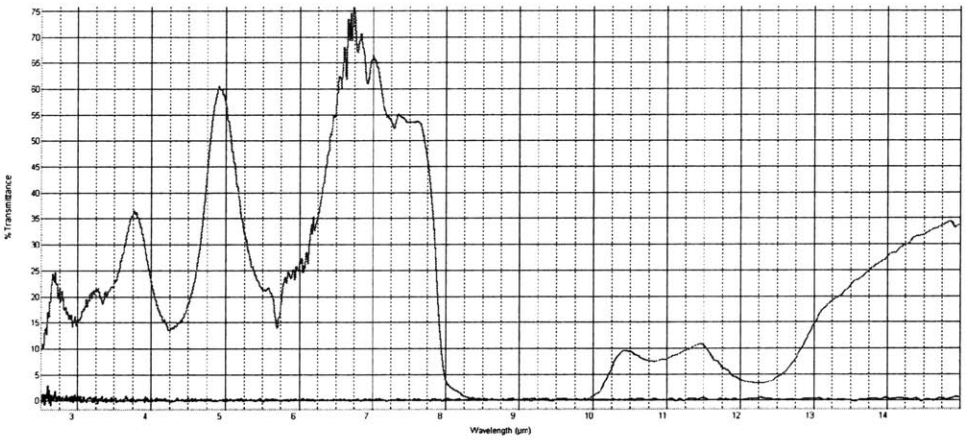

Figure A-28: Single grating, 2.4μm pitch, layer 1, TM (red) and TE (blue) intensity transmittance vs. wavelength.

A.2.13 Single Grating, 2.4μm Pitch, Layer 2

(Filter 8, Name: polarizer2_layer2)

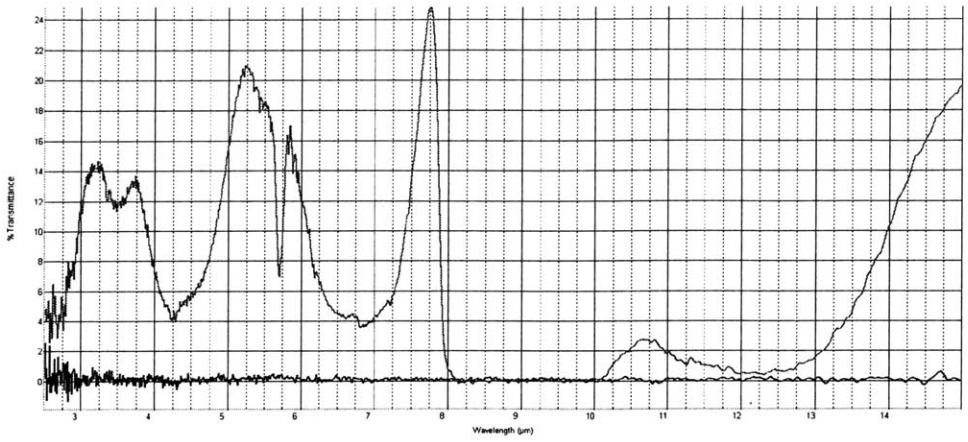

Figure A-29: Single grating, 2.4μm pitch, layer 2, TM (red) and TE (blue) intensity transmittance vs. wavelength.

A.2.14 Single Grating, 2.4μm Pitch, Layer 3

(Filter 4, Name: polarizer2_layer3)

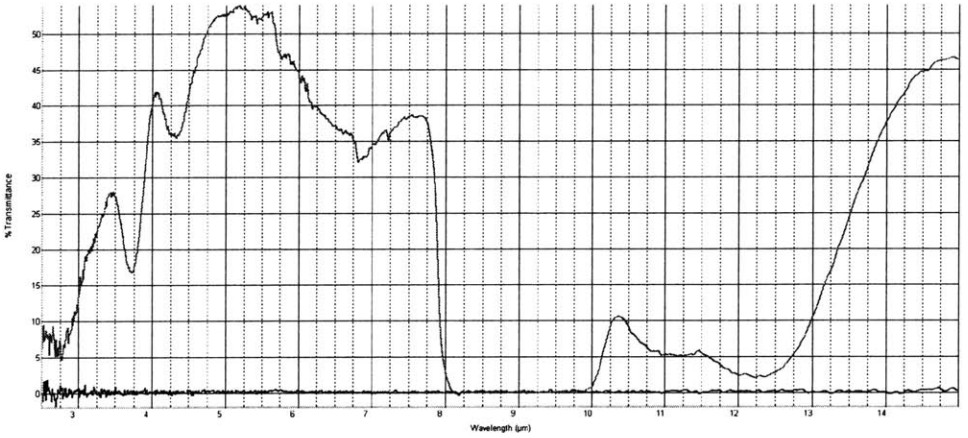

Figure A-30: Single grating, 2.4μm pitch, layer 3, TM (red) and TE (blue) intensity transmittance vs. wavelength.

A.2.15 Two-Layer Grating, 2.4μm Pitch (Layer 1 and Layer 2)

(Filter 13, Name: polarizer2_layer1and2)

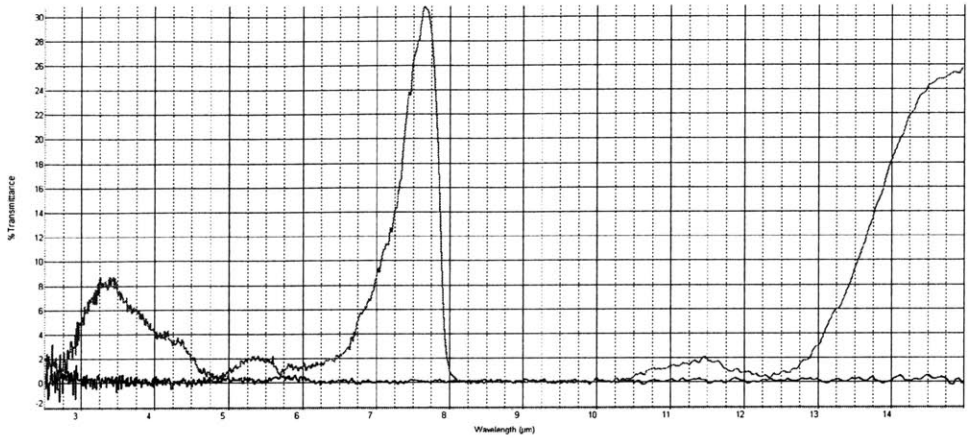

Figure A-31: Two-layer grating, 2.4μm pitch (layer 1 and layer 2) TM (red) and TE (blue) intensity transmittance vs. wavelength.

A.2.16 Two-Layer Grating, 2.4μm Pitch (Layer 1 and Layer 3)

(Filter 9, Name: polarizer2_layer1and3)

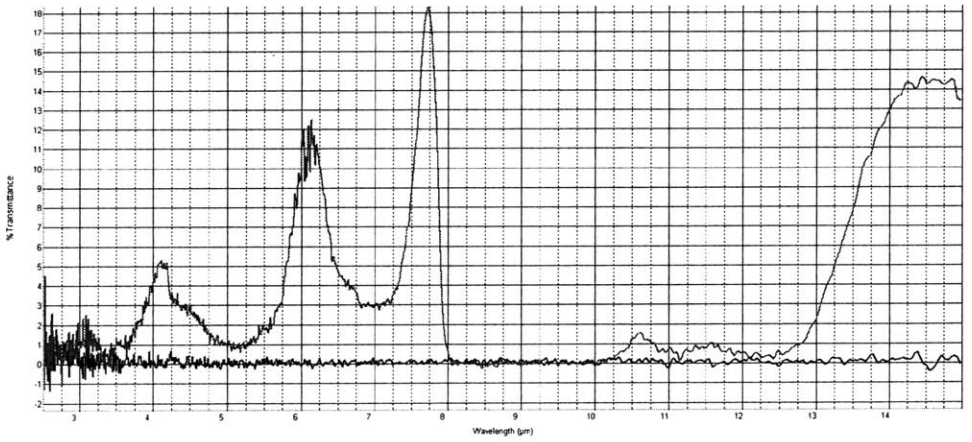

Figure A-32: Two-layer grating, 2.4μm pitch (layer 1 and layer 3) TM (red) and TE (blue) intensity transmittance vs. wavelength.

A.2.17 Two-Layer Grating, 2.4μm Pitch (Layer 2 and Layer 3)

(Filter 5, Name: polarizer2_layer2and3)

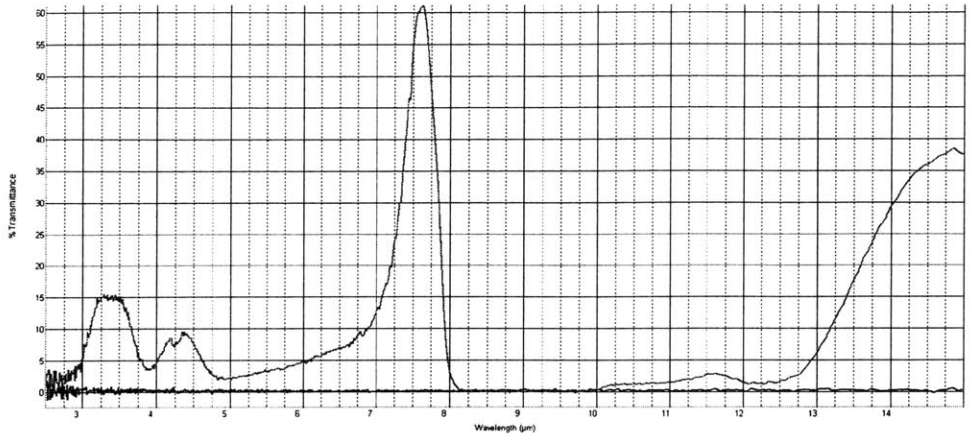

Figure A-33: Two-layer grating, 2.4μm pitch (layer 2 and layer 3) TM (red) and TE (blue) intensity transmittance vs. wavelength.

A.2.18 Three-Layer Grating, 2.4μm Pitch (Layer 1, Layer 2,and Layer 3)

(Filter 10, Name: polarizer2_layer1and2and3)

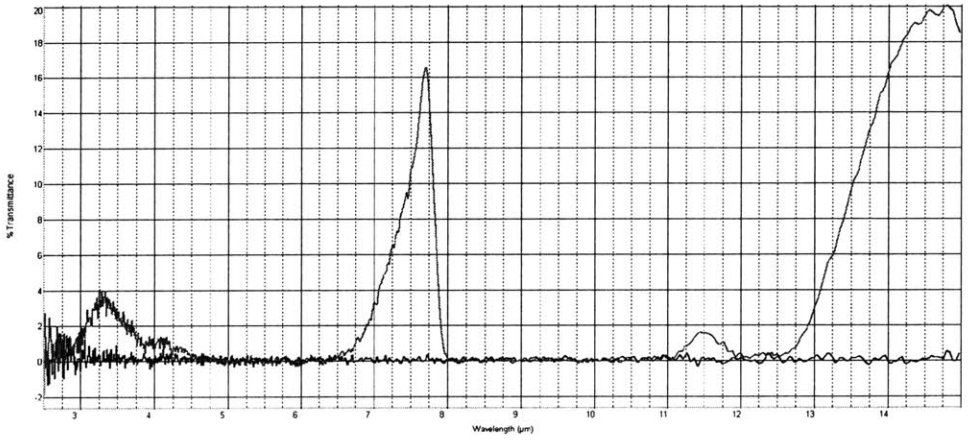

Figure A-34: Three-layer grating, 2.4μm pitch (layer 1, layer 2,and layer 3) TM (red) and TE (blue) intensity transmittance vs. wavelength.

A.2.19 Crossed Grating, 2.4μm Pitch (Layer 1 and Layer 2)

(Filter 12, Name: polarizer2_layer1and2_crossed)

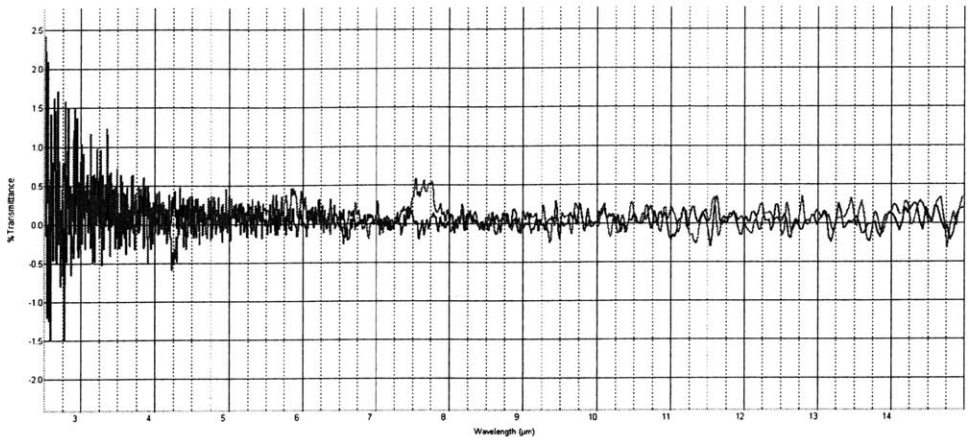

Figure A-35: Crossed grating, 2.4μm pitch (layer 1 and layer 2) TM (red) and TE (blue) intensity transmittance vs. wavelength.

A.2.20 Two-Layer Grating, 2.4μm Pitch (Layer 2 - Normal Spacing; Layer 3 - Double Pitch)

(Filter 7, Name: polarizer2_layer2_dp3)

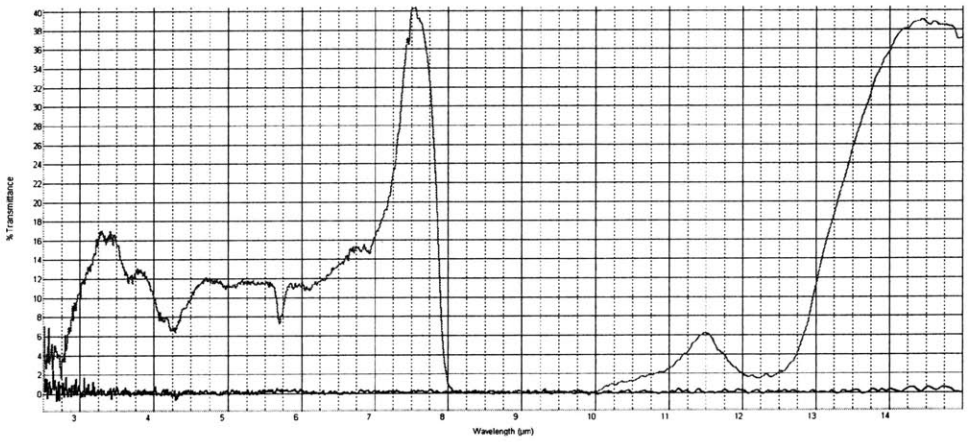

Figure A-36: Two-layer grating, 2.4μm pitch (layer 2 - normal spacing; layer 3 - double pitch) TM (red) and TE (blue) intensity transmittance vs. wavelength.

A.2.21 Three-Layer Grating, 2.4μm Pitch (Layer 1 and Layer 2 - Normal Spacing; Layer 3 - Double Pitch)

(Filter 11, Name: polarizer2_layer1and2_dp3)

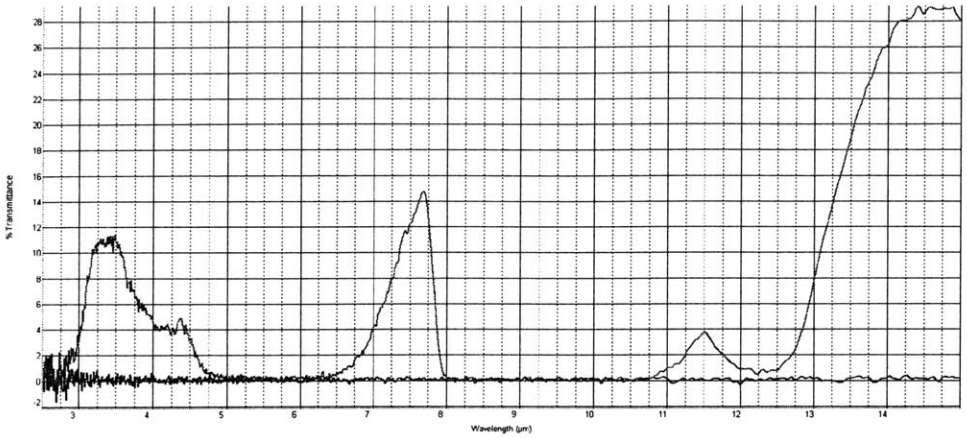

Figure A-37: Three-layer grating, 2.4μm pitch (layer 1 and layer 2 - normal spacing; layer 3 - double pitch) TM (red) and TE (blue) intensity transmittance vs. wavelength.

A.2.22 Three-Layer Grating, 2.4μm Pitch (Layer 2 - Normal Spacing; Layer 1 and Layer 3 - Double Pitch)

(Filter 6, Name: polarizer2_layer2_13dp)

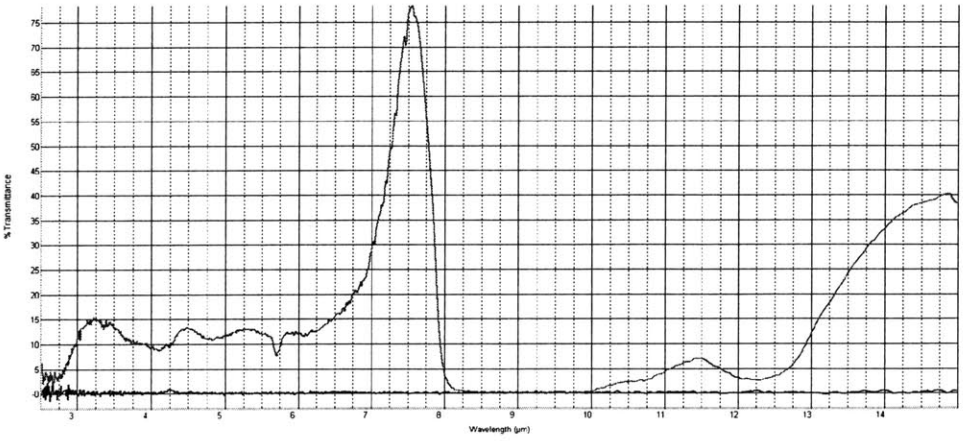

Figure A-38: Three-layer grating, 2.4μm pitch (layer 2 - normal spacing; layer 1 and layer 3 - double pitch) TM (red) and TE (blue) intensity transmittance vs. wavelength.

A.2.23 Meanderline Grating, (Layer 1 - Minimum Spacing)

(Filter 1, Name: polarizer_meanderline_wire)

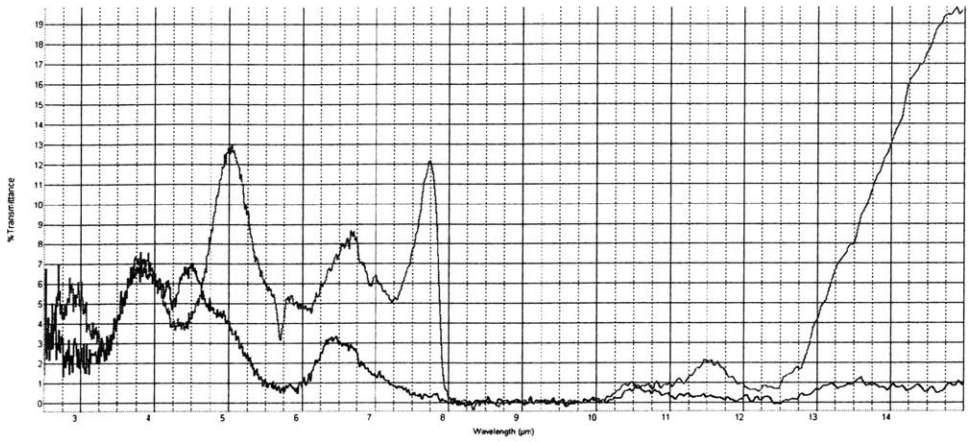

Figure A-39: Meanderline grating, (layer 1 - minimum spacing) TM (red) and TE (blue) intensity transmittance vs. wavelength.

A.2.24 Inverse Meanderline Grating (Layer 1 - Minimum Spacing)

(Filter 3, Name: polarizer_meanderline_wire_inv)

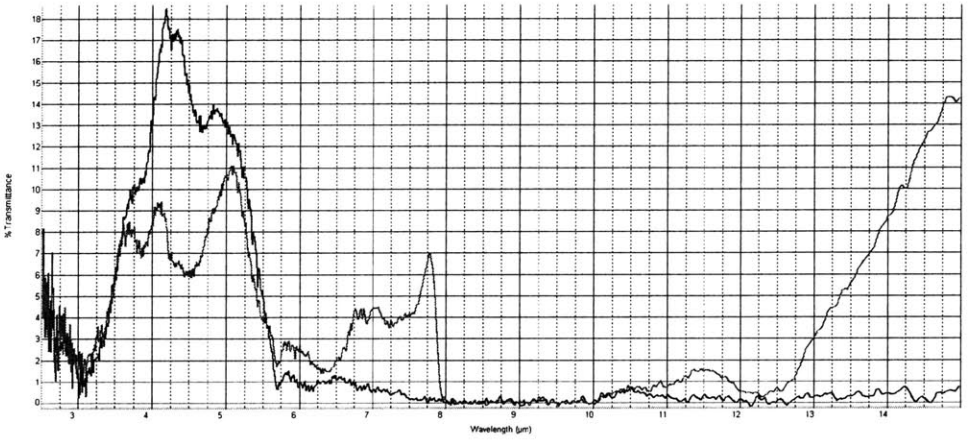

Figure A-40: Inverse meanderline grating (layer 1 - minimum spacing) TM (red) and TE (blue) intensity transmittance vs. wavelength.

A.2.25 Two-Layer Meanderline Grating (Layer 1 and Layer 2 - Minimum Spacing)

(Filter 2, Name: polarizer_meanderline2_wire)

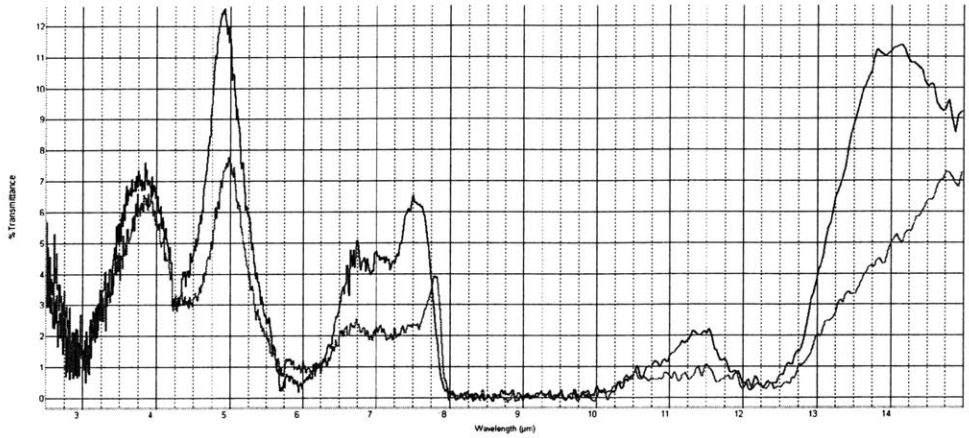

Figure A-41: Two-layer meanderline grating (layer 1 and layer 2 - minimum spacing) TM (red) and TE (blue) intensity transmittance vs. wavelength.

A.3 Wire grid filter arrays

A.3.1 9×9 Unit 3×3 Cells with Non-Manhattan Diagonal Grating

Twenty-seven strip, three-polarization states array (9x9 unit 3x3 cells) (Filter 39, Name: 9x9)

A.3.2 9×9 Unit 3×3 Cells with Meanderline Diagonal Grating

Twenty-seven strip, three-polarization states array with meanderline $45^{c}irc$ polarizer (9x9 unit 3x3 cells) (Filter 38, Name: 9x9_funkydiag)

A.4 Radar-type IR filters

A.4.1 Cross-Type Filter

Cross-type filter (Filter 36, Name: cross2)

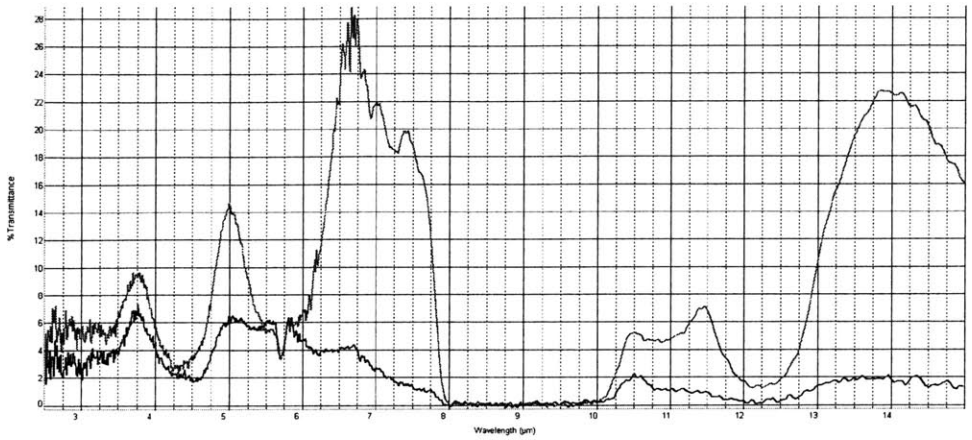

Figure A-42: Cross-type filter, TM (red) and TE (blue) intensity transmittance vs. wavelength.

A.4.2 Two-Layer Cross Filter

Two-layer cross filter (Filter 35, Name: cross2_2layer)

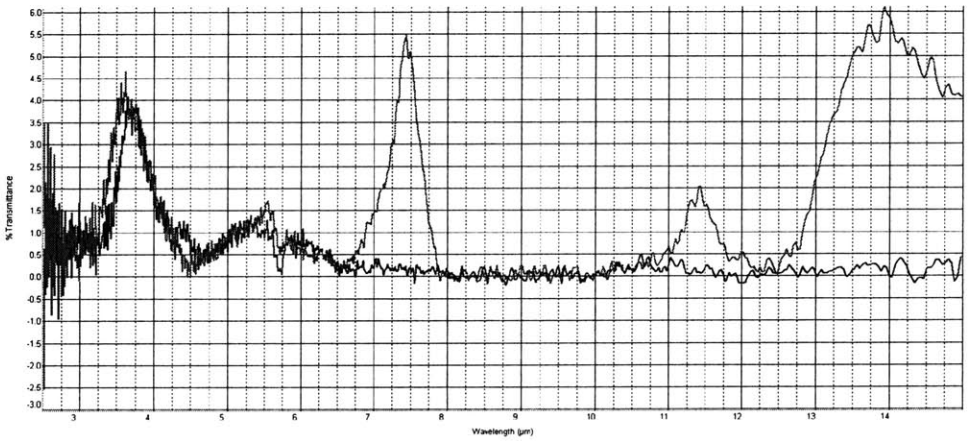

Figure A-43: Two-layer cross filter, TM (red) and TE (blue) intensity transmittance vs. wavelength.

A.4.3 Square-Line Punch Filter (Eyeball Filter)

Square-line punch filter (Filter 34, Name: eyeballs)

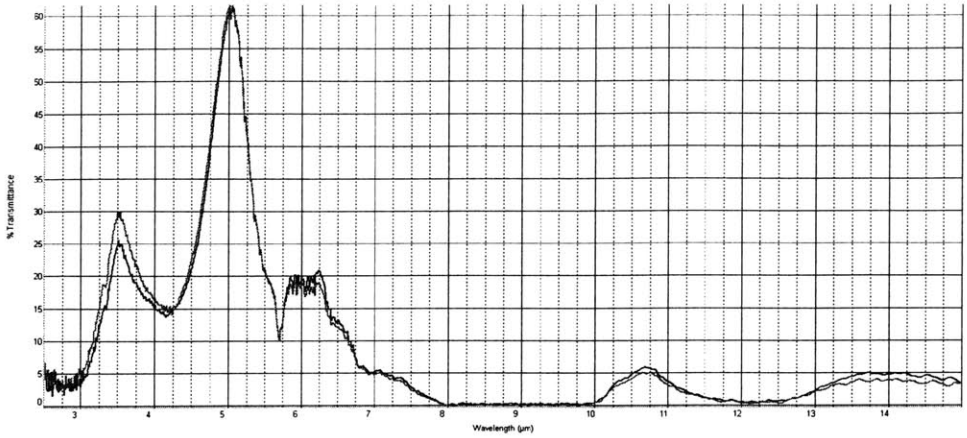

Figure A-44: Square-line punch filter (eyeball filter) TM (red) and TE (blue) intensity transmittance vs. wavelength.

A.4.4 Rectangular-Line Punch Filter (Oblong Eyeball Filter)

Rectangular-line punch filter (Filter 33, Name: eyeballs2)

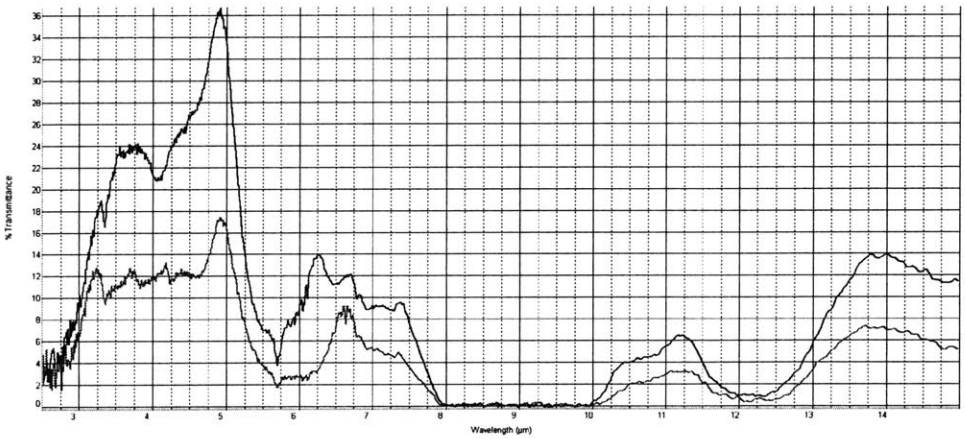

Figure A-45: Rectangular-line punch filter (oblong eyeball filter) TM (red) and TE (blue) intensity transmittance vs. wavelength.

A.4.5 Two-Layer Square-Line Punch Filter

Two-layer square-line punch filter (Filter 31, Name: eyeballs_2layer)

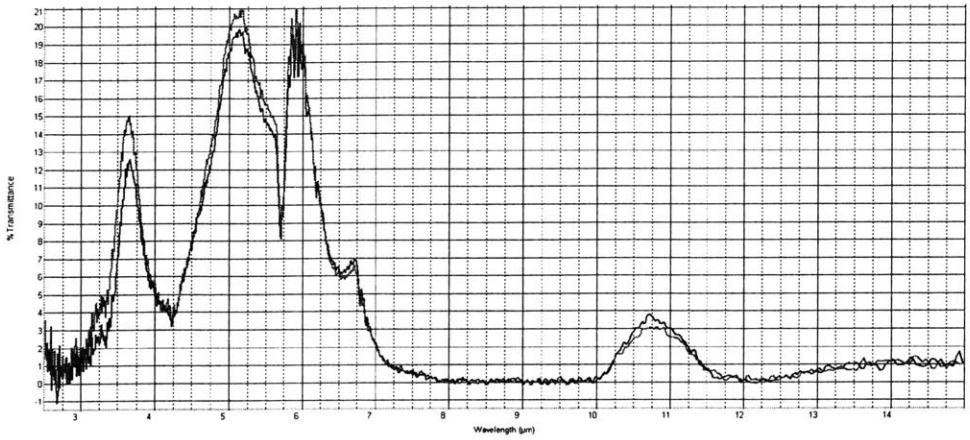

Figure A-46: Two-layer square-line punch filter, TM (red) and TE (blue) intensity transmittance vs. wavelength.

A.4.6 Two-Layer Rectangular-Line Punch Filter

Two-layer rectangular-line punch filter (Filter 32, Name: eyeballs2_2layer)

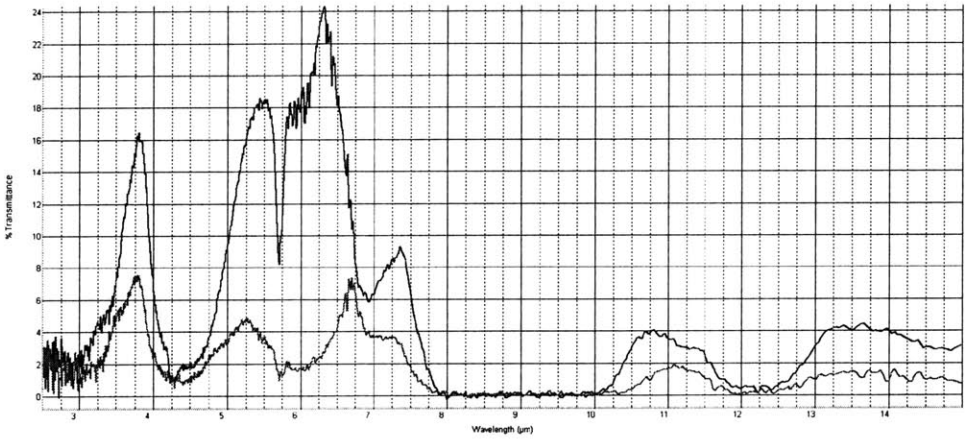

Figure A-47: Two-layer rectangular-line punch filter, TM (red) and TE (blue) intensity transmittance vs. wavelength.

A.4.7 Rectangular-Line Punch Filter with Single-Layer Grating, 2.4μm Pitch

Rectangular-line punch filter with polarizer (Filter 30, Name: eyeballs_and_polarizer)

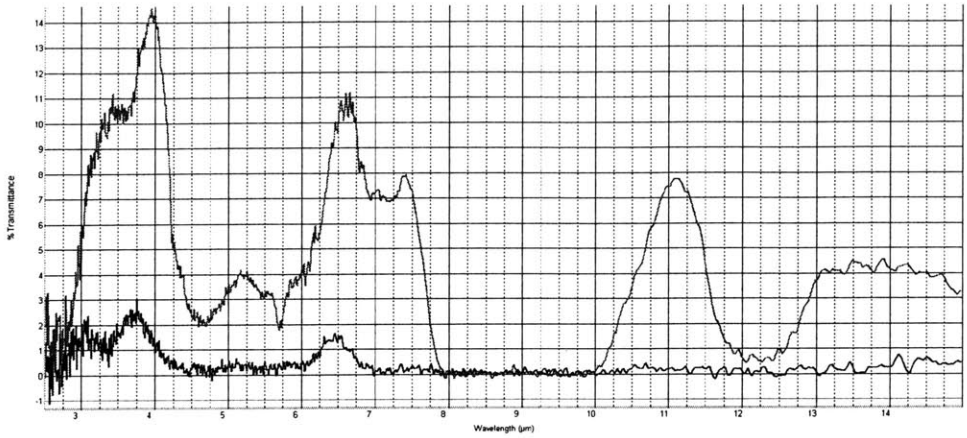

Figure A-48: Rectangular-line punch filter with single-layer grating, 2.4μm pitch, TM (red) and TE (blue) intensity transmittance vs. wavelength.

A.4.8 Cross-Potent Filter

Cross Potent filter (Filter 29, Name: kaiser)

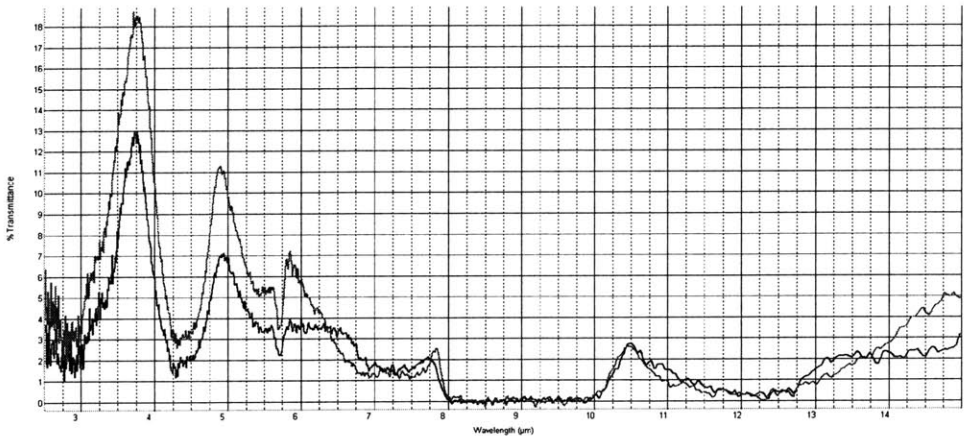

Figure A-49: Cross-potent Filter, TM (red) and TE (blue) intensity transmittance vs. wavelength.

A.4.9 Two-Layer Cross-Potent Filter

Two-layer Cross Potent filter (Filter 28, Name: kaiser_2layer)

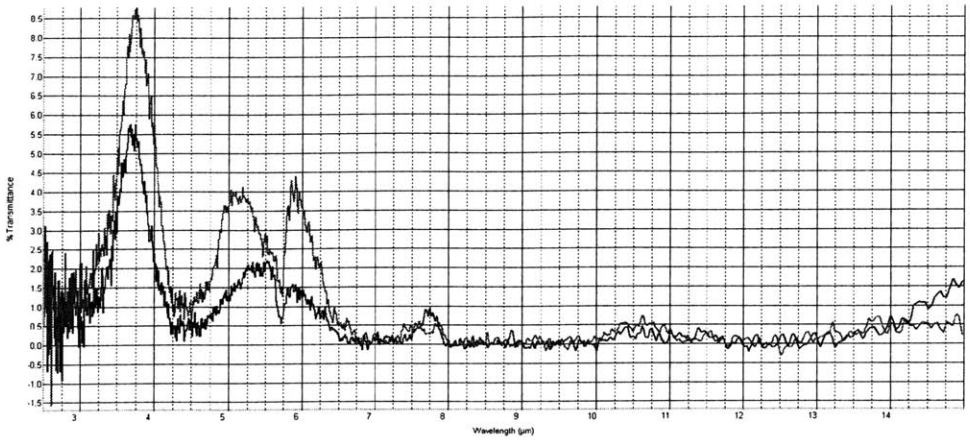

Figure A-50: Two-layer cross-potent filter, TM (red) and TE (blue) intensity transmittance vs. wavelength.

A.4.10 Rectangular Slot Array Filter

Perforated grid filter (Filter 27, Name: perfgrid2)

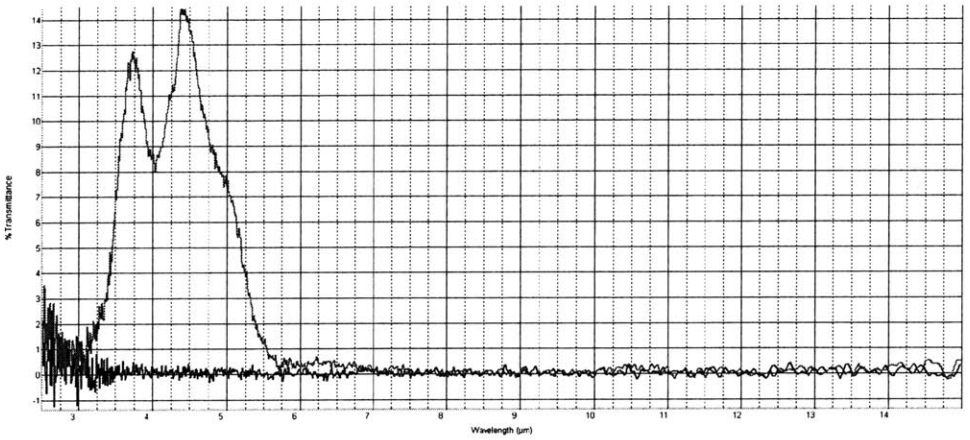

Figure A-51: Rectangular slot array filter, TM (red) and TE (blue) intensity transmittance vs. wavelength.

A.4.11 Two-Layer Rectangular Slot Array Filter

Two-layer perforated grid filter (Filter 26, Name: perfgrid2_2layer)

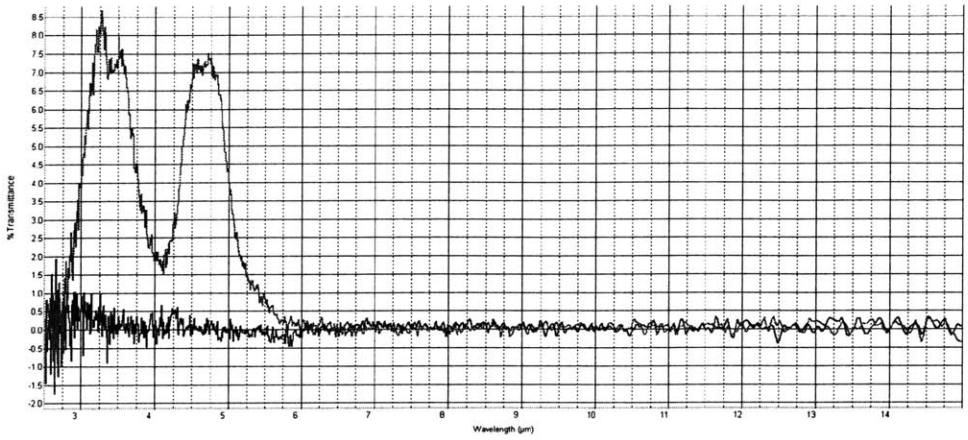

Figure A-52: Two-layer rectangular slot array filter, TM (red) and TE (blue) intensity transmittance vs. wavelength.

A.4.12 Open Space On Chip

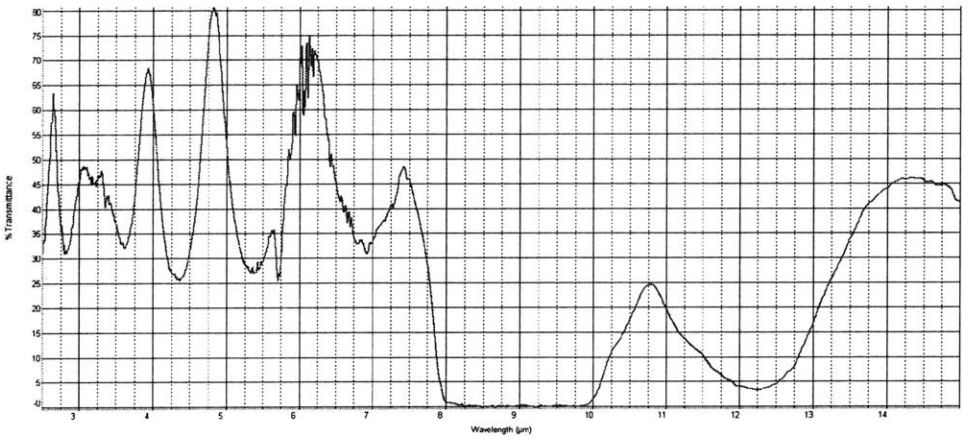

Figure A-53: Intensity transmittance vs. wavelength for non-metal-containing open-space portion of chip.

Bibliography

[1] T. J. Rogne, F. G. Smith, and J. E. Rice. Passive target detection using polarized components of infrared signature. *Proc. of SPIE, Polarimetry: Radar, Infrared and Visible, Ultraviolet and X-Ray*, 1317:242, 1990.

[2] T. J. Rogne, R. Maxwell, J. Nicoll, and R. Legault. Ir polarization for target cuing. *Proc. IRIS, Passive Sensors*, 1:323, 1997.

[3] M. J. Duggin, W. G. Egan, and J. Gregory. Measurements of polarization of targets of differing albedo and shadow depth. *Proc. of SPIE, Targets and Backgrounds: Characterization and Representation V*, 3699:27–37, 1999.

[4] W. G. Egan. Enhancement of optical detectability with polarization. *Proc. of SPIE, Targets and Backgrounds: Characterization and Representation V*, 3699:38, 1999.

[5] D. C. Kim. *Design, Development and Characterization of an Integrated Multispectral Polarimetric Sensor.* PhD thesis, Massachusetts Institute of Technology, 2001.

[6] C. Warde. Atmoshperic imaging and communications sensor technologies. Final technical report, Air Force Research Lab Contract F19628-99-C-0052, Massachusetts Institute of Technology, 2002.

[7] Joseph P. Estrera, Timothy Ostromek, Wayne Isbell, and Antonio Bacarella. Modern night vision goggles for advanced infantry applications. *Proc. of SPIE,*

Helmet and Helmet-Mounted Displays VIII: Technologies and Applications, 5079:196–207, 2003.

[8] Bruno Fieque, Arnaud Crastes, Olivier Legras, and Jean-Luc Tissot. MWIR uncooled microbolometer, a way to increase the number of applications. *Proc. of SPIE, Infrared Technology and Applications XXXI*, 5783:531–538, 2005.

[9] Jean Jacques Yon, Gerard Destefanis, and Eric Mottin. Recent develpoment in infrared technologies at leti for earth observation. *Proc. of SPIE, Sensors, Systems, and Next-Generation Satellites VIII*, 5570:525–536, 2004.

[10] Timothy J. Spera and Burton D. Figler. Uncooled infrared sensors for an integrated sniper location system. *Proc. of SPIE*, 2938:326–339, 1997.

[11] Derick M. T. Chochrane, Paul A. Manning, and Tim A. Whyllie. Uncooled thermal imaging sensor for UAV applications. *Proc. of SPIE, Infrared Technology and Applications XXVII*, 4369:168–177, 2001.

[12] M. Aguilar, D. A. Fay, W. D. Ross, A. M. Waxman, D. B. Ireland, and J. P. Racamato. Real-time fusion of low-light CCD for uncooled IR imagery for color night vision. *Proc. of SPIE, Conference on Enhanced and Synthetic Vision*, 3364:124–135, 1998.

[13] Allen M. Waxman, Eugene D. Savoye, David A. Fay, Mario Aguilar, Alan N. Grove, James E. Carrick, and Joseph P. Racamato. Electronic imaging aids for night driving: Low-light CCD, uncooled thermal IR, and color fused visible/lwir. *Proc. of SPIE*, 2902:62–73, 1997.

[14] Glen L. Francisco. Advances in ir sensor for law enforcement. *Proc. of SPIE, Sensors, and Command and Control, Communications, and Intelligence (C3I) Technologies for Homeland Defense and Law Enforcement*, 4708:192–200, 2002.

[15] T. Schimert, N. Cunningham, G. Francisco, R. Gooch, J. Gooden, P. McCardel, B. Neal, B. Ritchey, J. Rife, A. J. Syllaios, and J. Tregilgas. Low cost, low

poer uncooled 120x160 a-si-based micro infrared camera for law enforcement applications. *Proc. of SPIE, Enabling Technologies for Law Enforcement and Security*, 4232:187–194, 2001.

[16] Eric Brindley, Jack Lillie, Pete Plocki, and Robert Volz. Selection of the thermal imaging approach for the XM29 combat rifle fire control system. *Proc. of SPIE, Infrared Technologies and Applications XXIX*, 5074:380–395, 2003.

[17] Herman E. Scott, Stephen H. Jones, Frank Iannarilli, and Kurt Annen. Hyperspectral IR polarimetry with applications in demining and unexploded ordanance detection. *Proc. of SPIE, Conference on Environmental Monitoring and Remediation Technologies*, 3534:300–320, 1999.

[18] J. W. Salisbury and D. M. D'Aria. Emissivity of tererstrial materials in the 8-14 micron atmospheric window. *Remote Sens. Environ.*, 42:83–106, 1992.

[19] Jeffrey R. Johnson, Paul G. Lucey, Keith A. Horton, and Edwin M. Winter. Infrared measurements for pristine and disturbed soils. 1. spectral contrast differences between field and laboratory data. *Remoste Sens. Environ.*, 64:34–46, 1998.

[20] J. N. Cederquist, T. J. Rogne, and C. R. Schwartz. Multispectral infrared target detection: Phenomenology and modeling. *Proc. of SPIE*, 1954:192–197, 1993.

[21] Tzong-Sheng Lee and Jin-Shown Shie. Feasability study on low-resolution uncooled thermal imagers for home-security applications. *Opt. Eng.*, 39(6):1431–1440, 2000.

[22] Stephen K. Holland, Roland H. Krauss, and Gabriel Laufer. Demonstration of multi-spectral remote chemical sensing and identification using uncooled detectors. *Proc. of SPIE, Sensors, and Command and Control, Communications, and Intelligence (C3I) Technologies for Homeland Security and Homeland Defense III*, 5403:371–377, 2004.

[23] James W. Hoffman, Philip J. Riggan, Stephanie A. Griffin, Ronald C. Grush, William H. Grush, and James Pena. Firemapper(r)2.0: A multispectral, uncooled infrared imaging system for airborne wildfire mapping and remote sensing. *Proc. of SPIE, Infrared Spaceborne Remote Sensing XI*, 5152:92–99, 2003.

[24] Robert A. Freitas. *Nanomedicine, Volume 1: Basic Capabilities.* Landes Bioscience, 1999.

[25] Joseph Kostrzewa, William Meyer, George Poe, and William Terre. Addressing the challenges of thermal imaging for firefighting applications. *Proc. of SPIE, Infrared Technology and Applications XXIX*, 5074:564–573, 2003.

[26] M. Emanuel, H. Caron, B. Kovacevic, M. Faina-Cherkaoui, L. Wrobel, and G. Turcotte. Alliedsignal driver's viewer enhancement (DVE) for paramilitary and commercial applications. *Proc. of SPIE, Conference on Infrared Technology and Applications XXV*, 3698:170–179, 1999.

[27] T. Meitzler, E. Sohn, R. Karlsen, G. Gerhart, and S. Lakshmanan. Simulation and comparison of infrared sensors for automotive applications. *Proc. of SPIE*, 2470:38–46, 1995.

[28] P. G. Datskos, S. G. Demos, and S. Rajic. Miniature uncooled infrared sensitive detectors for *in Vivo* biomedical applications. *Proc. of SPIE*, 3253:94–100, 1998.

[29] Tim White and Arthur Leary. Digital ir imaging capability for medical applications. *Proc. of SPIE, Conference on Battlefield Biomedical Technologies*, 3712:35–46, 1999.

[30] Hank Hogan. Astronomical research spawns detector innovation. *Photonics Spectra*, pages 55–64, July 2004.

[31] Richard Volpe. Mars rover navigation results using sun sensor heading determination. *Proc. of IEEE, International Conference on Intelligent Robots and Systems*, pages 460–467, 1999.

[32] M. Fouquet and M. N. Sweeting. UoSAT-12 minisatellite for high performance Earth observation at low cost. Technical report, Symposium on Future Earth Observation Missions, 47th IAF Congress, October 1996.

[33] Steven A. Hildreth. Missile defense: The current debate. Crs report for congress, Congressional Research Service, July 2005.

[34] Dong-Hyun C. Kim. *Design, Development, and Characterization of an Integrated Multispectral Polarimetric Sensor System.* PhD thesis, Massachusetts Institute of Technology, May 2001.

[35] W. G. Egan. Proposed design of an imaging spectropolarimeter/photopolarimeter for remote sensing of earth resources. *Opt. Eng.*, 25(10):1155, 1986.

[36] W. G. Egan. Polarization in remote sensing II. *Proc. of SPIE, vol. 1166 Polarization and Remote Sensing*, page 23, 1989.

[37] W. G. Egan. Polarization in remote sensing. *Proc. of SPIE, Polarization and Remote Sensing*, 1747:2–48, 1992.

[38] L. D. Travis. Remote sensing of aerosols with the earth observing scanning polarimeter. *Proc. of SPIE, vol. 1747 Polarization and Remote Sensing*, page 72, 1992.

[39] P. Y. Deschamps, M. Herman, A. Podaire, and A. Ratier. The POLDER instrument: mission objectives. *Proc. of SPIE, vol. 1747 Polarization and Remote Sensing*, page 72, 1992.

[40] D. A. Glenar, J. J. Hillman, B. Saif, and J. Bergstrahl. Polaris II: an acousto-optic imaging spectropolarimeter for ground-based astronomy. *Proc. of SPIE, vol. 1747 Polarization and Remote Sensing*, page 92, 1992.

[41] D. H. Goldstein and R. A. Chipman. Infrared spectropolarimeter. *U.S. Patent*, #5,045,701, 1991.

[42] D. B. Chenault and R. A. Chipman. Infrared spectropolarimetry. *Proc. of SPIE, vol. 1166 Polarization Considerations for Optican Systems II*, page 254, 1989.

[43] J. L. Pezzaniti and R. A. Chipman. Mueller matrix imaging polarimeter. *Opt. Eng.*, 43(6):1558, 1995.

[44] B. H. Miles, E. R. Cespedes, and R. A. Goodson. Polarization-based active/passive scanning system for minefield detection. *Proc. of SPIE, vol. 1747 Polarization and Remote Sensing*, page 139, 1992.

[45] K. P. Bishop, H. D. McIntire, M. P. Fetrow, and L. McMackin. Multi-spectral polarimeter imaging in the visible to near IR. *Proc. of SPIE, vol. 3699 Targets and Backgrounds: Characterization and Representation V*, page 49, 1999.

[46] K. Oka and T. Kato. Spectroscopic polarimetry with a channeled spectrum. *Opt. Lett.*, 24:1475, 1999.

[47] H. Takami, H. Shiba, S. Sato, T. Yamashita, and Y. Kobayashi. A near-infrared prism spectrophotopolarimeter. *Publ. Astro. Soc. of the Pacific*, 104:949, 1992.

[48] M. R. Descour and E. L. Dereniak. Computer-tomography imaging spectrometer: experimental calibration and reconstruction results. *Appl. Opt.*, 34:4817, 1995.

[49] C. S. L. Chun, D. L. Flemming, W. A. Harvey, E. J. Torok, and F. A. Sadjadi. Synthetic vision using polarization-sensitive, thermal imaging. *Proc. of SPIE, vol. 2736 Enhanced and Synthetic Vision*, page 9, 1996.

[50] R. M. A. Azzam and K. A. Giardina. Photopolarimeter based on planar grating diffraction. *J. Opt. Soc. Am. A*, 10(6):1190, 1993.

[51] R. M. A. Azzam. Diffraction-grating photopolarimeter and spectrophotopolarimeter. *U.S. Patent*, # 5,337,146, 1994.

[52] J. R. Maxwell and T. J. Rogne. Advances in infrared imaging, Part 1 & 2. *Spectral Reflections, IRIA Newsletter*, 97-01 & 97-04, 1997.

[53] W. A. Shurcliff. *Polarized Light: Production and Use.* Harvard University Press, Cambridge, Massachusetts, 1962.

[54] E. Oliva. Wedged double Wollaston and a device for single shot polarimetric measurements. *Astron. Astrophysics. Suppl. Ser.*, 123:589, 1997.

[55] G. P. Nordin, J. T. Meier, P. C. Deguzman, and M. W. Jones. Micropolarizer array for infrared imaging polarimetry. *J. Opt. Soc. Am. A*, 16(5):1168, 1999.

[56] Matthew H. Smith, James D. Howe, Jacob B. Woodruff, Miranda A. Miller, George R. Ax, Thomas E. Petty, and Elizabeth A. Sornsin. Multispectral infrared stokes imaging polarimeter. *Proc. of SPIE, Polarization: Measurement, Analysis and Remote Sensing II*, 3754:137–143, 1999.

[57] Matthew H. Smith, Miranda A. Miller, Robert V. Blumer, Mark A. Stevens, David M. Teale, and James D. Howe. Infrared stokes polarimeter calibration. *Proc. of SPIE, Polarization: Measurement, Analysis, and Remote Sensing III*, 4133, 2000.

[58] G. Benedetti Michelangeli, R. Viola, N. Liberatore, A. Civetti, F. Pagni, and C. Corsi. Multi-band infrared imaging radiometer. *Infrared Physics and Technology*, 43:279–283, 2002.

[59] Evan Preston, Tom Bergman, Ron Gorenflo, Dave Hermann, Ed Kopala, Tom Kuzma, Larry Lazofson, and Randy Orkis. Development of a field-portable imaging system for scene classification using multispectral data fusion algorithms. *IEEE AES Systems Magazine*, pages 13–19, 1994.

[60] Martin Chamberland, Charles Belzile, Vincent Farley, Jean-Francois Legault, and Karl Schwantes. Advancements in filed-portable imaging radiometric spectrometer technology for chemical detection. *Proc. of SPIE, Chemical and Biological Sensing V*, 5416:63–72, 2004.

[61] Eliel Villa-Aleman. Temperature and emissivity measurements with the multispectral thermal imager satellite at ivanpah playa. *Westinghouse Savannah River Technology Center - USDOE Contract Report DE-AC09-96SR18500*, pages 1–12, 2002.

[62] NASA Landsat Program. http://landsat.gsfc.nasa.gov/about/history.html. Website, Retrieved Jan. 2007.

[63] Jeff Hecht. Ever vigilant, optical sensors already monitor much of our daily lives. *Laser Focus World*, pages 101–108, July 2004.

[64] Brian R. Johnson, Kevin P Czajkowski, Robert P. d'Entremont, Julie A Haggerty, Thomas U. Kampe, Hilary E. Snell, and Jennifer Turner-Valle. An airborne imaging radiometer AIR for atmospheric and surface process studies. *Proc. of SPIE, Multispectral and Hyperspectral Remote Sensing Instruments and Applications II*, 5655:212–221, 2005.

[65] John W. Salisbury and Dana M. D'Aria. Emissivity of terrestrial materials in the 2-3μm atmospheric window. *Remote Sens. Environ.*, 47:345–361, 1994.

[66] J. H. W. G. den Boer, G. M. W. Kroesen, W. de Zeeuw, and F. J. de Hoog. Improved polarizer in the infrared: two wire-grid polarizers in tandem. *Opt. Lett.*, 20(7):800, 1995.

[67] S. S. Wang and R. Magnusson. Multilayer waveguide-grating filters. *Appl. Opt.*, 34(14):2414, 1995.

[68] R. Magnusson and S. S. Wang. Transmission badnpass guided-mode resonance filters. *Appl. Opt.*, 34(35):8106, 1995.

[69] Allen Mann. Infrared optics and zoom lenses. *Tutorial Texts in Optical Engineering, SPIE Press*, TT42:1–13, 1999.

[70] Jose A. Sobrino and Juan Cuenca. Angular variation of thermal infrared emissivity for some natural surface from experimental measurements. *Applied Optics*, 38(18):3931–3936, 1999.

[71] Craig R. Schwartz, Jack N. Cederquist, and Timothy J. Rogne. Comparison of modeled to measured infrared multispectral target/background signatures. *Proc. of SPIE*, 2235:162–184, 1994.

[72] Michael T. Eismann, John H. Seldin, Craig R. Schwartz, James R. Maxwell, Kenneth K. Ellis, Jack N. Cederquist, Alan D. Stocker, Ara Oshagan adn Ray O. Johnson, William A. Shaffer, Marc R. Surette, Martin J. McHugh, Alan P. Schaum, and Larry B. Stotts. Target detection in desert backgrounds: Infrared hyperspectral measurements and analysis. *Proc. of SPIE, Signal and Data Processing of Small Targets*, 2561:80–97, 1995.

[73] Craig R. Schwartz, Michael T. Eismann, John N. Cederquist, and R. O. Johnson. Thermal multispectral detection of military vehicles in vegetated and desert backgrounds. *Proc. of SPIE*, 2742:286–197, 2996.

[74] Alan D. Stocker, Ara Oshagan, John H. Seldin, Jack N. Cederquist, and Craig R. Schwartz. Analysis of infrared multi-spectral target/background field measurements. *Proc. of SPIE*, 2235:148–161, 1994.

[75] Hanna T. Haskett, Donald A. Reago, and Richard Legault. Identification of optimal bands in (3-5um) region for lightweight airborne mine detection (LAMD) system. *Proc. of SPIE, Detection and Remediation Technologies for Mines and Minelike Targets VI*, 4394:246–257, 2001.

[76] Steve Moyer, Ronald G. Driggers, and Richard H. Vollmerhausen. Information differences between subbands of the mid-wave infrared spectrum. *Optical Engineering*, 42(8):2296–2303, 2003.

[77] Stephen M. Doss-Hammel, Carl R. Zeisse, Amalia E. Barrion, Gerrit de Leeuw, Marcel Moerman, Arie N. de Jong, Paul A. Frederickson, and Kenneth L. Davidson. Low-altitude infrared propagation in a coastal zone: Refraction and scattering. *Applied Optics*, 41(18):3706–3724, 2002.

[78] A. M. Waxman, A. N. Gove, M. C. Seibert, D. A. Fay, J. E. Carrick, J. P. Racamato, E. D. Savoye, B. E. Burke, R. K. Reich, W. H. McGonagle, and D. M. Craig. Progress on color night vision: Visible/ir fusion, perception & search and low-light ccd imaging. *Proc. of SPIE*, 2736:96, 1996.

[79] Alfred W. Cooper, William J. Lentz, and Phillip L. Alker. Infrared polarization ship images and contrast in the MAPTIP experiment. *Proc. of SPIE*, 2828:85–96, 1996.

[80] Joseph A. Shaw. Polarimetric measurements of long-wave infrared spectral radiance from water. *Applied Optics*, 40(33):5985–5990, 2001.

[81] Peter N. Raven, David L. Jordan, and Catherine E. Smith. Polarized directional reflectance from laurel and mullein leaves. *Optical Engineering*, 41(5):1002–1012, 2002.

[82] Walter G. Egan. Polarization and surface roughness. *Proc. of SPIE, Scattering and Surface Roughness II*, 3426:144–152, 1998.

[83] Edward D. Palik, editor. *Handbook of Optical Constants of Solids.* Academic Press Inc., 1985.

[84] Naoki Oda, Yutaka Tanaka, Tokuhito Sasaki, Akira Ajisawa, Akihiro Kawahara, and Seiji Kurashina. Performance of 320x240 bolometer-type uncooled infrared detector. *NEC Res. & Develop.*, 44(1):170–174, 2003.

[85] E. Mottin, A. Bain, J. L. Martin, J. L. Ouvrier-Buffet, S. Bisotto, J. J. Yon, and J. L. Tissot. Uncooled amorphous silicon technology enhancement for 25μm pixel pitch achievement. *Proc. of SPIE, Infrared Technology and Applications XXVIII*, 4820:200–207, 2003.

[86] M. Z. Tidrow, W. W. Clark III, W. Tipton, R. Hoffman, W. Beck, S. C. Tidrow, D. N. Robertson, and H. Pollehn. Uncooled infrared detectors and focal plane arrays. *Proc. of SPIE*, 3553:178–187, 1998.

[87] Brian Backer, Thomas Breen, Nancy Hartle, Margaret Kohin, and Robert Murphy. Improvements in state of the art uncooled microbolometer system performance based on volume manufacturing experience. *Proc. of SPIE, Infrared Technology and Applications XXIX*, 5074:500–510, 2003.

[88] D. Murphy, M. Ray, R Wyles, J. ASbrock, N. Lum, J. Wyles, C. Hewitt, A. Kennedy, D. Van Lue, J. Anderson, D. Bradley, R Chin, and T Kostrzewa. High sensitivity 25μm microbolometer FPAs. *Proc. of SPIE, Infrared Detectors and Focal Plane Arrays VII*, 4721:99–110, 2002.

[89] Ben A. Munk. *Frequency Selective Surfaces: Theory and Design.* Wiley-Interscience, New York, 2000.

[90] Ben A. Munk. *Finite Antenna Arrays and FSS.* Wiley-Interscience, New York, 2003.

[91] Irina Puscasu, W. L. Schaich, and Glenn D. Boreman. Modeling parameters for the spectral behavior of infrared frequency-selective surfaces. *Applied Optics*, 40(1):118–124, 2001.

[92] Reinhard Ulrich. Interference filters for the far infrared. *Applied Optics*, 7(10):1987–1996, 1968.

[93] P. G. Huggard, M. Meyringer, A. Schilz, K. Goller, and W. Pretti. Far-infrared bandpass filters from perforated metal screens. *Applied Optics*, 33(1):39–41, 1994.

[94] V. P. Tomaselli, D. C. Edewaard, P. Gillan, and K. D. Moller. Far-infrared bandpass filters from cross-shaped grids. *Applied Optics*, 20(8):1361–1366, 1981.

[95] Ville Kettunen, Markku Kuittinen, Jari Turunen, and Pasi Vahimaa. Spectral filtering with finitely coducting inductive grids. *J. Opt. Soc. Am. A*, 15(10):2783–2785, 1998.

[96] Henri J. Lezec and Tineke Thio. Diffracted evanescent wave model for enhanced and suppressed optical transmission through subwavelength hole arrays. *Optics Express*, 12(16):3629–3651, 2004.

[97] U. Schroter and D. Heitmann. Surface-plasmon-enhanced transmission through metallic gratings. *Physics Review B*, 58(23):15 419 – 15 421, 1998.

[98] Rashid Zia, Mark D. Selker, Peter B. Catrysse, and Mark L. Brongersma. Geometries and materials for subwavelength surface plasmon modes. *J. Opt. Soc. Am. A*, 21(12):2442–2446, 2004.

[99] Andreas Drauschke, Bernd Schnabel, and Frank Wyrowski. Comment on the inverse polarization effect in metal-stripe polarizers. *J. Opt. A: Pure Appl. Opt.*, 3:67–71, 2001.

[100] Hans Lochbihler. Surface polaritons on gold-wire gratings. *Physical Review B*, 50(7):4795–4801, 1994.

[101] J. M. Steele, C. E. Moran, A. Lee, C. M. Aguirre, and N. J. Halas. Metallodielectric gratings with subwavelength slots: Optical properties. *Physical Review B*, 68:205103–1 – 205103–7, 2003.

[102] J. A. Porto, F. J. Garcia-Vidal, and J. B. Pendry. Transmission resonances on metallic gratings with very narrow slits. *Physical Review Letters*, 83(14):2845–2848, 1999.

[103] R. J. Bleiler, R. S. Hockett, P. Chu, and E. Strathman. Sims measurements of ozygen in heavily-doped silicon. *Material Research Society Symposia Proceedings*, 59:73–79, 1986.

[104] G. Perez and J. M. Sanz. Infrared characterisation of evaporated SiO thin films. *Thin Solid Films*, 416:24–30, 2002.